Highly-efficient entanglement transfer into and out of cold-atom quantum memories

Félix Hoffet

SORBONNE UNIVERSITÉ

THÈSE DE DOCTORAT
DE SORBONNE UNIVERSITÉ

Spécialité : Physique

École doctorale nº564: Physique en Île-de-France

réalisée sous la direction de Julien LAURAT

au Laboratoire Kastler-Brossel

présentée par

Félix HOFFET

Sujet de la thèse :

Highly-efficient entanglement transfer into and out of cold-atom quantum memories

soutenue le 28 3 2022

devant le jury composé de :

M.	Afzelius Mikael,	Professeur,	Univ. de Genève,	Rapporteur
M.	Chanelière Thierry,	Chargé de recherche,	Institut Néel,	Rapporteur
Mme	Diamanti Eleni,	Directrice de recherche,	Sorbonne Université,	Examinatrice
M.	Goldner Phillipe,	Directeur de recherche,	Chimie Paristech,	Examinateur
Mme	Goldfarb Fabienne,	Maitresse de conférences,	Univ. Paris-Saclay,	Examinatrice
M.	Laurat Julien,	Professeur,	Sorbonne Université,	Directeur de thèse

Contents

Remerciements

Mes premiers remerciements se dirigent tout d'abord vers mon directeur de thèse Julien Laurat. Depuis mon arrivée en stage de Master, j'ai bénéficié de sa vision pointue du domaine qui m'a permis de comprendre les enjeux globaux de la recherche sur les mémoires quantiques. Sa confiance en ma capacité à gérer cette expérience complexe m'a encouragé à mener à bien un travail expérimental soutenu. Ses précieux conseils ont permis l'obtention de résultats importants.

Durant ma thèse au laboratoire, j'ai aussi eu la chance de rencontrer d'autres personnes qui ont beaucoup influencé ma vision, ma compréhension et mes résultats. Je remercie Mingtao Cao, le premier post doc à m'avoir acceuilli sur l'expérience mémoire, pour m'avoir appris les rudiments du travail expérimental en optique quantique. Thomas Nieddu m'a ensuite rejoint sur l'expérience. Je le remercie pour sa bonne humeur, sa modestie et sa franchise. J'ai largement bénéficié de sa présence tant sur le plan scientifique que humain, et je suis heureux aujourd'hui de le compter parmi mes amis. J'ai aussi eu la chance de démarrer ma thèse le même jour que Jeremy Berroir, thésard sur l'expérience nanofibre. Entre autres, je le remercie pour nos nombreuses discussions sur la physique atomique car j'ai énormément bénéficié de ses connaissances théoriques. Au dela de la physique, notre évolution en parallèle au laboratoire nous a aussi permis de devenir amis. Je remercie aussi Thomas et Jeremy pour nos parties d'échec endiablées qui ont ponctué notre aventure au LKB. Je suis aussi heureux d'avoir rencontré les autres membres de l'équipe "Quantum Networks" qui m'ont aussi influencé tout au long de ce doctorat : Tom Darras, Adrien Bouscal, Hadriel Mamann, Beate Asenbeck, Alban Urvoy et Tridib Ray. L'ambience au sein de l'équipe a constitué un vrai atout au cadre de travail au laboratoire.

Je souhaite aussi remercier Anaïs Labeyrie pour sa présence à mes côtés pendant cette période. Elle a su m'écouter et me conseiller lors de ma traversée de moments parfois difficiles qu'un doctorat en physique expérimentale peut offrir. Je ne sais pas dire à quel point cette thèse aurait été différente sans elle. Je remercie aussi mes meilleurs amis Maxime Schwarz, Emile Chevrin et Martin Czertow (MEMF) pour leur présence et leurs conseils.

Finalement, j'ai une pensée très forte pour mes parents sans qui je ne serais pas arrivé là aujourd'hui. J'ai bénéficié de leur clairvoyance et leur support tout au long de ma thèse. Les moments partagés lors de la soutenance ont été inoubliables. Je remercie aussi les autres membres de ma famille, notamment mon frère et grand maman qui sont des personnes importantes pour moi.

Introduction

Over the recent years, the amount of money that has been invested in quantum technologies (public research or private companies) has increased exponentially. At the European level for instance, a 1-billion euros flagship program has been lauched by the European commission to support quantum research for ten years starting from 2018 [Cartlidge 2018]. This program led in particular to the creation of the Quantum Internet Alliance (QIA) consortium in which our group has been an active member and in which I actively participated throughout my PhD. The goal of this consortium is to eventually create the first quantum network in Europe by combining the strengths of many research labs and companies. With similar efforts and national initiatives over the world, an increase in development speed of quantum technologies is expected to be observed. Thus, the 2020-2030 decade will be a crucial test to assess the pratictability of quantum technologies in quantum communication. In this endeavour, a key technology is the ability to map quantum states of light into and out of quantum memories, with high efficiency. This is the topic of the present work. In this thesis, the 90% efficiency mark was reached, an essential requirement to build large-scale networks.

Context

I joined Prof. Julien Laurat's group as an intern in April 2018 and started my PhD shortly after in October 2018. The experimental setup, relying on a cold atomic ensemble, was already well established since four generations of PhD students had worked on it before me. As the last PhD student had already defended his thesis when I joined the group, I was welcome by Mingtao Cao who was a post-doctoral fellow at the time. We worked together for two years until he got a position in China in X'ian. I was then working alone for a few month before Thomas Nieddu joined me on the experiment as a post-doctoral fellow. Finally, Hadriel Mamman started as a PhD student in October 2020.

When I joined the group, the team had just published their latest result [Vernaz Gris, Huang, et al. 2018] that demonstrated an efficient memory for polarization qubits operating on the D_2 line of cesium. The efficiency in this work more than doubled the state of the art but seemed limited to about 65%. The plan at that time was to modify the experiment to make it compatible with the D_1 line of cesium and build a single-photon source using DLCZ, in order to perform a storage experiment with single photons which would yield large storage-and-retrieval efficiency. Indeed the simulations predicted around 90% should be achievable using the specific D_1 transition and pushing the number of atoms to higher values. We modified thereby the setup for a long period of time with Mingtao until we were ready to take data. It finally enabled to reach a storage-and-retrieval efficiency close to 90%. Ultimately, we focused on a fundamental requirement, namely the efficient transfer of single-

photon entanglement into and out of entangled quantum memories. This experiment yielded results that paved the way toward scalable quantum networks made of efficient memories and was published in Optica [Cao et al. 2020].

During my PhD, I was also affected by the pandemic crisis of COVID-19 since we had to stop our experimental research activity for a few months during the first lockdown. After that period of time, we needed to work part-time in the lab for almost a year, which made it difficult to carry out other experiments and keeping it aligned. Nonetheless, the sanitary crisis was a good opportunity to focus on the bibliographic aspect to find ideas on how to improve our setup. Eventually, we decided to improve the experiment by changing some of its essential components. Now, a quantum cryptography experiment, namely a quantum money protocol involving a quantum memory is ongoing. In parallel, we are pushing the multimodal capability thanks to the multiplexing of Hermite-Gaussian spatial modes of light.

Alongside research activities, I also had the chance to teach at Sorbonne University. During the first two years, I taught electromagnetism to a class of second year students. Moreover, I also had the opportunity during my second year to follow a group of third year students as they built a physics project from the ground up. The teaching as a supplementary activity was a nice addition to my PhD work.

Outline

The following thesis is organized in four chapters.

Chapter 1 introduces the general quantum information concepts that are central to this thesis, and gives an overview of the state of the art of research on quantum networks. We focus in particular on quantum memories, defining important parameters and presenting different schemes. We review the recent advances in quantum memories with cold atoms, and emphasize on the efficiency, storage time and multimodality of memories. We end the chapter by exploring a toy model in order to illustrate the scaling of repeater protocols with memory parameters. Specifically, we note that the efficiency of quantum memories is a crucial parameter that need to be maximized to build large scale quantum networks.

Chapter 2 describes the atom-light interactions that are relevant to this thesis. Specifically, we study the electromagnetically induced transparency phenomenon and explain how it is used to perform memory experiments with cold atoms by the means of slow light, dark-state polaritons and collective spin excitations. Eventually, we discuss the critical conditions that are required for efficient quantum storage. Among others, we explain how the D_1 line is more suitable for high efficiencies as compared with the D_2 line. These conditions have guided the work of this thesis to renew the setup in order to perform experiments with highly efficient memories.

Chapter 3 presents the experimental tools and techniques that we developped. We start by explaining how we implement our magneto-optical trap and describe the techniques to characterize its properties such as optical depth, temperature and magnetic environment. We then focus on the optimization of these properties and detail how we can reach high values of optical depth in our experiment. Specifically, we explain the difference between two approaches, a temporal dark-MOT and a compressed PG-cooled

MOT. Finally, we present our experimental apparatus from our laser system to our atomic trap setup.

Chapter 4 reports on a highly-efficient single-photon storage and the reversible mapping of photonic entanglement. We first explain the implementation of a single photon source based on the DLCZ scheme and report the generation of single photons with low two-photon contribution and tunable temporal shape. We then demonstrate the single-mode storage of a single photon with a storage-and-retrieval efficiency of $\eta = (87 \pm 5)\%$. Finally we detail the experimental process of entanglement mapping and show that we have obtained an entanglement transfer parameter of $\lambda = (80 \pm 20)\%$ without any correction.

Chapter 1

Optical quantum memories for scalable quantum networks

This general introduction aims to decribe the field of quantum communication and the needs of quantum memories in the envisionned quantum internet. It is separated in four distinct sections. The first one introduces the concept of quantum information processing and describes the motivations of this broad research field. The second section focuses on quantum communications and outlines the structure of a quantum internet from its quantum information carriers to the components of its quantum nodes. Then, we examine in more detail the research field on quantum memories by reviewing today's state of the art. We conclude this chapter with the presentation of quantum repeater simulations, considering a chain of elementary segments. The goal of these simple simulations is to give an idea of the scaling of several memory parameters as a function of the performance of a quantum repeater chain.

1 Quantum information

1.1 What is information ?

Information is a general concept that represents data and its encoding. Etymologically, the word *information* comes from the latin *informare* that means "to form an idea of" or "give form to". This concept is strongly related to physics since it represents something that is carried by a physical system and that can be modified through physical processes. Shannon describes information as a generalization of the concept of entropy [Shannon 1948] used in statistical physics. For a random variable X with $\{x_1,...,x_n\}$ possible outcomes that occur with probability $\{P(x_1),...,P(x_n)\}$, the Shannon entropy is defined by

$$-\sum_i P(x_i)\log_2\left[P(x_i)\right]. \tag{1.1}$$

Here, the base 2 logarithmic function is used to give the result in units of *bits*. A simple example is to consider a coin toss with known probabilities for the two outcomes. If the probability for getting tails is 1/2, the uncertainty on the result is maximal and the information carried by the coin is 1 bit. On the other hand, if the coin is flawed and has a probability of 1 for tails, the entropy is zero since each toss cannot deliver new information.

1.2 Limits of classical information

Classical information is nowadays encoded as series of *bits* (binary digits). In general, the physical system that encodes these bits is the transistor, building block of modern computers. Computation (or processing) is made through the manipulation of these bits with *gates*, that are basic arithmetic logical operations.

Throughout the last few decades, the growth of available computational power and the new applications of computers dramatically transformed our society. Over those years, the emergence of new technologies improved the capacity of processors according to Moore's law [Moore 2006], predicting (empirically) that the number of transistor per computer microprocessor doubles every two year. Making the hypothesis that a processor stays the same size with time, we see that Moore's law has a fundamental limit when the length between each transistor reaches a sub-nanometer scale where quantum effects start to be dominant. To overcome this limit, we will need the ability to create processors dealing with such quantum features.

1.3 Quantum information resources and properties

Quantum theory offers resources that are non-existent in classical information. For example, the existence of truly random events through a measurement operation, impossible in deterministic classical dynamics, is core to quantum mechanics. Furthermore, the nature of a quantum state and its measurement is an essential difference between quantum and classical information.

Qubits In quantum mechanics, the superposition principle allows the state of a system to be described as a coherent superposition of two configurations. In contrast to the classical bit, we define the quantum bit (qubit) to be a superposition of two orthogonal quantum states $|0\rangle$ and $|1\rangle$. The general qubit state can be written as

$$|\psi\rangle = \alpha\,|0\rangle + \beta e^{i\varphi}\,|1\rangle\,. \tag{1.2}$$

Information is encoded in the real amplitudes α and β, and in the relative phase φ. The states $|0\rangle$ and $|1\rangle$ can be generated from any two orthogonal eigenstates of an observable. For example, a qubit can be encoded in the presence or absence of a photon, the polarization of a photon, the state of an atom or the current in a superconducting loop.

It is generally convenient to represent the qubit state on the surface of a sphere called the *Bloch sphere*. With spherical coordinates, we write $\alpha = \cos(\phi/2)$ and $\beta = \sin(\phi/2)$ where ϕ is the angle between the state and the z-axis that crosses the two poles. The poles of this sphere represent the orthogonal $|0\rangle$ and $|1\rangle$ states. Any rotation along the z-axis represents a variation of phase between the two states.

Entanglement Entanglement is an essential and intrinsic quantum feature that occurs when several physical systems share correlations that make impossible to describe the state of one system independently of the state of the others. Entanglement can lead to correlations between distant objects, implying that quantum theory is a *non-local* theory. This idea emerged from the work of John Bell [Bell 1964] who showed that the predictions of quantum mechanics cannot be reproduced by any local hidden variable theory. After the seminal

experiment of Alain Aspect and colleagues in 1982 [Aspect et al. 1982], quantum non-locality has been demonstrated on various experiments and in several physical systems [Rowe et al. 2001; Hensen et al. 2015; Giustina et al. 2015; Shalm et al. 2015].

Mathematically, entanglement is defined in opposition to a certain class of states called *separable* states. A separable state designates a state of a system than can be written as a tensor product of the state of its system constituents. An entangled state cannot be written as a product state and the system cannot be considered by independently considering its subsystems. For a system made of two particles A and B, a separable state of the global system writes $|\Psi\rangle_{AB} = |\psi\rangle_A \otimes |\psi\rangle_B$. An entangled state can be a sum of separable state, for example :

$$|\Psi\rangle_{AB} = \frac{1}{\sqrt{2}} \left[|0\rangle_A \otimes |1\rangle_B + |1\rangle_A \otimes |0\rangle_B \right]. \tag{1.3}$$

Again, this state can be encoded in numerous bases such as presence or absence of a photon, polarization and so on. The state $|\Psi\rangle_{AB}$ is known as a Bell-state and, together with three other Bell-states, form a basis for any two-mode entangled state. More generally, entanglement is not limited to two parties, but can be extended to an unlimited number of parties that all share non-local correlations. For example, this can be made experimentally with cluster states or with frequency combs [Chen et al. 2014; Larsen et al. 2019].

No-cloning theorem In quantum theory, performing a measurement of one observable A will influence the outcome of an ulterior measurement on observable B if $[A,B] \neq 0$. It is therefore inevitable to disturb the state of a system by acquiring information on it. This property is linked to one of the most essential feature of quantum information, the so called no-cloning theorem [Wootters and Zurek 1982], that states impossible to create identical copies of an arbitrary unknown quantum state. This principle has important consequences in quantum information science and is one of the building blocks of quantum cryptography.

1.4 Towards quantum computing

Quantum information science therefore has access to a whole new set of resources emerging from quantum mechanics. Let us now examine the motivations of research in quantum information science and see what applications it can bring that are not feasible with classical technologies.

Quantum computing A first goal in quantum information science is to reach the ability to build *quantum computers* that can manipulate qubits in order to perform the same tasks than a classical computer, but exponentially faster. This goal emerged in 1994 with the seminal discovery that some quantum algorithms may outperform their classical couterparts in terms of computation time [Shor 1994; Chi-Chih Yao 1993]. A typical example is Shor's quantum algorithm [Shor 1994; Shor 1997], that allow to factor an integer N into its primes factors in a time that only grows polynomially in $\log N$. Classically, the most efficient factoring algorithm has an exponential complexity that makes the time to solve the problem in powers of $\log N$. This makes the quantum algorithm almost exponentially faster than its classical counterpart. The problem of factoring numbers into their prime factors is actually well known for its complexity since most of classical cryptography is based on this algorithm. Since Shor's algorithm is based on the efficiency of the quantum Fourier transform algorithm, there exist

many others quantum algorithms that can have an improved time of success as compared to their classical counterpart. Some famous example are the Deutsh-Jozsa algorithm [Deutsch and Jozsa 1992], Simon's algorithm [Simon 1997] or Grover's algorithm [Grover 1996]. Note that an algorithm performed by a quantum computer is a probabilistic algorithm due to the randomness of the quantum measurement process. Shor's algorithm is not guaranteed to succeded in finding the prime factors, it does it with a high probability. Eventually, this is not a problem since it is easy to verify the solution.

A quantum computer consists in a collection of qubits that can be adressed by specific quantum gates in order to create several circuits. To be scalable, a real quantum computer should be able to perform any type of quantum computation on the same platform hardware and have the ability to perform error-correction on a very large number of qubits. Experimentally, we are still far from this perspective. Nevertheless, numerous efforts are done in the field to demonstrate algorithm realizations. For example, Shor's algorithm has been achieved on various platforms [Vandersypen et al. 2001; Lu et al. 2007; Lanyon et al. 2007; Lucero et al. 2012] although without showing any improvement over the classical time taken by the algorithm to solve the problem. Nowadays, the quantum advantage, i.e. demonstrating that a programmable quantum device can solve a problem that no classical computer can solve in any feasible amount of time, is pursued by academic labs but also large private companies such as Google, IBM or Intel. The first claim of quantum advantage has been made by Google in 2019 [Arute et al. 2019] performing a series of operations in 200 seconds on a superconducting array made of 54 qubits, which would supposedly take more than ten thousands years to complete on a classical supercomputer. In december 2020, Jian Wei Pan's group in USTC demonstrated quantum advantage for Boson sampling on a 76 qubit photonic platform [Arrazola et al. 2021]. The paper states that the number of samples generated over 20 seconds is equivalent to that generated by a classical supercomputer in 600 million years. These recent demonstrations illustrate the difficulty of such a goal but potentially pave the way toward a new era.

Quantum simulation Another motivation for the interest in quantum information science arises from the inherent difficulty to simulate large quantum systems on classical computers. This difficulty emerges from the size of the Hilbert space of a system containing a large number N of particles. With classical interactions, such a problem can be resolved with at least N bits whereas for a quantum system at least 2^N bits is required to fully simulate the state of the system. An ideal quantum simulator is a device that has the ability to simulate the evolution and behaviour of any quantum system. Even if this goal is not reachable yet, there already exists many physical platforms that enable the quantum simulation of specific Hamiltonians, with the ability to tune some parameters of the simulated model [Schymik et al. 2020; Bloch et al. 2012; Blatt and Roos 2012; Aspuru-Guzik and Walther 2012; Nguyen et al. 2018; Scholl et al. 2021].

2 Quantum communication

Parallell to the research field of quantum computing is the field of quantum communications [Gisin and Thew 2007]. Quantum communication science can be defined as the generation and transmission of quantum states between remote places.

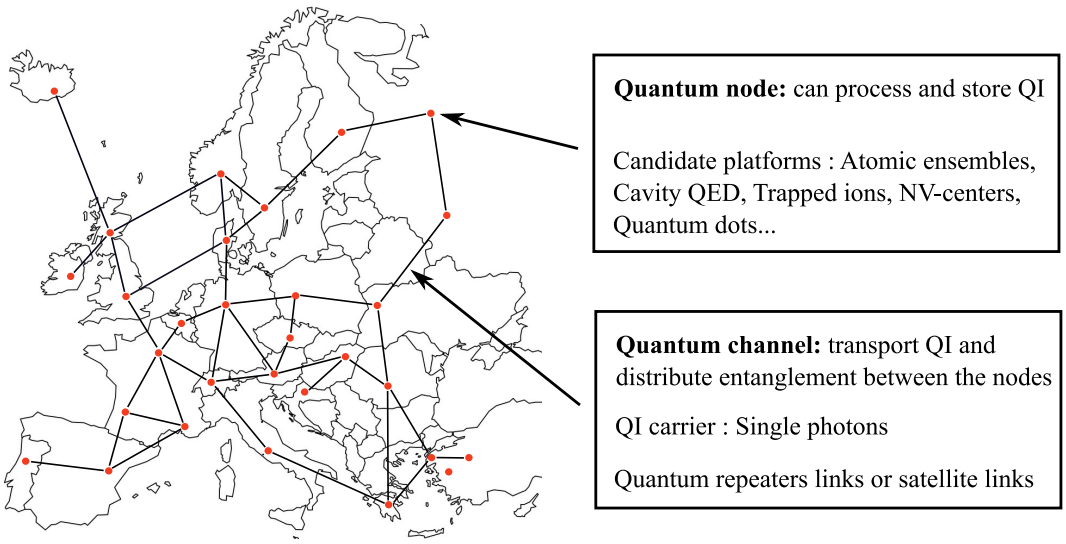

Fig. 1.1 *Schematic view of a European quantum internet. Quantum nodes (represented by red dots) are linked via quantum channels (black lines). Quantum information can be sent at each node of the network and entanglement can be distributed along them. Information is processed by the nodes and can ideally be stored as well.*

2.1 Quantum internet and quantum networks

An exciting prospect of the development of quantum communication science is the perspective of building a global *quantum internet* [Kimble 2008; Wehner et al. 2018]. The envisionned quantum internet is based on *quantum repeaters* [Cirac et al. 1997; Briegel et al. 2000] enabling quantum communication between any points of the network. These *quantum nodes* are spread over long distances among the whole world where quantum information is generated, processed and stored in each of them. All nodes are connected by *quantum channels* that distribute entanglement across the whole network and transmit quantum states with high fidelity. Quantum networks are closely linked to quantum information processing since they could connect quantum processors in order to achieve capabilities that are provably impossible using classical means. In the following paragraphs, we discuss the structure of a quantum internet and describe the state of the art on this topic.

Single photons Single photons are ideal carriers for quantum information. They travel at the speed of light and possess numerous degrees of freedom on which one can encode information. Logically, one main research activity focuses on the generation of single photons and other non-classical states. The characteristics required by single-photon sources depend on the considered network architecture but ideally the source should be *on-demand* (i.e. press a button to get a photon in a deterministic way) and the fidelity of the output state to the Fock-state $|1\rangle$ should be 100% [Eisaman et al. 2011]. The repetition rate should be

high and the emited photons should be completely indistinguishable. Lately, the ability to multiplex the generation of single photon in several degrees of freedom has also become an important goal to achieve scalable quantum networks [Meyer-Scott et al. 2020].

One important parameter is the purity of a single photon that can be assessed by the normalized Glauber second-order correlation function $g^2(0)$. It is similar to measuring the fidelity of the photon to $|1\rangle$ in the sub-space excluding vacuum since it measures multiphoton-components. This parameter, besides being easy to measure, is crucial since the multiphoton components of the state are generally the limiting factors in Bell-type measurement and swapping operations [Laurat et al. 2006]. The indistinguishibility is quantified using the visibility of Hong-Ou-Mandel interference [Hong et al. 1987; Osorio et al. 2013].

The most widely used sources are based on nonlinear frequency conversion [Burnham and Weinberg 1970]. They are usually operated at room-temperature using parametric down-conversion in non-linear crystals. They are *probabilistic* sources in the sense that correlated photon pairs are emitted at random times. A main characteristic is that the two photons can be made non-degenerate in order to be separated deterministically after generation. A subsequent detection of one photon *heralds* the presence of the twin photon in the other mode with high probability. The produced photons are pure, highly indistinguishable and can also be used as polarization entangled photon pairs. Such sources are being investigated at LKB where single photons at 91% fidelity and $g^2(0) = 10^{-3}$ can be produced at a rate of 200 kHz [Morin et al. 2012; Jeannic et al. 2018]. The drawback of such sources comes from their probabilistic nature, which sometimes makes them unsuitable for several applications [Eisaman et al. 2011]. Quantum dots [Gazzano et al. 2013; Senellart et al. 2017] and color-centers in crystals [Mizuochi et al. 2012] are the two main platforms of *deterministic* single-photon sources. These quantum emitters offer remarkable emission properties but suffer from low indistinguishability due to charge fluctations in their local environment [Kuhlmann et al. 2013]. The emission rates reach the GHz level altough the escape efficiency is limited to around 30% due to filtering. The purity is high and the antibunching parameter can reach $g^2(0) = 10^{-4}$ [Schweickert et al. 2018], limited by the dark counts of the single-photons detector. Their emission is broadband and each emitter has a slightly different output spectrum, which can potentially make them impractical for several interfacing applications.

The research field in single photon sources is constantly evolving and a lot of advances have been achieved over the recent years. A full review on this topic is out of the scope of this thesis, however these developments are tremendously important for future quantum networks since single photons are meant to be the information carriers. Single photons will therefore be used in quantum channels to transmit quantum information and generate entanglement between nodes of the network. These channels can be built in free-space using satellites [Yin et al. 2020] or in fiber-based links [Boaron et al. 2018]. However, single photons are sensitive to losses induced by propagation in optical fibers. One way to overcome this requires the use of a *quantum repeater* [Briegel et al. 1998] as this will be discussed in the next section.

Quantum nodes Having photons as information carriers means that the quantum nodes must be interfaced with these photons in order to process the transported quantum information. One main scientific challenge is therefore to achieve coherent control over the interactions between single photons and matter. Several physical platforms are investigated in this direction, all with their specific advantages and drawbacks. Atomic ensembles [Chou et al. 2007; Duan et al. 2001; Hammerer et al. 2010] are excellent candidates since simply

increasing the numbers of atoms can improve the interaction strength between the single photon and the ensemble. Cavity quantum-electrodynamics made of a single atom trapped in a cavity is also a promising system for light-matter interfacing [Parkins et al. 1993; Enk et al. 1998; Brekenfeld et al. 2020; Raimond et al. 2001; Reiserer and Rempe 2015] since the cavity enables strong coupling between the field and the single atom. Systems made of trapped ions in cavities are also being investigated because using ions can enable the deterministic preparation of a quantum state [Leibfried et al. 2003; Stute et al. 2013; Northup and Blatt 2014; Stute et al. 2012] while the cavity enables highly efficient mapping of the ion's state to a single photon. Spin systems in solid-state crystals, specifically nitrogen-vacancy centers in diamond are also a platform of interest offering a strong robustness to decoherence and long coherence time [Kane 1998; Hanson and Awschalom 2008; Dutt et al. 2007; Pompili et al. 2021; Bernien et al. 2013; Humphreys et al. 2018]. Recently, light-matter interfacing has also been studied in the context of atoms trapped in the vicinity of nanostructures such as nanofibers [Corzo et al. 2016; Corzo et al. 2019; Prasad et al. 2020] and photonic crystal waveguides [Berroir et al. 2021; Goban et al. 2014; Goban et al. 2015; Đorđević et al. 2021].

Interfacing Another major challenge for the realization of scalable quantum networks is the connection of heterogeneous platforms. For instance, the physical platform of an *end node* of the network will be different from the platform used in a central node, where a quantum memory will be present. In this prospect, the ability to tune the frequency of single photons travelling around in the network is an essential requirement. This can be achieved with *quantum frequency conversion* (QFC) [Kumar 1990]. QFC can be done thanks to sum- or difference-frequency conversion in non-linear χ^2 crystals or in atomic vapors by means of four-wave mixing. In general, QFC aims to convert photons from the platform's frequency to the telecom band where the losses of fiber propagation are the lowest. In this endeavour, QFC experiments have been realized with atomic quantum memories [Chanelière et al. 2006; Radnaev et al. 2010; Maring et al. 2017] with conversion from visible to telecom wavelength, with quantum dot photons using crystals [De Greve et al. 2012] or using non-linear waveguides [Maring et al. 2018]. The requirement of QFC for making quantum networks scalable brings one more layer of difficulty to its realization since frequency conversion has limited efficiency (30 to 60% at best depending on the frequencies) and can be noisy.

On the other hand, it is possible that future quantum networks will allow the distribution of quantum information via different types of encoding. For example, both discrete-variable encoding and continuous-variable encoding offer advantages for specific tasks [Kok et al. 2007; Braunstein and Loock 2005]. Our team at LKB is working on these aspects by engineering non-gaussian states combining these two encodings. For instance, it is possible to generate hybrid entangled-states [Morin et al. 2014] and perform hybrid entanglement swapping between these two encodings [Guccione et al. 2021].

Operation While most of the research focuses on the hardware of a quantum internet, some investigate the architecture possibilities of a fully fledged quantum network and its high level programming possibilities [Wehner et al. 2018]. An ideal and fully functionning quantum network may be structured as a stack made of layers [Dahlberg et al. 2019], similar to what is done in the classical internet today. Each layer has its own function, allowing for abstraction of technical details from the layer above it. The lowest level layer is the physical layer which consists in the quantum devices and their arrangement in space. Since architectures made of

several interconnected nodes, repeaters and channels are highly complex for mathematical analysis, machine learning optimization can be used to find the optimal construction of quantum networks [Coopmans et al. 2021].

2.2 Quantum repeater: the importance of quantum memories

While the concept of a quantum network may be simple, it is not a simple task to build one. A major challenge to overcome is to generate entanglement at large distances despite losses induced by fiber propagation. A solution to this problem is to use quantum repeaters that rely on quantum memories. In this section, we motivate the research towards fully fledged quantum repeater and explain why the inclusion of quantum memories, which are at the heart of this thesis, is a necessary task.

Fiber losses When light propagates into a fiber, it is subject to an exponential attenuation mainly caused by Rayleigh scattering and absorption. The light transmission $T = e^{-L/L_0}$ is attenuated differently depending on the light frequency, and the attenuation length L_0 reaches a maximum for $\lambda = 1550$ nm. At this wavelength, the losses reach 0.2 dB/km. For instance, if one consider a source generating telecom single photons at a rate of 1 GHz, the time it takes to transmit just one photon over 1000 km is as high as 300 years. This limitation is overcome in classical communications by using *repeaters* that amplify light signals. However, this capability is not available in quantum communications since amplification of quantum states is forbidden by to the no-cloning theorem.

Concept *Quantum repeaters* have been proposed in 1998 [Briegel et al. 1998] as a solution to overcome this limitation. The concept relies on the transfer of qubits using quantum teleportation [Bennett et al. 1993; Bouwmeester et al. 1997; Furusawa et al. 1998; Marcikic et al. 2003] where entanglement is distributed along the nodes thanks to *entanglement swapping* [Pan et al. 1998]. The protocol to establish entanglement between two nodes separated by a distance L is first to divide this channel into N shorter segments of length L/N. Entanglement is then generated in each segment and entanglement swapping is performed between all adjacent nodes in order to distribute the entanglement along the whole link.

Synchronization Losses are encountered at every stage of the repeater and, most importantly, entanglement generation is probabilistic. These two limitations lead to the mandatory inclusion of a quantum memory that enables to store entanglement as illustrated on Fig. 1.2. Let us illustrate this need by a simple example: even if the generation of entangled single photons is deterministic, the propagation losses in a small segment of length L/N makes the entanglement generation probabilistic with a probability of $e^{-L/(NL_0)}$. The swapping must be performed when all segments are equipped with an entangled pair, which happens with a probability of $\left(e^{-L/(NL_0)}\right)^N = e^{-L/L_0}$. We see that this probability is equal to the original exponential decay and therefore there is no improvement upon the simple propagation over a fiber link. However, if one segment can store the generated entanglement while its neighbour is trying to generate entanglement, the probability of getting all the segments entangled can be increased to 1 (if the quantum memory has an infinite lifetime). The memory therefore acts as a synchronization tool that allows the entanglement to be stored in order to be retrieved on demand, when the system is ready to perform entanglement swapping.

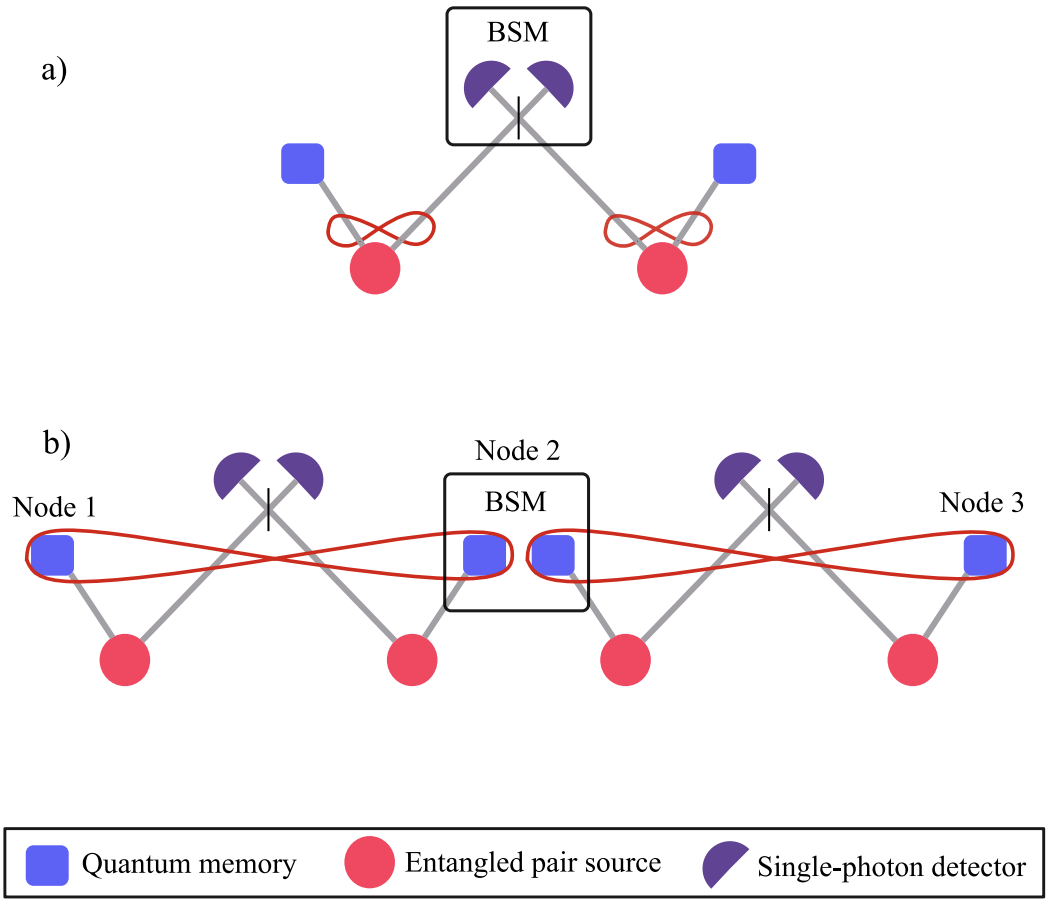

Fig. 1.2 *Scheme of a quantum repeater. a) Elementary segment of a quantum repeater. Single-photon entangled pairs are produced by sources indicated by the red circles. One mode of each entangled pair is sent to a Bell-state measurement station, and the other mode is stored into a quantum memory. A single detection on one of the detectors induces entanglement between the two memories. b) A quantum repeater made of two segments: Node 1/Node2 and Node 2/Node 3. Once entanglement has been generated in each elementary segment, entanglement swapping is performed by doing a Bell-state measurement on the two memories of Node 2. For example this measurement can be done by reading the memories, make the retrieved photons interfere on a BS and measuring each output. The detection of one photon heralds the entanglement of Node 1 and Node 3.*

Entanglement purification In practice, the generated entanglement has a Bell-state fidelity below one such that performing swapping gates to enable the connection of nodes induce some noise that alter the resulting fidelity of the state. A protocol has been proposed to increase the quality of the entanglement, called *entanglement purification* [Bennett et al. 1996]. The idea is to increase the purity of an entangled state by performing measurements on a set of other entangled states, that are lost in the process. It has been experimentally demonstrated on various platforms [Pan et al. 2001; Franzen et al. 2006; Kalb et al. 2017] although its inclusion in a quantum repeater scheme is believed to be difficult in practice. One way to include it in repeaters architecture could be by *multiplexing* the entanglement generation. If multiple entangled pairs are produced on a same segment, one could perform entanglement purification of one mode using all other entangled modes.

Experimental realizations In general, quantum memories have finite lifetimes and efficiencies below unity. Adding this to the fact that entanglement generation is probabilistic and is created with a Bell-state fidelity below 1 makes the realization of a scalable quantum repeater a tremendous challenge. Recently, experimental elementary instances of quantum repeaters have been realized [Pu et al. 2021; Li et al. 2019; Pompili et al. 2021; Lago-Rivera et al. 2021; Chou et al. 2007] although none of them includes all the necessary ingredients of a fully functionnal quantum repeater. The implications of quantum memories properties for the success of building quantum repeaters is studied in section 4 of this Chapter.

2.3 Applications

The purpose of a quantum internet is to enable applications that are out of reach for the classical internet. Akin to the early days of the classical internet, it is hard to predict all uses of a future quantum internet [Kimble 2008; Wehner et al. 2018]. However, several major applications have already been identified and some of them can even be implemented before a fully fledged quantum network is achieved [Wehner et al. 2018].

Qubit teleportation The first application that comes to mind is the transfer of quantum information from one node of the network to another, via *quantum teleportation* [Bennett et al. 1993]. It could also be seen as a capability rather than an application since teleportation is at the hearth of many application protocols. Qubit teleportation can be performed when two nodes are entangled. The external state to be teleported can be unknown, and is measured jointly with one mode of the entangled link. This Bell-state measurement gives a result which is transferred through a classical channel to the other end of the entangled link. By applying a unitary transformation conditioned upon the result of the initial Bell-state measurement, the initial state can be recovered in the end node. This protocol destroys the initial entanglement shared by the two nodes of the link. The first experimental realization was made in 1997 by Zeilinger's group [Bouwmeester et al. 1997] and quantum teleportation is now widely used in several academic labs. Our group at LKB is currently working on the teleportation of qubits from continuous variable encoding to discrete variable encoding.

Quantum money Thanks to the no-cloning theorem, other cryptography schemes than QKD exist. Quantum money is one of them and aims to protect against forgery of cheques, banknotes or credit cards by associating them with a secret key encoded into quantum states.

The idea is that a bank can verify the authenticity of a quantum credit card thanks to a distant payment terminal that performs local quantum operations only and communicates classically. This has the advantage to avoid long-distance propagation of quantum states which can lead to the rejection of honest credit cards due to noise and losses. The first proposal dates from 2014 [Gavinsky 2014] and has been improved since to a scheme in which the terminal can be untrusted and coherent states of light can be used instead of single photons [Bozzio et al. 2018; Bozzio et al. 2019]. In these type of schemes, a highly efficient quantum memory can be useful, acting as the quantum credit card. An implementation is currently ongoing in the group.

Metrology and sensing A quantum internet also has applications in the field of metrology and sensing. For instance, the use of atomic clocks in quantum nodes could increase the accuracy and precision of GPS systems [Kómár et al. 2014]. Quantum networks could also increase the precision of telescopes [Gottesman et al. 2012]. Another major application enabled by quantum networks is the field of *distributed quantum computing*. The interconnection of quantum processors enables an exponential speed-up of computing power with a linear amount of physical resources [Van Meter and Devitt 2016]. This distributed computing also allows protocols such as *blind quantum computing* [Broadbent et al. 2009], which allows a server to perform quantum computation for a client in such a way that the client's inputs, outputs and computation remain private and secure. In this scheme, the client does not need to have a quantum processor since the computation is made in the "cloud".

3 Quantum memories

As we have seen previously, quantum memories are an essential tool for storage and synchronization of quantum information. In this section, we describe quantum memories and their important figures of merit, and give a brief review of the different memory schemes and platforms.

3.1 Definition and distinctions

A quantum memory is a device able to store quantum information and retrieve it at a later time. We have seen previously that the ideal information carrier for envisionned quantum networks is a flying single photon. Therefore, a quantum memory should be able to store photonic quantum states. The latter includes photonic qubits, single-photon states, entangled states, coherent sates and states encoded in continuous variable such as quadrature squeezed states.

Quantum memories can be implemented in several different platforms. We first make the distinction between three types of protocols: *on-demand* memories, *pre-programmed delay* protocols, and *hybrid* schemes. On-demand quantum memories are generally implemented in an optically-controlled medium with the use of an auxiliary *control* beam. This family of memories includes both *absorptive* and *emissive* protocols. Other types of memories are based on the *engineered absorption* of inhomogeneously broadened systems to implement quantum memories with an initially programmed delay. These include controlled-reversible-inhomogeneous-broadening (CRIB), gradient-echo-memory (GEM) and atomic frequency comb (AFC) protocols, described later in this section. Finally, some schemes combine the

two previous approach of inhomogeneous absorption to the excited state, with an optical π-pulse that is used to map the excited state population onto a long-lived state.

The most recent reviews to date about quantum memories were written five years ago [Heshami et al. 2016; Ma et al. 2017]. Since then, the field has progressed especially on efficiency and lifetime of specific platforms and new memory schemes have been developed. We give a review of this topic later in this section.

We also point out here that quantum memories might also have other uses than synchronization devices for repeaters applications, essentially in metrology or magnetometry [Bussières et al. 2013]. For instance, it was shown recently that a quantum memory could add a computational advantage over the quantum Shor's algorithm if quantum computer would be interfaced with a memory [Gouzien and Sangouard 2021].

3.2 Properties of quantum memories

To characterize quantum memories precisely, several benchmark parameters exist that help to fully assess their capabilities. In the following, we list some of the most important parameters of a quantum memory.

Efficiency (η_m)

The efficiency of a memory is defined by the energy ratio between the retrieved state and the input state. For storage of a single photon, this is simply the success probability of the process. If the efficiency is below unity, it means that the process is lossy. It is sometimes useful to break down the storage-and-retrieval process into two steps, defining the overall efficiency as a product of the two steps' respective efficiencies.

$$\eta_m = \eta_s \eta_r = \frac{E_{out}}{E_{in}}. \tag{1.4}$$

A first fundamental threshold for memory efficiency is to beat the 50% limit which means that more information is retrieved than lost to the environment, a requirement to operate in the no-cloning regime. This threshlod was demonstrated in the group for polarization qubits [Vernaz Gris, Huang, et al. 2018].

Fidelity ($\mathcal{F}$)

The fidelity of a memory measures the similarity between the input and the retrieved state. If each of these states is characterized by a density matrix ρ_{in} and ρ_{out} the fidelity of the memory is defined by:

$$\mathcal{F}(\rho_{in},\rho_{out}) = \mathrm{Tr}\left(\sqrt{\rho_{in}}\rho_{out}\sqrt{\rho_{in}}\right). \tag{1.5}$$

In the case of pure states $|\psi_{in}\rangle$ and $|\psi_{out}\rangle$, the fidelity is given by the squared modulus of their overlap $\mathcal{F} = |\langle\psi_{in}|\psi_{out}\rangle|^2$. Fidelity also have a fundamental threshold which is known as the classical limit, the maximum fidelity that a classical memory can achieve. This bound is equal to $(N+1)/(N+2)$ for a state with N photons [Massar and Popescu 1995], which is $2/3$ for a single photon. This bound is usually taken as a reference to prove that a memory is quantum. If the fidelity threshold is not overcome, we cannot speak of *quantum* memory and the corresponding used term is *optical* memory. In quantum memory experiments, the

fidelity between the input and output state is strongly related to the signal to noise ratio and sometimes, a memory can be very inefficient but still retrieve the state with high fidelity.

Memory lifetime (τ_m)

The lifetime of a memory characterizes the typical storage duration. Several definition exists but it is generally the time at which the retrieval efficiency is decreased by $1/e$ of its initial value.

$$\eta_m(t = \tau_m) = \frac{1}{e}\,\eta_m(t = 0) \tag{1.6}$$

This decay is usually gaussian or exponential. One fundamental threshold to overcome when considering repeater protocols is to have the ability to hold the information for longer than the time it takes to generate entanglement in a segment. This criterion defines the quantum-link efficiency (noted η_{link}) which is the ratio between the lifetime and the entanglement rate in a repeater segment, which should be above unity. The quantum link efficiency is a parameter that involves both the quantum memory and the single-photon sources of a quantum repeater. Another bound needed for large-scale quantum network is that the lifetime should be of the order of the propagation time of flight between two distant points. For a continent-scale network, this time is around 100 ms.

Multimode capacity ($\mathcal{K}$)

Quantum communication protocols can be realized faster if operations can be performed in parallel. To this end, multimode memories that have the capacity to store multiples modes carrying information have been developped. The multimode capacity (noted $\mathcal{K}$ in this thesis) is defined by the number of modes that can be stored simultaneously in a memory. Ideally, the modes should have the possibility to be stored and independently. This means that the writing and reading process should be decoupled in each memory mode and that there exist no contamination from one mode to another, exactly as if the memories were spatially separated. To store a single qubit, two modes are already required. These modes can be encoded in various degree-of-freedom such as temporal, spatial or spectral.

Signal-to-noise ratio (SNR)

Quantum storage usually involves bright laser beams while the signal that needs to be stored is generally at the single-photon level. The ability to measure above the background noise is given by the signal-to-noise ratio, defined by the ratio between the energy of the signal to the energy of the noise, at the detector. This quantity depends on the input signal and is closely linked to the fidelity. In entanglement storage experiments, the SNR is directly related to the degradation of the entanglement coherence through the process. Filtering is usually employed to increase the SNR.

Delay-bandwidth product

The delay-bandwidth product is a useful metric to compare memories that operates at different time scales. It is defined by the ratio of memory lifetime and input pulse duration and it indicates the number of signal pulses that would fit in the typical memory lifetime. This is generally important in repeater applications where memories are used as synchronization

devices. For a probabilistic operation of success probability p, the memories will be impactful if their delay-bandwidth product is greater than $1/p$. This condition is similar to the one that states that the quantum link efficiency η_{link} should be greater than unity.

3.3 Overview of memory schemes

As said earlier in this section, we distinguish different memory schemes by the way they are controlled and identify two main categories. The first group is based on classical auxiliary fields that allow for a dynamic control of the storage and leads to an *on-demand* retrieval. The second group is usually based on engineered absorption in a frequency broadened medium allowing for a storage with a pre-programmed delay.

Dynamical EIT

Dynamical EIT is the scheme used in the work presented in this thesis. The protocol is described in detail in the second Chapter of this manuscript. It relies on electromagnetically-induced transparency (EIT), a quantum phenomenon that modifies the absorption and dispersion of a medium with a strength that is mediated by a control beam [Harris 1997]. EIT is usually accompanied by a strong reduction of the group velocity of light propagation in the medium which allows storage by bringing this velocity to zero. This scheme can be performed with cold-atoms [Vernaz Gris, Huang, et al. 2018; Cao et al. 2020], hot vapours [Julsgaard et al. 2004; Appel et al. 2008; Li et al. 2021], Bose-Eistein condensates [Riedl et al. 2012; Lettner et al. 2011] and solid-state materials such as rare-earth doped crystals [Schraft et al. 2016].

Raman memory

A Raman memory is similar to the dynamic EIT scheme in the sense that it uses a signal pulse and a control beam to map the photon onto an atomic spin state. However in this scheme both signal and control fields are far detuned from the excited state, therefore there is no reduction of light group velocity compared to the resonant case. This gives the possibility to store broad bandwidth pulses and these memories usually have the highest delay-bandwitdh product. This scheme is usually performed in hot vapours [Sprague et al. 2014; Michelberger et al. 2015; Thomas et al. 2017; Saunders et al. 2016; Guo et al. 2019] but can be extended to cold-atoms [Ding, Zhang, Zhou, Shi, Xiang, et al. 2015; Ding, Zhang, Zhou, Shi, Shi, et al. 2015], solid-state [England et al. 2013] or molecules [Bustard et al. 2013].

Atomic frequency comb

The atomic frequency comb (AFC) scheme relies on the engineered absorption of a frequency broadened medium. It is usually performed in solid-state systems that have a natural broadening due to the fluctuation of the electric field inside the material. The large inhomogeneously-broadened absorption line is then shaped as a periodic comb by a spectral hole burning technique. If each comb tooth is separated by the same frequency Δ, the absorption of a light pulse on this transition leads to a re-emission of this pulse after a pre-programmed delay of $2\pi/\Delta$ thanks to photon-echo rephasing [Carlson et al. 1984]. Even though the spectral density of atoms is concentrated on narrow peaks, the absorption of a

light pulse with a bandwidth larger than Δ can be total if the optical density integrated over the photon bandwidth is high enough [Afzelius et al. 2009]. Most AFC quantum memories are realized with rare-earth doped solid state materials at cryogenic temperatures such as europium [Alexander et al. 2006], praseodymium [Sabooni et al. 2010; Seri et al. 2019; Lago-Rivera et al. 2021], thulium [Saglamyurek et al. 2011], neodymium [Tiranov et al. 2016] or erbium [Lauritzen et al. 2010].

Λ-AFC

The Λ-AFC technique is a hybrid protocol that combines the AFC protocol with a dynamical storage into a long-lived state using a strong control beam. This approach is called Λ-AFC in reference to the hybrid combination of a Λ-type three-level system and the AFC protocol. This combination allows to keep the advantages of AFC storage while allowing for on-demand storage. The Λ-AFC storage is initiated by an AFC absorption followed by the use of a strong control beam to map the coherence into an atomic spin-wave. Another control beam is applied when the signal needs to be read out, which resumes the atomic rephasing leading to the emission of the signal. Since these memories are based on AFC, their implementation is mostly realized in doped solid-state crystals [Afzelius et al. 2010; Jobez et al. 2015; Jobez et al. 2016; Rakonjac et al. 2021].

Other photon-echo techniques

The ability to actively control an inhomogeneous medium thanks to the use of an electric or magnetic field allows for the realization of photon-echo memories also called controllable-reversible inhomogeneous broadning (CRIB) memories. The idea relies on the time reversal of light absorption which can be triggered by the reversal of the medium broadening [Tittel et al. 2010]. This technique originates from a proposal that generates photon-echoes despite Doppler broadening in hot vapours [Moiseev and Tittel 2011]. Since then, this technique has been extended to solid-state rare earth ions [Chanelière and Hétet 2015] and also lead to the development of gradient-echo memory (GEM) in cold atomic systems [Higginbottom et al. 2015; Cho et al. 2016].

Emissive memories

Some heralding protocols such as DLCZ [Duan et al. 2001] or spin-photon entanglement in NV-centers [Bernien et al. 2013] constitute quantum memories slightly different than all the above protocols since no quantum state is input into the memory. The idea is based on the *heralding* of a long-lived state which can be read-out at a later time. While these memories can not store an input pulse, they are useful to generate remote entanglement between systems [Pompili et al. 2021; Bernien et al. 2013; Humphreys et al. 2018; Chou et al. 2005]. A detailed explanation of the DLCZ protocol can be found in Chapter 4 of this thesis, as it can also be used as a tunable single-photon source.

Other types of schemes

The simplest scheme for a quantum memory is an optical fiber loop. This simple system can be considered a quantum memory with a pre-programmed delay which is determined by the

length of the loop. A cavity can also be considered a quantum memory since it can store a photon during the number of round trips. However it is impossible to know when the photon escapes the cavity which makes it unpractical for applications. Nevertheless some groups have developed cavities with on-demand release of the stored photon using a Pockels-cell [Bouillard et al. 2019] that proves to be useful for continuous-variable processing and state engineering.

3.4 State of the art and recent advances in memory platforms

In this subsection we review the state of the art of two of the most-used platforms for quantum memories. We focus on the most relevant properties for quantum applications such as efficiency, multimode capacity and lifetime.

Cold alkaline atoms

A promising platform for quantum memory experiments is cold atomic ensembles of alkaline species such as ^{87}Rb or ^{55}Cs. They offer the advantage of being a well-known and easily controllable system with limited inhomogeneous broadening. This platform is mainly used for dynamical EIT memories and DLCZ heralding preparation. Using dynamical EIT, the first storage experiments in the quantum regime using cold atoms were realized in the mid-2000's [Chanelière et al. 2005] ($\eta_m = 6\%$, $\tau_m = 8\mu s$) and were quickly followed by the first storage of entanglement in 2008 [Choi et al. 2008] ($\eta_m = 17\%$, $\tau_m = 8\mu s$). These first achievements were marked by their low storage-and-retrieval efficiency and by relatively low storage times. At that time, with the goal of increasing the capabilities of these memories, a lot of effort was put to understand the scaling of efficiency from a theoretical point of view [Gorshkov, André, Lukin, et al. 2007; Gorshkov, André, Fleischhauer, et al. 2007; Gorshkov et al. 2008; Sheremet et al. 2010]. To this day, theoretical research on this matter is still an active field, trying to understand the evolution of efficiency through pulse shaping [Nakao and Yamamoto 2017], off-resonant contamination [Hsiao et al. 2018; Vernaz Gris, Huang, et al. 2018], multimodality [Grodecka-Grad et al. 2012] or broadband operations [Shinbrough et al. 2021; Rastogi et al. 2019; Wei et al. 2020]. Alongside these theoretical developments, experimental realizations of EIT-based memories kept increasing in quality over the years as discussed in the following paragraphs.

One of the main achievements of the recent years in this platform is the realization of highly efficient quantum memories. For qubits, an experimental realization in 2018 showed a substantial improvement of nearly a factor two [Vernaz Gris, Huang, et al. 2018] ($\eta_m = 67\%$, $\tau_m = 15\mu s$) compared to other qubit storage experiments which reported efficiencies below 35%, all platforms considered [Parigi et al. 2015; Kalb et al. 2015; Clausen et al. 2011; Jin et al. 2015]. This achievement was surpassed in 2019 by the realization of a qubit EIT-memory with 86% efficiency [Wang et al. 2019] ($\eta_m = 86\%$, $\tau_m = 15\mu s$) and our work at LKB also showed the realization of a 87% efficiency memory for single photons [Cao et al. 2020] ($\eta_m = 87\%$, $\tau_m = 15\mu s$), proving EIT-quantum memories to be a good candidate for pratical applications. In this work, at the hearth of this thesis, we also shown that highly efficient entanglement transfer between two quantum memories was possible. Recently, experiments involving the EIT-storage and manipulation of single photons coming from SPDC sources have achieved high efficiencies [Tsai et al. 2020] ($\eta_m = 36\%$, $\tau_m = 10\mu s$), [Tseng et al. 2020] ($\eta_m = 70\%$, $\tau_m = 10\mu s$). In DLCZ experiments, it seems more difficult to reach these kinds

of efficiencies due to the increasing phase mismatch for long ensembles of large OD [Surmacz et al. 2008]. The best efficiency in free-space has been obtained in Kimble's group [Laurat et al. 2006] ($q_c = 50\%$). The overall spin-wave to photon conversion efficiency can be improved by placing the ensemble inside a cavity [Bao et al. 2012] ($q_c = 73\%$, $\tau_m = 3.2$ms) however it does not improve the effective efficiency of the process when considering the emission out of the cavity which was limited under 50% by the output coupler of the cavity. For detuned Raman memories in cold atoms, the efficiency has recently reached 65% using rubidium clouds of large OD [Vernaz Gris, Tranter, et al. 2018] ($q_c = 65\%$, $\tau_m = 60\mu$s). Combining Raman memories with controlled inhomogeneous broadening can also lead to highly efficient memories as demonstrated in [Cho et al. 2016] ($\eta_m = 87\%$) although this was realized in the classical regime.

Long lifetimes in alkali vapor are also widely investigated from an experimental perspective. Pumping to a specific Zeeman state enables insensitivity to the magnetic field decoherence of the collective excitation, leading to the storage times of the order of hundreds of microseconds, only limited by the temperature of the sample [Chen et al. 2013] ($\eta_m = 78\%$, $\tau_m = 98\mu s$, classical), [Xu et al. 2013] ($\eta_m = 7\%$, $\tau_m = 1$ ms). Recently, extensions of these techniques to long lived traps such as lattices and dipole traps combined with cavities have been investigated in the group of J-W Pan, proving that quantum storage with more than 100ms of storage time is compatible with EIT-based memories [Yang et al. 2016] ($\eta_m = 76\%$ inside cavity, $\tau_m = 5$ ms), [Wang et al. 2021] ($\eta_m = 76\%$ inside cavity, $\tau_m = 100$ ms). Note that the use of a cavity limits the overall retrieval efficiency and it generally does not exceed 50% considering the retrieval outside the cavity. Around ten years ago, dynamical decoupling of spin-waves has been demonstrated to be possible in cold-atomic lattice and classical storage of the order of the minute has been demonstrated [Dudin et al. 2013] ($\eta_m = 14\%$, $\tau_m = 16$ s, classical). To date, this technique was not explored further in cold atomic memories. In DLCZ platforms, the temperature problem has been shown to be unavoidable without going to a dipole trap and freezing the spin-wave to reduce its k-vector to zero thanks to a set of microwave pulses [Jiang et al. 2016] ($\tau_m = 2$ ms).

Multimodality in DLCZ and EIT-based memories is also an active field of research and it has been demonstrated that multiplexing could be performed using various degrees of freedom in these memories. The multimode capacity $\mathcal{K}$ in cold atoms is believed to be small compared to rare earth ions although the field has not totally been explored yet. In EIT memories, the principal method for multiplexing is to use spatial modes of light either using orbital angular momentum [Nicolas et al. 2014] ($\mathcal{K} = 2$), angles between signals [Cao et al. 2020; Vernaz Gris, Huang, et al. 2018] ($\mathcal{K} = 2$), [Dai et al. 2012] ($\mathcal{K} = 4$) or angles between controls [Chen et al. 2016] ($\mathcal{K} = 4$). Time multiplexing in EIT is essentially impossible because of the nature of the dynamical EIT protocol, however it is possible to store spatial modes and convert these modes into temporal ones using switching networks [Tian et al. 2017; Wen et al. 2019] ($\mathcal{K} = 4$). Recently, the development of spatial mode multiplexing using acousto-optic deflectors (AOD) [Lan et al. 2009] to address individual cells in Rb ensembles have enabled to address a large number of modes, the only drawback so far being the low efficiency for each mode [Jiang et al. 2019] ($\mathcal{K} = 210, < \eta_m >= 7\%$). These massively AOD-multiplexed memories are also performing well in DLCZ experiments [Pu et al. 2017] ($\mathcal{K} = 225$) and it has been shown that DLCZ and EIT can be interfaced in this way to multiplex entanglement generation and storage [Jiang et al. 2019] ($\mathcal{K} = 6$). In general, DLCZ seems to offer more multimode capacity than EIT by using the emission of

the heralding photon in multiple directions. This direction is investigated in Poland using spatially resolved single-photon detection [Lipka et al. 2021; Parniak et al. 2017] ($\mathcal{K} = 665$). Multiplexing using time-bins is also a possibility in DLCZ using a low-finesse cavity around the atomic ensemble [Heller et al. 2020] ($\mathcal{K} = 6$).

Broadband operation in cold atoms have also seen substantial improvement in recent years. While Raman memories offer the possibility to store classical pulses of short durations Δt [Bao et al. 2012; Vernaz Gris, Tranter, et al. 2018] ($\Delta t = 200$ ns), the first demonstrations of true single-photon storage with high bandwidth in cold atoms [Ding, Zhang, Zhou, Shi, Xiang, et al. 2015; Ding, Zhang, Zhou, Shi, Shi, et al. 2015] ($\Delta t = 100$ ns) represent an important advance in this effort. Recently, it has been shown that broadband pulses around 20 MHz linewidth could be stored using the so called Autler-Townes (AT) scheme [Rastogi et al. 2019; Saglamyurek et al. 2018; Saglamyurek et al. 2019; Saglamyurek et al. 2021] ($\Delta t = 20$ ns). This AT-scheme is basically similar to EIT-memories, instead operating in a regime where the control power is very high. Similar studies where performed in Chen's group with the realization of a broadband classical memory with high efficiency [Wei et al. 2020] ($\Delta t = 20$ ns, $\eta_m = 80\%$, classical). This study is also accompanied by a comprehensive theoretical model that explains the subtleties of broadband storage with EIT and explains the emergence of a new figure of merit in this type of storage, the *waveform likeliness*.

Cold alkaline atoms therefore seem to be a viable platform for realistic applications since they perform very well with each benchmark parameter. Individually, the broadband capacity and multimodality seem to be lower than other platforms but the memory efficiency outperforms any other platform. Although each figure of merit could potentially reach high values in this type of systems, devising a quantum memory that simultaneously performs well on all fronts remains a true experimental challenge. For example, optimizing both efficiency and lifetime seems to be possible by trapping the atoms in lattices and using cavities, though it might lead to a decrease in terms of multimode capacity. Nevertheless, the multimodal aspects of EIT storage has yet to be deeply explored and it is possible that new types of spatial multiplexing might appear in the years to come. Our team at LKB is currently investigating the parallel storage of Hermite-Gaussian modes using EIT.

Rare-Earth Ions

Rare-earth ions have also proven to be a strong candidate for quantum memory platforms. Their attractiveness lies in unprecedented coherence time and large multimode capacity, both in the time and frequency domain. Protocols such as AFC, EIT and Λ-AFC are usually performed with such platforms.

One of the main way to increase the storage time in rare-earth ions is to use dynamical decoupling to counter decoherence by taking advantage of time-dependent control pulses [Viola and Lloyd 1998]. This technique can lead to storage time of the order of the minute in the classical domain, as demonstrated with EIT [Heinze et al. 2013] ($\tau_m = 40$s, classical). A storage time at this scale has recently been extended to Λ-AFC protocols [Holzäpfel et al. 2020] ($\tau_m = 0.5$s, classical) although it still needs to be demonstrated at the quantum level [Jobez et al. 2015] ($\tau_m = 1$ms).

Rare-earth ions also display high multimode capacity at the quantum level [Afzelius et al. 2009]. A first way to multiplex these memories is to encode information in the frequency domain [Sinclair et al. 2014] ($\mathcal{K} = 26$). It is also possible to harness the temporal degree-

of-freedom to multiplex the storage thanks to the nature of the AFC protocol [Jobez et al. 2016] ($\mathcal{K} = 100$), [Laplane et al. 2017] ($\mathcal{K} = 17$) and it has been proven to be useful for storing entanglement [Tiranov et al. 2016] ($\mathcal{K} = 2$). It is also possible to combine spectral and temporal multiplexing [Seri et al. 2019] ($\mathcal{K} = 15 \times 9$) and even adding another spatial multiplexing degree of freedom [Yang et al. 2018] ($\mathcal{K} = 2 \times 2 \times 3$).

For an AFC memory without cavity, the theoretically maximum achievable efficiency is 54% [Afzelius et al. 2009], limited by reabsorption in the crystal. To overcome this limitation, research focuses on the implementation of impedance matched cavities [Afzelius and Simon 2010]. In this endehavour, some experiments have reported efficiencies breaking the 54% limit [Sabooni et al. 2013] ($\eta_m = 56\%$), [Jobez et al. 2014] ($\eta_m = 53\%$). Using EIT in multipass configuration, higher efficiencies have been demonstrated in the classical regime [Schraft et al. 2016] ($\eta_m = 76\%$).

Rare-earth ions are also a promising platform for quantum network applications. Their high multimode capacity, which could theoretically reach more than one thousand modes if all degrees of freedom are combined, compensate for their so far limited storage-and-retrieval efficiency. Another advantage of this platform is the high bandwidth capacity of storage that can go up to 10GHz for specific types of crystals [Vivoli et al. 2013].

4 Scaling of memory parameters in repeater protocols

In order to illustrate the importance of quantum memories in quantum repeater schemes, we finally discuss the roles of several memory parameters on the performance of repeaters. We explore a simplified model of a repeater chain where we study the probability of successfully entangling the whole chain as a function of lifetime, efficiency and multimode capacity. This toy model does not aim to give realistic values of distribution time, but rather give a reasonable idea of how the probabilities scale. In this section, we consider a simple model of a repeater chain composed of elementary segments as represented in Fig. 1.3. We carry this study out step by step. We start from a perfectly efficient memory but with finite lifetime, we then add inefficiencies to the storage and retrieval process and finally add multiplexing capabilities to the memories. At each step, we discuss the scaling of the repeater performance with memory parameters.

4.1 Quantum link efficiency

To emphasize on the importance of a quantum memory in this section, we consider a somewhat ideal case. We suppose that the generation of entanglement in each segment is deterministic such that for each trial, we have a single-event detection on the Bell-state measurement (BSM) of Fig. 1.2a (one heralding event per trial). However, we consider the losses induced by the fiber propagation in each elementary segment, which means that entanglement is not necessarily delivered at each trial, even though a heralding event occured. This distinction is important to understand the discussion.

We have seen in Sec. 2.2 that if we implement a quantum repeater scheme without supplying quantum memories to the N_0 elementary segments, the probability to entangle every segment is the same probability as to entangle the whole link via the propagation of one photon pair through a fiber. If we assume a fiber transmission of $T = 95\%/\text{km}$, this probability is equal to $p_{link} = T^L$, with L the distance of the whole link. Now, suppose

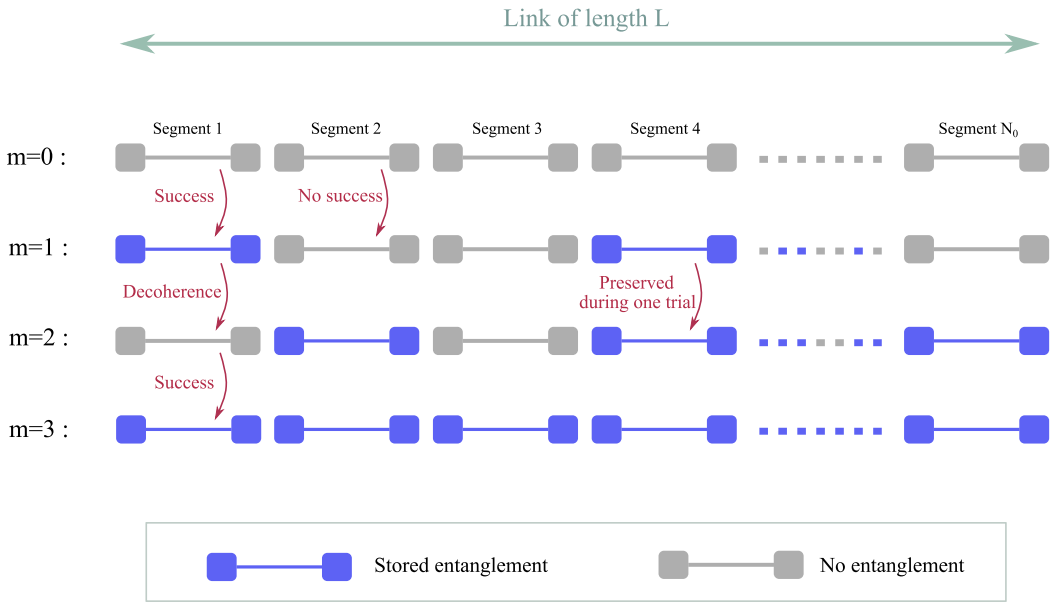

Fig. 1.3 *A repeater chain consisting of N_0 elementary segments. During each trial m, entanglement is attempted to be generated and stored in the memories of each segment. Entanglement can sometimes be lost between each trial due to decoherence of the memory. In this example, each segment has stored entanglement after m=3 trials. We are interested in the probability $\mathcal{P}(M)$ to have suceeded at least once in entangling every N_0 segments of the quantum repeater after performing M trials.*

that each elementary segment has the ability to store the generated entanglement with a lifetime which is equivalent to the time it takes to perform a number M_{deco} of entanglement generation trials. The probability to generate entanglement (and deliver it) in an elementary segment is unchanged and writes $p_{seg} = T^{L/N_0}$.

However, the average number of non-entangled elementary segments $N(m)$ now depends on the number of entanglement trials m. We identify two contributions to this number. The first one represents the number of segments which have not been entangled after the (m)-th trial and can be written: $N(m-1) - N(m-1)p_{seg}$. It is indeed the average number of unentangled segments after the $(m-1)$-th trial, minus the average number of segments that get entangled during the (m)-th trial. The second contribution comes from the decoherence of the memory. We introduce the probability p_{deco} that an entangled segment looses its entanglement between two trials. This probability is equal to $p_{deco} = 1/M_{deco}$ since M_{deco} is the number of entanglement trials it takes to reach the average time of entanglement loss due to decoherence of the memory. The number of entangled links that decohere between each trials is therefore equal to $[N_0 - N(m-1)]\, p_{deco}$. Finally, the average number of non-entangled elementary segments $N(m)$ after the m-th trial can be written:

$$N(m) = N(m-1) - N(m-1)p_{seg} + [N_0 - N(m-1)]\, p_{deco}. \tag{1.7}$$

It is interesting to note that the decoherence probability between each trial p_{deco} can also be

written as

$$p_{deco} = \frac{1}{\eta_{link}} \qquad \text{if} \qquad \eta_{link} \geq 1 \tag{1.8}$$

where η_{link} is called the *quantum link efficiency* and corresponds to the ratio of the lifetime of the entanglement in the segment and the times it takes to create an entangled pair.

$$\eta_{link} = \text{lifetime} \cdot \text{entanglement rate}. \tag{1.9}$$

The probability to deliver entanglement in every segment of the whole link at the m-th trial is therefore equal to

$$P(m) = (p_{seg})^{N(m)}. \tag{1.10}$$

Finally, the probability to have suceeded at least once in delivering entanglement in every segments *after* performing M trials writes

$$\mathcal{P}(M) = 1 - \prod_{m=1}^{M} [1 - P(m)] \tag{1.11}$$

We observe from this expression that $\eta_{link} \gg 1$ yields a faster increase of this probability $\mathcal{P}(M)$ as a function of M, regardless of any other parameter. In other terms, it means that the probability to have suceeded at least once in entangling every segment after a number M of attemps increases when η_{link} increases. This illustrates the requirement that entanglement should be produced much faster than it is lost. This is one of the main challenges in the field, which pushes the single photon sources to increase their rate, and the quantum memories to increase their lifetime.

4.2 Memory efficiency

To further improve this discussion, we must now introduce the fact that a memory can be inefficient. Based on the previous calculations, we note that $\mathcal{P}(M)$ can be optimized by arbitrarily increasing the number of elementary segments N_0 of the link. Indeed, if $N_0 \sim \infty$, the probability to succesfully get entanglement in one segment $p_{seg} \sim 1$ since there is no propagation loss. This disappears with the introduction of inefficencies.

The connection of the end-nodes via entanglement can only be done after the entanglement-swapping stage of the repeater. It means that, after each elementary segment of the link has delivered entanglement to its memories, we need to *read-out* the memories and perform a BSM between each adjacent read-out memories. For simplicity, we will still suppose that the BSM is lossless and we only consider the losses induced by the read out of the memory, called the *retrieval efficiency*, noted η_{mem}.

From these considerations, one can see what happens to the probability of delivering entanglement to the end-nodes of the link when N_0 varies. There are $2N_0$ memories that need to be read-out (or N_0 depending on the type of entanglement we consider), which means that the probability of succesfully reading out all the memories is $(\eta_{mem})^{2N_0}$. In the end, the cumulative efficiency of the quantum repeater noted $\rho(M)$, and expressed as the probability to have distributed entanglement at least once between the two end-nodes after M trials can be written:

$$\rho(M) = 1 - \prod_{m=1}^{M} \left[1 - P(m) \cdot (\eta_{mem})^{2N_0}\right]. \tag{1.12}$$

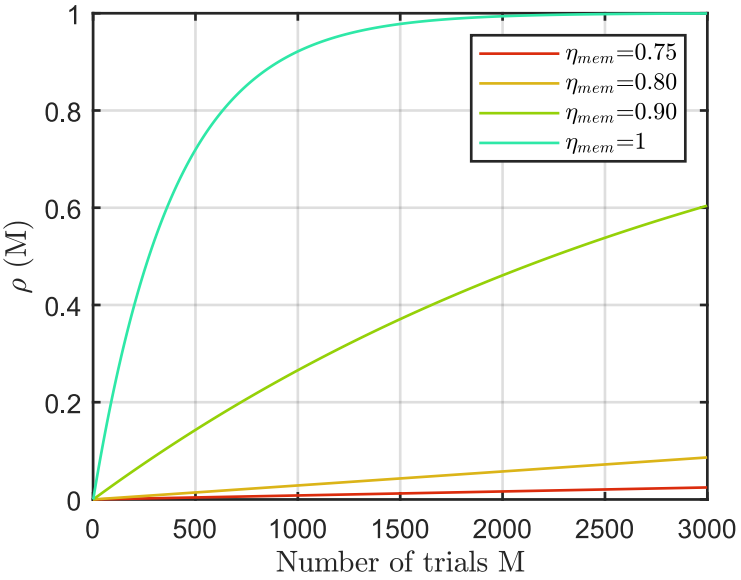

Fig. 1.4 *Probability $\rho(M)$ to have suceeded at least once in entangling every N_0 segments of the quantum repeater and succesfully read-out all memories to perform entanglement swapping, after performing M trials, as a function of M. Here we set a total length $L = 200$km, the total number of segments $N_0 = 10$ and the quantum link efficiency $\eta_{link} = 2$. We plot $\rho(M)$ for different values of memory retrieval-efficiency η_{mem}. We observe the importance of memory efficiency in quantum repeaters protocols.*

First, we note that there is a single value of N_0 that optimizes $\rho(M)$ for a given M. This is due to the fact that a trade-off must be found between p_{seg} which decreases as N_0 decreases, and the probability of successfully reading out all memories $(\eta_{mem})^{2N_0}$, that increases when N_0 decreases. This optimized N_0 depends on L, η_{mem} and η_{link}. This fact is of great importance since it highlights the importance of the *architecture* design of a quantum repeater. For example, with $\eta_{link} = 2$ and L=200 km, the optimal number of segments is $N_0 = 1$ for $\eta_{mem} = 75\%$, $N_0 = 7$ for $\eta_{mem} = 80\%$ and $N_0 = 11$ for $\eta_{mem} = 90\%$. In real conditions, you need to add losses in the BSM and in the detectors which generally reduces the overall efficiency, bringing the optimal value of N_0 closer to 1. This means that it is not possible to improve the rates compared to direct transmission if the sum of all efficiencies is low.

Then, we run the simulation for several values of memory retrieval efficiency, considering a link of length $L = 200$ km, a quantum link efficiency of $\eta_{link} = 2$ and a number of elementary segments of $N_0 = 10$. These conditions optimize the probabilities for a memory of 90% efficiency, as explained in the previous paragraph. This illustrates the importance of memory efficiency in quantum repeater protocols as it is presented in Fig. 1.4. In this configuration, the number of trials required to achieve $\rho(M) \geq 50\%$ is represented for several memory efficiencies on Fig. 1.5. The behaviour is quasi-linear in logarithmic scale and it shows that loosing 10% of efficiency multiply the time to achieve $\rho \geq 50\%$ by a factor of

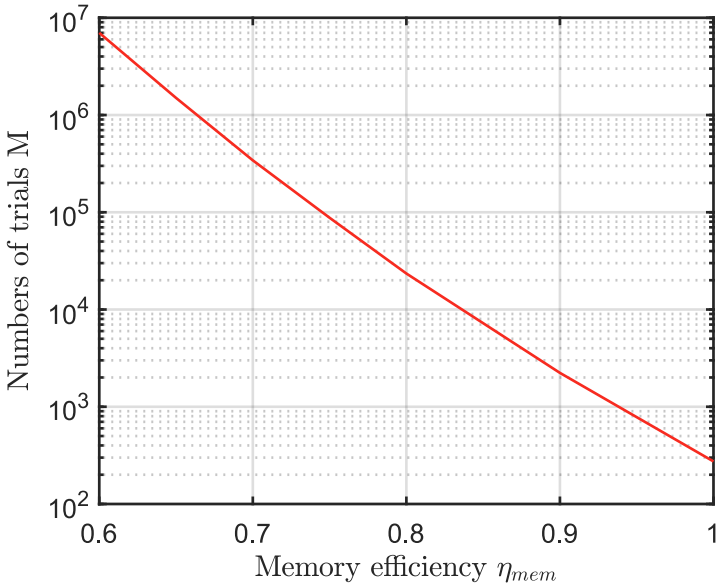

Fig. 1.5 *Numbers of trials M required to get $\rho(M) \geq 50\%$, for different memory efficiencies in the situation where $N_0 = 10$, $\eta_{link} = 2$ and $L = 200$km. We observe that loosing 10% of efficiency leads to a lower entanglement rate by one order of magnitude.*

~ 10. As an example, an increase from 70% to 90% efficiency would boost the rate by a factor 250.

In the study of N. Sangouard and collegues [Sangouard et al. 2011], they predicted a rate increase of a factor 20 for the best repeater scheme between 70% and 90% memory efficiency, which is one order of magnitude lower than what we find with this illustrative model. In this study, they did not explicitely considered a quantum link efficiency value in their protocol which might impact the scaling in general. On the other hand, we opted for a number of link $N_0 = 10$ larger than what they considered and did not consider a specific scheme for the elementary segments. Our toy model is more directed towards illustrative purposes, to easily grap the importance of memory parameters in repeater schemes.

4.3 Multiplexing

One way to increase the efficiency of a quantum repeater relies on the ability to multiplex the entanglement generation in elementary segments. For each trial, we consider that an elementary segment tries to store entanglement via a number $\mathcal{K}$ of modes. For simplicity, we still consider that the BSM heralding station of a segment clicks once per trial and per mode. We consider that Bell-state measurements cannot be performed between different modes and thus the probability to get a full link of entangled segments of a specific mode at least once $\rho(\mathcal{K},M)$ after M trials is:

$$\rho(\mathcal{K},M) = 1 - [1 - \rho(M)]^{\mathcal{K}} . \tag{1.13}$$

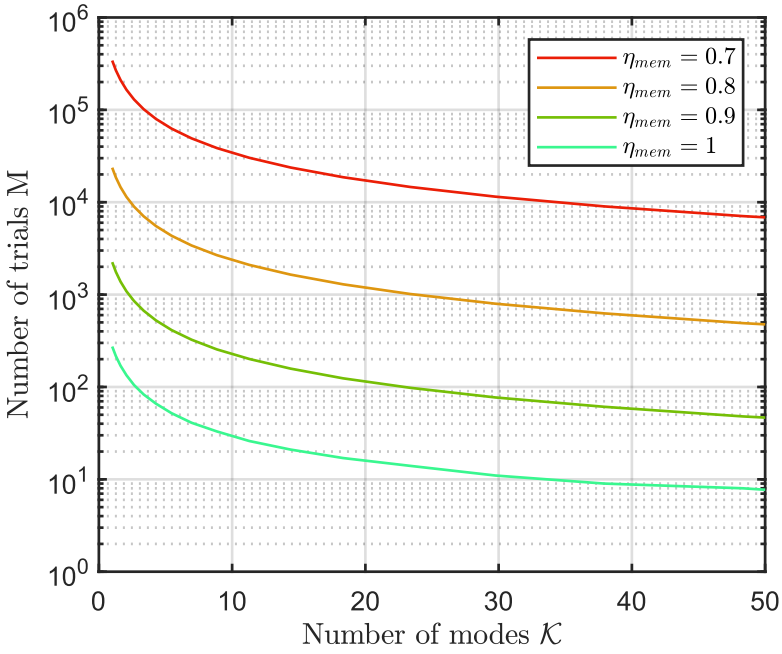

Fig. 1.6 *Numbers of trials M required to obtain $\rho(\mathcal{K},M) \geq 50\%$, for different memory efficiencies, as a function of the number of modes $\mathcal{K}$ in the situation where $N_0 = 10$, $\eta_{link} = 2$ and $L = 200km$.*

We plot on Fig. 1.6 the minimum number of trials required to obtain $\rho(\mathcal{K},M) \geq 50\%$ as a function of the number of available modes. We consider the same length, quantum link efficiency and number of segments than in the previous section ($L = 200$km, $N_0 = 10$, $\eta_{link} = 2$). We observe that there is an significant improvement with increasing $\mathcal{K}$. Independently of the memory efficiency, one order of magnitude can be won on the entanglement rate of the whole link if the number of modes is set to $\mathcal{K} = 10$. This shows that a significant improvement can be achieved by multiplexing the entanglement generation and the memory mode capacity.

However, it also shows that pushing the experimental capabilities to only $\mathcal{K} \sim 10$ modes is already a giant step towards functional quantum networks. Indeed, it shows that going from ten to a hundred modes is not game changing since all the significative improvement is made by the first few tenth of modes. The efficiency is nevertheless a crucial parameter since for example, the number of modes of repeater with a memory of efficiency $\eta_{mem} = 0.8$ required to obtain the same entanglement rate than a repeater with a memory efficiency of $\eta_{mem} = 0.9$ and a multimode capacity of $\mathcal{K} = 10$ is $\mathcal{K} \sim 1000$ modes. However, here we only considered the multimodality as a way to parallelize the process and did not consider the ability to perform entanglement swapping BSM between different modes. The scaling would be further improved if this capability was included.

4.4 Discussion

Note that this simulation considered lossless Bell-state measurements for entanglement swapping, which is not at all the case in practice. The inclusion of losses in BSM can be simulated by adding a multiplicative factor to $P(m)$ in eq. 1.12, which would also scale as a power of N_0. This means that losses in BSM have a relatively similar effect to the memory efficiency in decreasing the rate of entanglement generation over a whole repeater link. Using the scheme proposed in Fig. 1.2 inherently makes the BSM of repeater nodes limited to 50% efficiency. This is due to the fact that the stored entangled state in each segment is the Bell-state $|01\rangle + |10\rangle$. The BSM required to perform entanglement swapping has therefore four outcomes where two of them destroy the entanglement (either a double click detection or a double vacuum detection), there are thus two outcomes out of four that effectively transfer the entanglement. However, some schemes were proposed to increase the efficiency of BSM which can reach unity in theory [Furusawa et al. 1998]. Besides, this simple model did not consider the inclusion of noise in the process. Noise can happen in the memory read-out but also in the BSM. It generally has the effect of reducing the quality of entanglement.

Besides, the model proposed here is based on the average of quantities in order to get analytic formulas. In order to check the accuracy of this approach, a computer simulation of this model was also made by considering the N_0 segments as booleans. By using random numbers to simulate their flip to the entangled-state and decoherence to the not-entangled state, the same scaling for $\mathcal{P}(M)$ and $\rho(M)$ at low M was recovered. However, since the time to perform the simulation grows exponentially with N_0, M and $\mathcal{K}$, it was impossible to perform the simulation for high values of M, justifying the use of this averaged model.

5 Conclusion

In this chapter we introduced the basis of quantum information and quantum communication research. The motivation for quantum communication and quantum memories development has been detailled through the explanation of the functionning of an hypothetical quantum internet made of nodes and channels. State of the art of quantum memories properties has been presented, with the goal of presenting the current state of the research to the reader. Finally, we analyzed the influence of memory parameters such as efficiency, lifetime and multimode capacity on the scaling of a quantum repeater chain using a toy model. Among others, we identified that improving the efficiency of quantum memories that have the ablility to store entanglement is a crucial requirement for a fully fledged quantum repeater. For instance, an increase from 70% to 90% in efficiency would boost the entanglement delivery rate by a factor 250. This improvement in efficiency has been experimentally realized in this thesis as it is shown in the next Chapters.

Chapter 2

Atom-light interactions for EIT-based quantum memories

The interactions between atomic ensembles and light is a core subject of this thesis. In this chapter we start by describing the interactions in a classical and quantum framework, defining useful quantities along the way such as the optical depth or the susceptibility. We then focus on an ensemble of three-level atoms where we theoretically study the EIT phenomenon associated with collective excitations and storage in an atomic medium. Finally, we discuss the importance of the choice of the excited state for storage processes and we justify our choice to perform the experiments presented in the next chapters on the D_1 line.

1 Absorption of light by an atom

Light absorption by an atom is a fundamental process that is at the heart of our experiment. In this section, we give a general description of this process and define useful quantities such as the optical depth, a crucial parameter when aiming for efficient memory experiments.

1.1 Polarizability

We start by studying the response of an atom to an oscillating electric field $E_0\mathbf{u}_z exp(-i\omega t)$. We model an atom by a single electron bound to a nucleus by a harmonic force with an angular frequency of ω_0, and a damping coefficient γ corresponding to the emission of radiation by the accelerated electron. The equation of motion writes:

$$\frac{d^2\mathbf{r}}{dt^2} + \gamma\frac{d\mathbf{r}}{dt} + \omega_0\mathbf{r} = \frac{qE_0}{m}\mathbf{u}_z e^{-i\omega t} \tag{2.1}$$

with q the charge of the electron and m its mass. The steady state solution to this equation is the oscillating dipole $\mathbf{d} = q\mathbf{r} = \mathbf{d}_0 exp(-i\omega t)$ created by the moving electron with

$$\mathbf{d}_0 = q\mathbf{r}_0 = \epsilon_0\alpha_c E_0\mathbf{u}_z \tag{2.2}$$

where ϵ_0 is the vacuum permittivity and

$$\alpha_c = \frac{q^2}{m\epsilon_0}\frac{1}{\omega_0^2 - \omega^2 - i\gamma\omega} \tag{2.3}$$

is called the polarizability of the atom. Note that this polarizability has a resonant behaviour around the atomic frequency ω_0.

1.2 Scattering

As the electron is accelerated by the incoming field, it radiates in all directions. The averaged radiated power $\mathcal{P}$ is given by the Larmor formula as $\mathcal{P} = q^2\omega^4|r_0|^2/(3\pi\epsilon_0)$. Using Eq. 2.3 we get

$$\mathcal{P} = \frac{\epsilon_0}{12\pi c^3}|\alpha_c|^2\omega^4 E_0^2. \tag{2.4}$$

We compare this power to the incident power per surface $\mathcal{P}_i = \epsilon_0 c E_0^2/2$ (assuming the field considered here is a planewave) and define the scattering cross-section as the ratio

$$\sigma_c = \frac{\mathcal{P}}{\mathcal{P}_i} = \frac{8\pi}{3}r_e^2\frac{\omega^4}{(\omega_0^2-\omega^2)^2+\gamma^2\omega^2} \tag{2.5}$$

where we have introduced the classical electron radius $r_e = q^2/(4\pi\epsilon_0 mc^2)$.

We are mostly interested in the case when $\omega \approx \omega_0$. We simplify the expression of the cross section using this approximation and get :

$$\sigma_c(\omega) = \frac{8\pi}{3}r_e^2\frac{\omega_0^2}{4(\omega_0-\omega)^2+\gamma^2}, \tag{2.6}$$

which is a lorentzian of width γ. When the oscillation frequency of the field is equal to the resonant frequency of the atom $\omega = \omega_0$, we obtain

$$\sigma_c(\omega_0) = \frac{3}{2\pi}\lambda_0^2. \tag{2.7}$$

At resonance, this cross section is proportional to the square of the resonant wavelength which is much larger than the size of the atom. It means that a cloud of atoms is expected to be opaque close to resonance. However, this model has a limited validity since it assumes that the atom radiates as much power as we send inside the cross section area, which is not true in pratice. Nevertheless, this model is correct if the incoming field has a low power compared to a "saturation power" which roughly corresponds to the scattering of photons at rate γ.

1.3 Absorption in a medium

Starting from Maxwell's equations and considering a collection of independent atoms with low enough density N such that the produced field on each atom by its neighbours is small compared to the incident field, we get the following propagation equation for the amplitude of a field oscillating at ω :

$$\Delta\mathbf{E} + \frac{\omega^2}{c^2}(1+N\alpha_c)\mathbf{E} = 0. \tag{2.8}$$

This equation respectively links the dispersive phase accumulation upon propagation and the exponential attenuation of the amplitude caused by the real and imaginary part of the medium's refraction index $n = \sqrt{1+N\alpha_c}$ respectively. We call $\chi = N\alpha_c$ the susceptibility

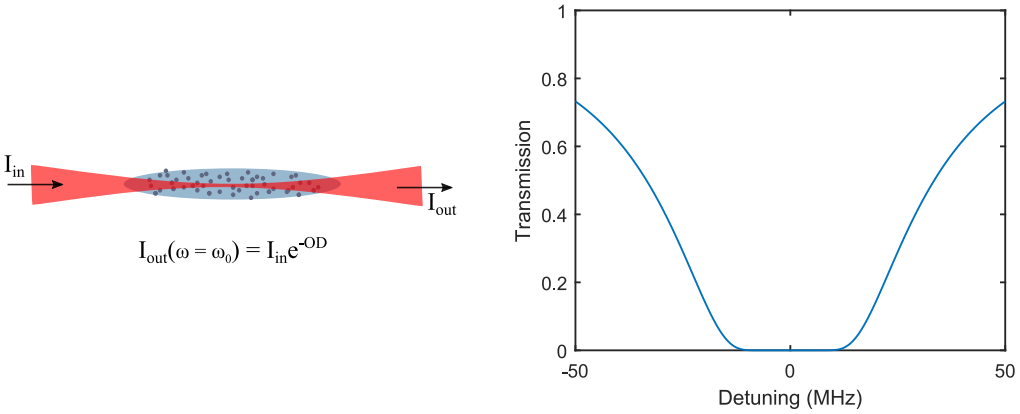

Fig. 2.1 *Optical depth. (left): An incident light with intensity I_{in} is attenuated by e^{-OD} at resonance. (right): Typical transmission profile for different detuning from resonance as given by Eq. 2.13*

of the medium, a quantity of importance when studying atom-light interactions. In the end, we can write the average density of energy transferred from the field to the atoms as

$$\mathcal{E}(\omega) = \frac{1}{2}\epsilon_0 \omega N \,\mathrm{Im}\left[\alpha_c(\omega)\right] |E_0|^2 \tag{2.9}$$

where we see that the absorption of the medium is directly proportionnal to the imaginary part of the polarizability given by:

$$\mathrm{Im}\left[\alpha_c(\omega)\right] = \frac{q^2}{m\epsilon_0} \frac{\gamma\omega}{(\omega_0^2 - \omega^2)^2 + \gamma^2\omega^2}. \tag{2.10}$$

1.4 Optical depth

The optical depth measures the absorption of a medium. It represents the fraction of light absorbed during propagation through the medium. For a resonant incoming field, we define the optical depth OD as a function of input and output intensity of a light beam by

$$\frac{I_{out}(\omega = \omega_0)}{I_{in}(\omega = \omega_0)} = e^{-\mathrm{OD}}. \tag{2.11}$$

Around resonance, the absorption can be derived from Eq. 2.9, with $\delta = \omega - \omega_0$ the detuning of the incoming field to the resonance frequency:

$$\frac{I_{out}(\delta)}{I_{in}(\delta)} = \exp\left(-\frac{\mathrm{OD}}{1 + 4(\delta/\Gamma)^2}\right) \tag{2.12}$$

where we have replaced γ by Γ, being the linewidth of the excited level. The on-resonance optical depth is thus given by

$$\mathrm{OD} = \left(1 + 4\frac{\delta^2}{\Gamma^2}\right) \ln\left(\frac{I_{in}(\delta)}{I_{out}(\delta)}\right). \tag{2.13}$$

Experimentally, if the on-resonance optical depth is large, it is usually much simpler to measure it by detuned absorption measurements since the absorption at resonance can quickly reach 100%. As explained later on in this thesis, this quantity is a crucial metric in the design of our highly efficient quantum memory.

1.5 Semi-classical description of atom-light interactions

Interaction Hamiltonian

The Hamiltonian describing the system of an atom coupled to an electric fields writes :

$$H = H_0 - \mathbf{D} \cdot \mathbf{E} \tag{2.14}$$

with $H_0 = \mathbf{P}^2/2m + qU(\mathbf{R})$ being the free atom Hamiltonian. Here $\mathbf{P}$ and $\mathbf{R}$ are the momentum and position operators for the electron and U is the electrostatic Coulomb potential binding the electron to the nucleus (or core depending on the nature of the atom). $\mathbf{E}$ is the electric field operator and $\mathbf{D} = q\mathbf{R}$ is the dipole operator. Here we describe the atom by a set of states $|i\rangle$ that are the eigenstates of H_0 with eigenvalues E_i. The lower energy state is called the groundstate $|g\rangle$. The energy difference between the ground state and an excited state $|e\rangle$ is expressed as $\hbar\omega_{eg}$ which is the energy of a photon at frequency ω_{eg}.

Two-level atom

For a two-evel atom, the full Hamiltonian in the interaction picture writes

$$\tilde{H} = \frac{\hbar\Delta}{2}\sigma_z - \frac{\hbar\Omega}{2}\left(\sigma_+ e^{-i\phi} + \sigma_- e^{i\phi}\right) \tag{2.15}$$

where we have introduced the Rabi frequency of the incoming field $\Omega = \mathbf{d} \cdot \mathbf{E}_0/\hbar$ where $\mathbf{d}$ is the dipole moment of the atom and Δ is the detuning from the field to the atomic resonance. Here, $\sigma_{x,y,z}$ are the Pauli operators and σ_+,σ_- are the increasing and lowering operators respectively. The evolution of the state of the atom coupled to light is the rotation around the axis $\mathbf{u}$ in the Bloch sphere at angular frequency $\Omega' = \sqrt{\Omega^2 + \Delta^2}$, with

$$\mathbf{u} = \frac{-\Omega\cos(\phi)\mathbf{u}_x - \Omega\sin(\phi)\mathbf{u}_y + \Delta\mathbf{u}_z}{\Omega'}. \tag{2.16}$$

Three-level atom

We now study an atom having a Λ-type level structure with state $|g\rangle$,$|e\rangle$ and another ground state $|s\rangle$ as represented on Fig. 2.2. These levels are coupled by two distinct fields, the signal field that adresses the $|g\rangle \rightarrow |e\rangle$ transition, and the control light resonant with the $|s\rangle \rightarrow |e\rangle$ transition. This configuration is of particular interest in this thesis since it allows electromagnetically-induced transparency (EIT) and storage of a signal pulse. In this framework, the Hamiltonian in interaction picture takes the following form:

$$H_{int} = -\frac{\hbar}{2}\left(\Omega_s e^{-i\omega_s t}\left|e\right\rangle\left\langle g\right| + \Omega_c e^{-i\omega_c t}\left|e\right\rangle\left\langle s\right|\right) + h.c. \tag{2.17}$$

with the $\{s,c\}$ subscript denoting the signal and control fields. This Hamiltonian has two eigenstates called bright $|B\rangle$ and dark $|D\rangle$. They can be written as $|B\rangle = \sin\theta\,|g\rangle + \cos\theta\,|s\rangle$

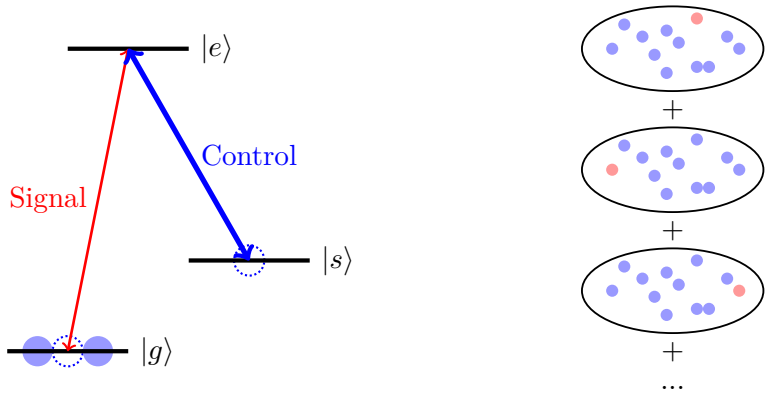

Fig. 2.2 *(left): The Λ-type system considered. A weak signal field drives the* $|g\rangle \rightarrow |e\rangle$ *transition while a strong control field drives the* $|e\rangle \rightarrow |s\rangle$ *transition. (right): An illustrated view of a collective spin excitation. One atom is in the* $|s\rangle$ *state while the others remain in the ground state. We don't know in principle which atom is excited so the corresponding state is a superposition of all contributions.*

and dark $|D\rangle = \cos\theta\,|g\rangle - \sin\theta\,|s\rangle$ with $(\cos\theta)^2 = \Omega_c^2/(\Omega_s^2+\Omega_c^2)$ and $(\sin\theta)^2 = \Omega_s^2/(\Omega_s^2+\Omega_c^2)$. We see that $H_{int}\,|D\rangle = 0$ which is the definition of a dark state since this state is completely decoupled from the light fields. If the control field is off $\Omega_c = 0$, we see that the dark state correspond to the $|s\rangle$ state.

2 Electromagnetically induced transparency

Electromagnetically induced transparency (EIT) is one of the most important features in three-level Λ-scheme atoms. First introduced in 1990 by Harris and his co-workers at Stanford [Harris et al. 1990], EIT is a quantum interference effect where an opaque atomic medium can become transparent at a given frequency [Harris 1997]. In our experiment we use it in a dynamical way to allow storage of light pulses in atomic ensembles [Fleischhauer and Lukin 2000; Fleischhauer and Lukin 2002].

2.1 Susceptibility in EIT systems

Here, we consider a collection of $\mathcal{N}$ three-level atoms, with a Λ-type level structure as in Fig. 2.2. The absorption of the signal field at detuning Δ from resonance of $|g\rangle \rightarrow |e\rangle$ is modified when a control field resonant with $|e\rangle \rightarrow |s\rangle$ is applied at the same time. As seen in Section 1.5, the combined effect of these fields brings the atom in a superposition of states $|g\rangle$ and $|s\rangle$. In this configuration, there are two different pathways (at first order) in which light can be absorbed. These two contributions can interfere destructively, leading to transparency of the signal field. In this configuration, none of the atoms are promoted to the excited state and the atoms are said to be in a dark state. We consider the case when the control field is strong and the signal field is weak. In this case, the response of the atomic ensemble can be described by the linear susceptibility (defined in Section 1.3), which can be written as:

$$\chi(\Delta) = g\mathcal{N}^2 \frac{i\gamma_{gs} + \Delta}{(\Gamma + i\Delta)(\gamma_{gs} + i\Delta) + \Omega_c^2}. \tag{2.18}$$

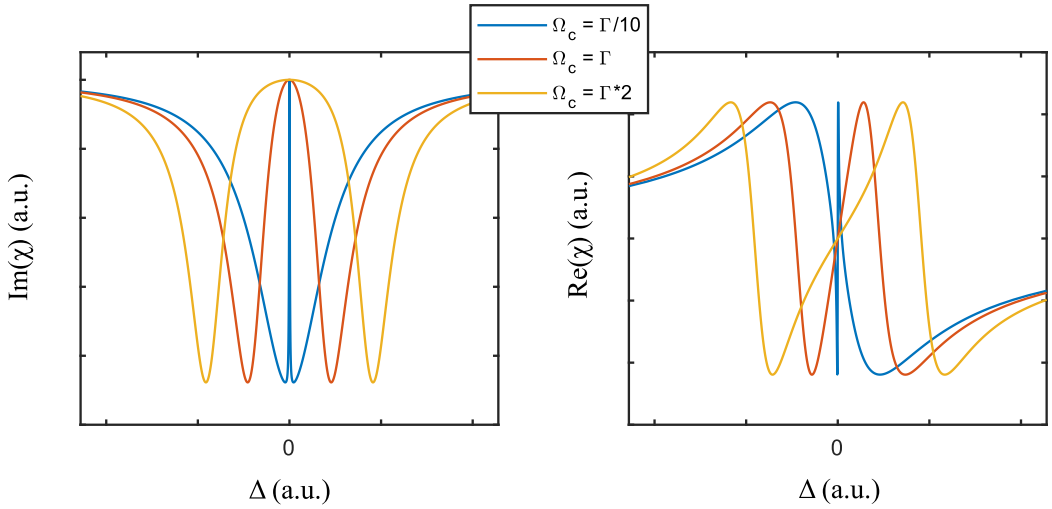

Fig. 2.3 *EIT in an atomic medium. (left): imaginary part of the susceptibility, describing the absorption properties of the medium. The transparency window is larger when the control beam is more intense. The blue regime corresponds to the EIT while the yellow curve represents the Autler-Townes regime (nearly two distinct absorption lines). (right): Real part of the susceptibility, linked to the dispersive properties of the medium. In the EIT regime, the gradient at resonance is very steep. This induces a strong reduction of the group velocity of light in the medium.*

Here, Γ is the linewidth of the excited state, γ_{gs} is the relaxation rate of the $|g\rangle \rightarrow |s\rangle$ coherence, Ω_c is the Rabi frequency of the control field and g is an atom-field coupling constant. The imaginary part of the susceptibility describes the absorptive properties of the medium and the transmission in a sample of length L can be written as:

$$T(\Delta) = e^{-\mathrm{Im}\{\chi(\Delta)\}kL}. \tag{2.19}$$

The refractive index of the medium can be written as a function of the real part of the susceptibility, and it determines the dispersive properties of the medium:

$$n(\Delta) = 1 + \frac{1}{2}\,\mathrm{Re}\{\chi(\Delta)\}. \tag{2.20}$$

We plot the imaginary and real parts of the susceptibility in Fig. 2.3. In the case where $\Omega_c \ll \Gamma$, the absorption resembles the standard Lorentzian resonance of a transition in which a narrow transparency window has been opened. When the power of the control field increases and $\Omega_c \gg \Gamma$, the transparency becomes wider up to a regime where the two halves of the spectrum can be distinguished as two well-separated resonances. These two regimes are called EIT regime and Autler-Townes regime (AT). Several studies have been dedicated to understand the fondamental differences between these two regimes [Abi-Salloum 2010; Anisimov et al. 2011] and the transition from EIT to AT was investigated in our group [Giner et al. 2013]. Quantum memory experiments are usually done in the EIT-regime although recent demonstrations have exhibited new memory schemes using AT-splitting [Rastogi et al. 2019; Saglamyurek et al. 2018; Saglamyurek et al. 2019; Saglamyurek et al. 2021].

2.2 Group velocity reduction

At resonance, the real part of the susceptibility vanishes and $n(\Delta = 0) = 1$. This implies that the phase velocity of light is equal to that in vacuum. Nevertheless, the slope of the refractive index with frequency is high around resonance, leading to a reduced group velocity compared to its vacuum counterpart c. This phenomenon is known as slow light and one of the most famous demonstration as been realized in 1999 [Hau et al. 1999] where the signal group velocity reaches a value of 17m/s in a Bose-Einstein condensate.

Considering a wave packet of frequency ω and wavevector k, the group velocity v_g is given by:

$$\frac{1}{v_g} = \frac{dk}{d\omega} \tag{2.21}$$

and from the propagation equation (Eq. 2.8), we derive the wave vector equation:

$$k(\omega)^2 = \frac{\omega^2}{c^2}\left(1 + \mathrm{Re}\{\chi(\omega)\}\right). \tag{2.22}$$

Considering the case around resonance $\Delta \simeq 0$, we have $\sqrt{1 + \mathrm{Re}\{\chi(\Delta)\}} \simeq 1$ and we then obtain the following equation:

$$v_g = \frac{c}{1 + \frac{\omega}{2}\frac{d}{d\Delta}\left(\mathrm{Re}\{\chi(\Delta)\}\right)}. \tag{2.23}$$

To first order, we have $\mathrm{Re}\{\chi(\Delta)\} \simeq 4g\mathcal{N}\Delta/\Omega_c^2$. This leads to the following expression for the group velocity of light inside the medium at resonance :

$$v_g = \frac{c}{1 + 2g\mathcal{N}\omega/\Omega_c^2}. \tag{2.24}$$

We observe that if Ω_c approaches zero, the group velocity can be made arbitrary small.

3 Storage in an atomic medium

As described previously, EIT enables slow light propagation. Nevertheless, the requirement to store a pulse of light is to stop the light by transferring its energy to the atomic ensemble. This can be done by a process called dynamical EIT. As presented in this section, the dynamics are well described by the propagation of a quasiparticle called dark-state polariton.

3.1 Dark-state polariton

The storage and retrieval of a signal pulse with EIT is well described by the propagation of a quasiparticle called dark-state polariton, a combined excitation of photons and atomic spins [Fleischhauer and Lukin 2000; Fleischhauer and Lukin 2002]. The storage process relies on the adiabatic change of control power and is sometimes called dynamical EIT. Historically, this protocol was used to realize the first memories twenty years ago [Liu et al. 2001; Chanelière et al. 2005].

To describe this system, we consider the propagating signal field as an electric-field operator $\hat{E}(z,t) = \sum_k \hat{a}_k(t)e^{ikz}$ where the sum is made over all modes with wave-vectors k.

We describe the properties of the medium by collective atomic operators:

$$\hat{e}(z,t) = \frac{1}{\mathcal{N}_z}\sum_{j=1}^{\mathcal{N}_z} |g_j\rangle\langle e_j| e^{-i\omega_{ge}t} \quad \text{and} \quad \hat{s}(z,t) = \frac{1}{\mathcal{N}_z}\sum_{j=1}^{\mathcal{N}_z} |g_j\rangle\langle s_j| e^{-i\omega_{gs}t} \tag{2.25}$$

where $\mathcal{N}_z \ll 1$ is the number of atoms contained in a small volume at position z. We model the atomic evolution by a set of Heisenberg equations $-i\hbar\frac{\delta}{\delta t}\hat{A} = \left[H_{int},\hat{A}\right]$ with H_{int} being the interaction Hamiltonian for a collection of three level atoms:

$$H_{int} = -\hbar\int \frac{dz}{\mathcal{L}}\left(\mathcal{N}g\hat{E}(z,t)\hat{e}(z,t) + \Omega_c\mathcal{N}\hat{s}(z,t)\right) + h.c. \tag{2.26}$$

Here we have modeled the strong control field as a classical field, and we have again introduced the atom-field coupling constant $g = d_0\sqrt{\frac{\omega_{ge}}{2\hbar\epsilon_0\mathcal{V}}}$ where d_0 is the dipole moment of the $|g\rangle \to |e\rangle$ transition and $\mathcal{V}$ is the quantization volume with $\mathcal{L}$ its length in the z direction. Making the assumption that the signal field is weak and that Ω_c and $\hat{E}$ change slowly in time we get at the first order in $\hat{E}$ the following set of equations :

$$\hat{e}(z,t) = \frac{-i}{\Omega_c}\left[\frac{\partial}{\partial t}\hat{s}(z,t)\right] \quad \text{and} \quad \hat{s}(z,t) = -\frac{g}{\Omega_c}\hat{E}(z,t). \tag{2.27}$$

The evolution of the pulse $\hat{E}$ is governed by the equation

$$\left(\frac{\partial}{\partial t} + c\frac{\partial}{\partial z}\right)\hat{E}(z,t) = ig\mathcal{N}\hat{e}(z,t). \tag{2.28}$$

The solution to this system of equation is a quantum field $\hat{\Psi}(z,t)$ which is a superposition of photonic $\hat{E}(z,t)$ and atomic $\hat{s}(z,t)$ components:

$$\hat{\Psi}(z,t) = \cos\theta\hat{E}(z,t) - \sin\theta\sqrt{\mathcal{N}}\hat{s}(z,t) \tag{2.29}$$

with

$$\cos\theta = \frac{\Omega_c}{\sqrt{\Omega_c^2 + g^2N}} \quad \text{and} \quad \sin\theta = \frac{g\sqrt{\mathcal{N}}}{\sqrt{\Omega_c^2 + g^2N}}. \tag{2.30}$$

The evolution of the field is described by the following equation of motion:

$$\left(\frac{\partial}{\partial t} + c\cos^2\theta\frac{\partial}{\partial z}\right)\hat{\Psi}(z,t) = 0, \tag{2.31}$$

which describes the propagation of a soliton with group velocity $v_g = c\cos^2\theta$. Note that this derivation is done in the ideal case, not considering decoherence effects that can reduce the amplitude of the polariton over the storage time.

3.2 Dynamical EIT

We observe in Eq. 2.29 that the properties of the dark-state polariton $\hat{\Psi}(z,t)$ can be modified by changing the intensity of the control field. The idea for a quantum memory relies in this ability to dynamically control $\Omega_c(t)$. In particular, when the control beam is turned off, $\Omega_c = 0$ and the polariton becomes purely atomic:

$$\hat{\Psi}(z,t) = -\sqrt{\mathcal{N}}\hat{s}(z,t). \tag{2.32}$$

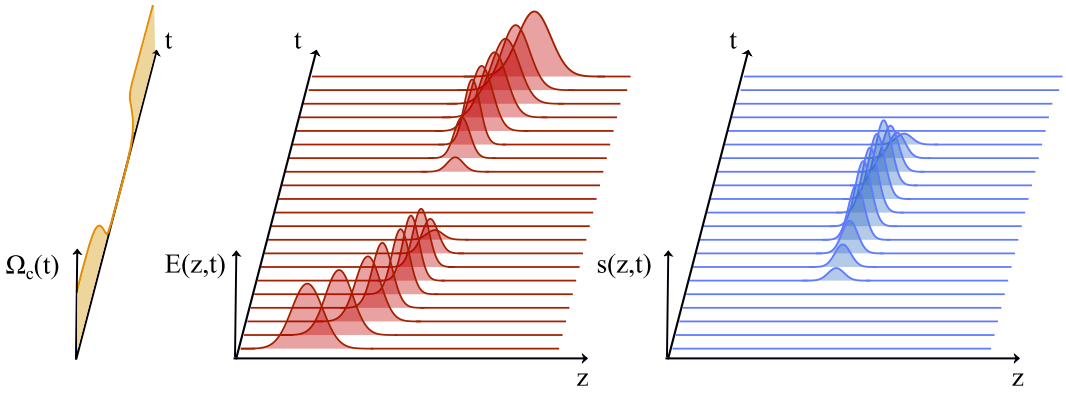

Fig. 2.4 *Dynamical EIT and dark-state polariton. Turning the control on and off allows the storage of an input signal pulse $E(z,t)$. When the signal enters the medium, it spatially compresses due to group velocity reduction. When the control is turned off, the photonic component of the dark-state polariton vanishes and the excitation is fully mapped into a collective excitation. The control is turned on again in order to retrieve the signal pulse in its photonic form, out of the ensemble.*

The input photonic state is therefore fully mapped to a collective excitation, and the polariton's group velocity is reduced to zero. After some time, the stored quantum state can be retrieved by "reaccelerating" the stopped polariton, i.e., turning the control field back on. The photonic pulse will then emerge out of the ensemble after the polariton reaches the end of the cloud and this recall can be obtained on-demand thanks to the classical control over Ω_c. This process is illustrated in Fig. 2.4.

4 Collective spin excitations

When the light pulse is stored in the medium, the state of the atomic ensemble is represented by a collective excitation, also called spin-wave. This state is subject to decoherence, which has important consequences in the storage performance. In this section we first define the collective excitation state, present the mechanisms of its decoherence and deduce an estimation of the coherence time we should achieve in our system.

4.1 Definition

Collective excitations are at the center of the EIT-based quantum memory since it represents the state of the atoms when the input signal has been stored in the ensemble. We consider here a three-level Λ-type system as shown in Fig. 2.2. Two ground states denoted as $|g\rangle$ and $|s\rangle$ are coupled through an excited state $|e\rangle$. The transition $|g\rangle \rightarrow |e\rangle$ is driven by the so-called signal weak pulse and the transition $|s\rangle \rightarrow |e\rangle$ is driven by a strong control beam of Rabi frequency Ω. For a large ensemble of $\mathcal{N}$ identical 3-levels atoms, a collective excitation corresponds to an excitation of a single atom from $|g\rangle$ to $|s\rangle$. It is impossible in principle

to determine which atom has been excited and the resulting state is a sum of all possible contributions. The corresponding state can be written as follows:

$$|\overline{s}\rangle = \frac{1}{\sqrt{\mathcal{N}}}\sum_{i=1}^{\mathcal{N}}|g_1,...,s_i,...,g_{\mathcal{N}}\rangle = \frac{1}{\sqrt{\mathcal{N}}}\sum_{i=1}^{\mathcal{N}}\hat{s_i}^{\dagger}|g_1,...,g_{\mathcal{N}}\rangle \tag{2.33}$$

where $\hat{s_i}^{\dagger}$ represents the creation operator associated to the $|s\rangle$ state of the i-th atom.

4.2 Decoherence mechanisms

Decoherence represents the loss of information of a system coupled to an environment. From the system's point of view, the dynamics are non-unitary and the process is therefore irreversible. Collective excitations are subject to decoherence which in the context of a memory experiment degrades the overall performance of the process. We usually evaluate our memory by the efficiency of storage and retrieval η_m. The efficiency of a memory corresponds to the probability of retrieving the initial signal optical pulse. It is expressed as $\eta_m = \eta_s\eta_r$, with $\eta_{s(r)}$ the storage (retrieval) efficiency. This quantity depends on time and η_r is proportionnal to $|\langle\overline{s}(0)|\overline{s}(t)\rangle|^2$. Note that compared to other states, a collective excitation is very stable. First of all, it is not subjected to spontaneous emission because it does not have $|e\rangle$ components. Moreover, if one atom is lost, the resulting state overlaps almost exactly with the previous one (with an error $1/\mathcal{N}$).

Decoherence in collective excitations can be described by a dephasing phase term for each contribution of the state:

$$|\overline{s}(t)\rangle = \frac{1}{\sqrt{\mathcal{N}}}\sum_{j=1}^{\mathcal{N}}e^{i\varphi_j(t)}\hat{s_j}^{\dagger}|g_1,...,g_{\mathcal{N}}\rangle \tag{2.34}$$

where $\varphi_j(t)$ depends on time and has a value that can be different for each atom. We discuss in the following paragraph the different sources of decoherence and their characteristic time as it appears in the efficiency η_m. From Eq. 2.34, we see that $\eta_m(t)$ takes the following form:

$$\eta_m(t) = |\langle\overline{s}(0)|\overline{s}(t)\rangle|^2 = \left|\frac{1}{\mathcal{N}}\sum_{i=1}^{\mathcal{N}}e^{i\varphi_i(t)}\right|^2 \tag{2.35}$$

which by taking the continuous limit turns into :

$$\eta_m(t) = \left|\int n(\varphi(t))e^{i\varphi(t)}d(\varphi(t))\right|^2 \tag{2.36}$$

where $n(\varphi(t))$ is the distribution of the phases at time t.

Motional dephasing

If the angle between the control and the signal field is not zero, the spin-wave dynamics is also dictated by the spatial coherence $\Delta\mathbf{k} = \mathbf{k}_s - \mathbf{k}_c$ of the collective excitation which accounts for the energy conservation of the process. If the atoms are not at rest, we can assume a linear motion for each atom such that $\mathbf{r}_i(t) = \mathbf{r}_i + \mathbf{v}_i t$ for the i^{th} atom during

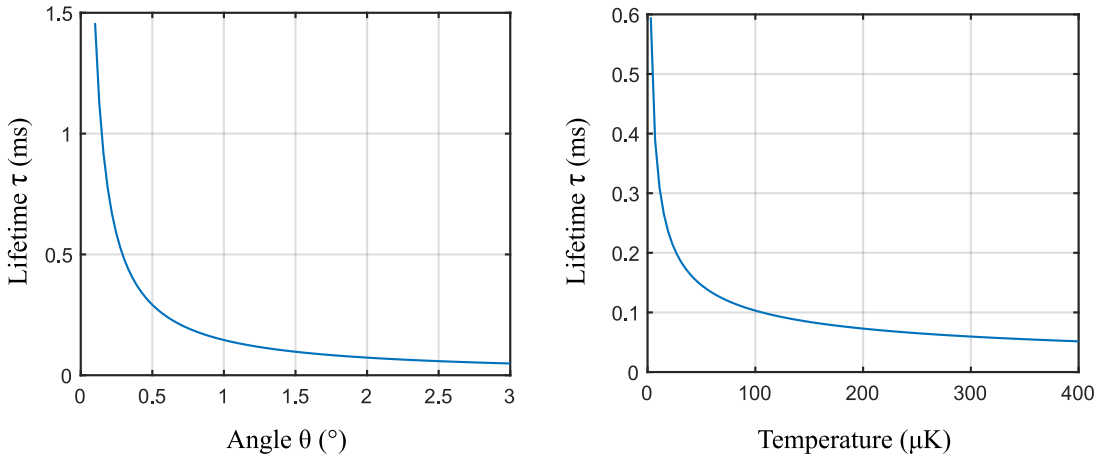

Fig. 2.5 *Motional decoherence of collective excitation. (left): The lifetime of the collective excitation as a function of the angle between the signal and control. This graph is plotted for a temperature of the atoms of 50 μK. (right): Lifetime as a function of temperature. This graph is plotted for an angle of 1 degree. For a 50 μK atomic cloud and an angle of 1 degree, lifetime of the order of 150 μs is expected for the motional decoherence.*

storage, where $\mathbf{r}_i$ is the position of the ith atom at $t = 0$. We can write the dephasing term as :

$$\varphi_i(t) = \Delta\mathbf{k} \cdot (\mathbf{r}_i + \mathbf{v}_i t) \tag{2.37}$$

If we consider a small angle we can write $|\Delta\mathbf{k}| = 2\pi \frac{sin\theta}{\lambda}$. The retrieval efficiency η_r can now be estimated as a function of time:

$$|\langle\overline{s}(0)|\overline{s}(t)\rangle|^2 = \left|\frac{1}{\mathcal{N}}\sum_{i=1}^{\mathcal{N}} e^{i\Delta\mathbf{k}\cdot\mathbf{v}_i t}\right|^2 = \left|\int f(v) e^{i\Delta\mathbf{k}\cdot\mathbf{v}t} dv\right|^2 \propto exp\left(\frac{-t^2}{\tau^2}\right) \tag{2.38}$$

where $f(v)$ is the Maxwell-Boltzmann distribution and

$$\tau = \sqrt{\frac{m}{k_B T}} \frac{\lambda}{2\pi sin\theta}. \tag{2.39}$$

As expected, temperature plays an important role in this motional decoherence effect. Cooling the atoms can therefore significantly increase the storage time of the memory. We also see that in the case of copropagating beams the phase term vanishes (if we neglect the norm difference of $|\mathbf{k}_s|$ and $|\mathbf{k}_c|$). Experimentally, it is required however to misalign the lasers on purpose in order to filter out the control beam from the signal pulse which is usually at the single-photon level. We generally work in a close angle configuration $\theta \sim 1°$ so that we can efficiently filter out the signal pulse from the control beam, and keep a high value for τ. In Fig. 2.5, we plot the lifetime of the collective excitation for different temperatures and angles. Considering an atomic cloud at $T = 50$ μK and an angle of 1 degree, coherence time is of the order of 150 μs. In our case, this is not the limiting factor.

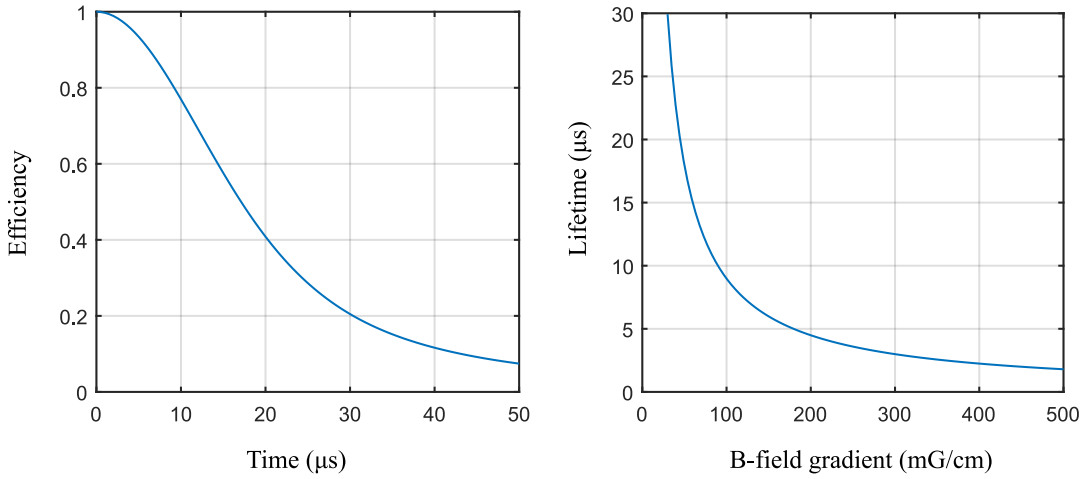

Fig. 2.6 *Decoherence of the collective excitation induced by residual magnetic field. (left): Decay of the retrieval efficiency as a function of time. This curve is the result of Eq. 2.42 taking the contribution of all Zeeman levels, with a B-field gradient value of* $B_1 = 50mG$*. We have assumed a homogeneous distribution of population of Zeeman levels in the cloud and a Gaussian atomic distribution. (right): Lifetime of the collective excitation for the most magnetic-sensitive Zeeman sublevel* $m_F = 3$ *as a function of the B-field gradient.*

Residual magnetic field

During the memory experiment, the current in the coils of the magneto-optical trap are switched off. However, there is still a residual magnetic field at the atoms generally due to Eddy-currents in metallic parts around the chamber induced by the fast shut-off of the current in the coils. Unwanted magnetic field can also come from the Earth or surrounding environment (lab hardware, neighbouring metro station). This type of decoherence was initially studied at Caltech [Felinto et al. 2005] to explain the very short memory times observed in DLCZ experiments at that time.

We consider a non-zero magnetic field of projection B along the quantization axis. This induces the splitting of the hyperfine level $|F\rangle$ into a set of $2F+1$ states called Zeeman sublevels and denoted by the quantum number $m_F \in [-F,F]$. The energy difference between each state compared to the magnetic-insensitive state $m_F = 0$ is given by $\Delta E = \mu_B g_F \Delta m_F B$ where μ_B is the Bohr's magneton and g_F is the Landé factor of the hyperfine state F. If we suppose that the magnetic field is not constant in space, we can write the phase term for the i^{th} atom (in state m_F) as :

$$\varphi_{i,m_F}(t,\mathbf{r}_i) = m_F \mu_B g_F B(\mathbf{r}_i) t \tag{2.40}$$

The efficiency then becomes an integral over space, summed for each Zeeman sub-level:

$$\eta_m(t) = \left| \sum_{m_F=-F}^{+F} \int n_{m_F}(z) \exp\left[i\varphi_{m_F}(t,z)\right] dz \right|^2 \tag{2.41}$$

where we have considered that the magnetic field only varies in the longitudinal direction. We write $n_{m_F}(z)$ as the distribution of m_F sub-levels population in space and we consider that the m_F sublevels are equally populated by the atoms. We suppose the atomic spatial distribution to be Gaussian shaped, $n_{m_F}(z) = 2e^{-4z^2/L^2}/(L\sqrt{\pi})$ with L the length of the cloud. In pratice, we use cancelation coils to minimize the magnetic field impact on the retrieval efficiency, allowing the cancelation of most of the field. We thus consider variations of $B(z)$ up to first order such that $B(z) = B_1 z$. This consideration leads us to:

$$\eta_r(t) = \left| \sum_{m_F=-F}^{+F} \int e^{-\frac{4z^2}{L^2}} e^{i\alpha_{m_F} z t} \right|^2 \tag{2.42}$$

where we have noted $\alpha_{m_F} = \mu_B g_F B_1 m_F$. For a single m_F level, this equation is the Fourier transform of a Gaussian leading to a Gaussian decay of the efficiency:

$$\eta_r(t) \propto e^{-L^2 \alpha_{m_F}^2 t^2/8} \tag{2.43}$$

with a memory time given by

$$\tau = \frac{2\sqrt{2}}{L|\alpha_{m_F}|}. \tag{2.44}$$

Figure 2.6 displays the decay of the efficiency as a function of time for $B_1 = 50$mG/cm which is the situation in our lab. We observe that the caracteristic time $\simeq 15\mu$s is the one that limits our experiment. These calculations could be made more accurate by considering higher orders of the magnetic field, especially the second order. We also assumed a Gaussian atomic distribution which may not be exact in our case. However, these results give a good order of magnitude and describe well the involved physics.

Differential light shift

Although not relevant in our system, decoherence from light shift arises in dipole trap atomic memories or optical lattices systems where strong lasers are shined onto the atoms during memory implementation. This induces a spatially varying shift in frequency of the states which depends on the intensity of the laser. If the laser intensity is not homogeneous along the cloud, dephasing will happen after some time. Moreover, the differential light shift depends on the m_F state considered which means that decoherence will be more important if several Zeeman sub-levels are populated.

Transit time

While this is not a dephasing effect, the transit time due to finite temperature in our cloud can potentially degrade the performance of the read out. The thermal motion of atoms in a non zero temperature vapor is distributed by the Maxwell Boltzmann distribution $f(v) \propto exp\left(\frac{-mv^2}{k_B T}\right)$. Due to this motion, the atoms can leave the interaction area during the storage process. For a temperature of 25μK, the average velocity is given by $\langle v \rangle = \sqrt{8k_B T/(\pi m)} = 63$mm/s. Considering a beam diameter of 250μm, the average transit time for an atom is given by $\tau \simeq 4$ms. This value is not limiting in our experiment since we usually perform storage in a time-scale of the order of a few tens of μs.

4.3 Collective enhancement

It is important to note that the memory process is made possible by the collective effects that arise thanks to the use of a large collection of atoms. If we were to implement this kind of quantum memory with a single atom in free space, there is no reason that the read-out signal would be emitted in the same mode as the input signal. However, using a large number of atoms makes it possible thanks to the effect known as *collective enhancement*.

This effect can be understood from the point of view of momentum conservation. As we have seen in Section 4.2, the ith atom absorbs a signal photon $\mathbf{k}_s$ and emits a control photon in the control mode $\mathbf{k}_c$ during the spin-flip process. The corresponding collective excitation therefore comes in with the phase factor $e^{i(\mathbf{k}_s-\mathbf{k}_c)\cdot\mathbf{r}_i}$. In the read-out operation, the atoms absorb a control photon $\mathbf{k}'_c$ and emit a signal photon $\mathbf{k}'_s$. The resulting state of the ensemble can be written as :

$$|\Psi\rangle = \frac{1}{\sqrt{\mathcal{N}}}\sum_{i=1}^{\mathcal{N}} e^{i(\mathbf{k}_s-\mathbf{k}_c+\mathbf{k}'_c-\mathbf{k}'_s)\cdot\mathbf{r}_i}\,|g_1,...,g_i,...,g_{\mathcal{N}}\rangle \tag{2.45}$$

The probability of the read-out process can be evaluated by the quantity $|\langle g|\Psi\rangle|^2$ which is significant only in the regime where $\mathbf{k}'_s = \mathbf{k}_s - \mathbf{k}_c + \mathbf{k}'_c$. In our experiment we use a single control beam such that $\mathbf{k}_c = \mathbf{k}'_c$. This leads to $\mathbf{k}'_s = \mathbf{k}_s$ causing the signal photon to be emitted in the same mode as the initial one.

5 Critical conditions for optimal storage

After defining and explaining the storage and retrieval process in an atomic medium, we now turn on to its optimization in order to maximize the efficiency. Several conditions are required in order to optimize the efficiency of the dynamical EIT memory process. First, the EIT window must be made as transparent as possible using a good set of polarizations for signal and control field. The temporal and frequency shape of the signal pulse must then be optimized to fit the EIT window. The optical depth of the medium is also a key parameter that should be as high as possible although this might reduce the efficiency in certain cases, especially in transitions where hyperfine excited levels are close in energy.

5.1 Polarization

In order to understand the importance of polarization in EIT, we must consider the selection rules between the Zeeman sub-levels. We consider σ^+, σ^- and π polarizations of a signal field compared to its propagation axis z. If we decompose the $m_{F,z}$ sublevel on the z axis, $\sigma^\pm$ will only couple states with a difference of quantum number $\Delta m_{F,z} = \pm 1$ respectively. Similarly, π transitions only couple to the same $m_{F,z}$. This implies that, for a specific set of polarizations between the control and the signal, some excited states might not be coupled to another ground state as it is represented on Fig. 2.7. This induces absorption in the transparency that is dependent on the population distribution of the initial m_F sublevels. The correct set of polarization depends on the hyperfine levels chosen as ground and excited states. For the D_1 line of cesium, taking $|g\rangle = \left|6S_{1/2},F=3\right\rangle$, $|s\rangle = \left|6S_{1/2},F=4\right\rangle$ and $|e\rangle = \left|6P_{1/2},F=4\right\rangle$, the ideal situation is obtained when both probe and control have the

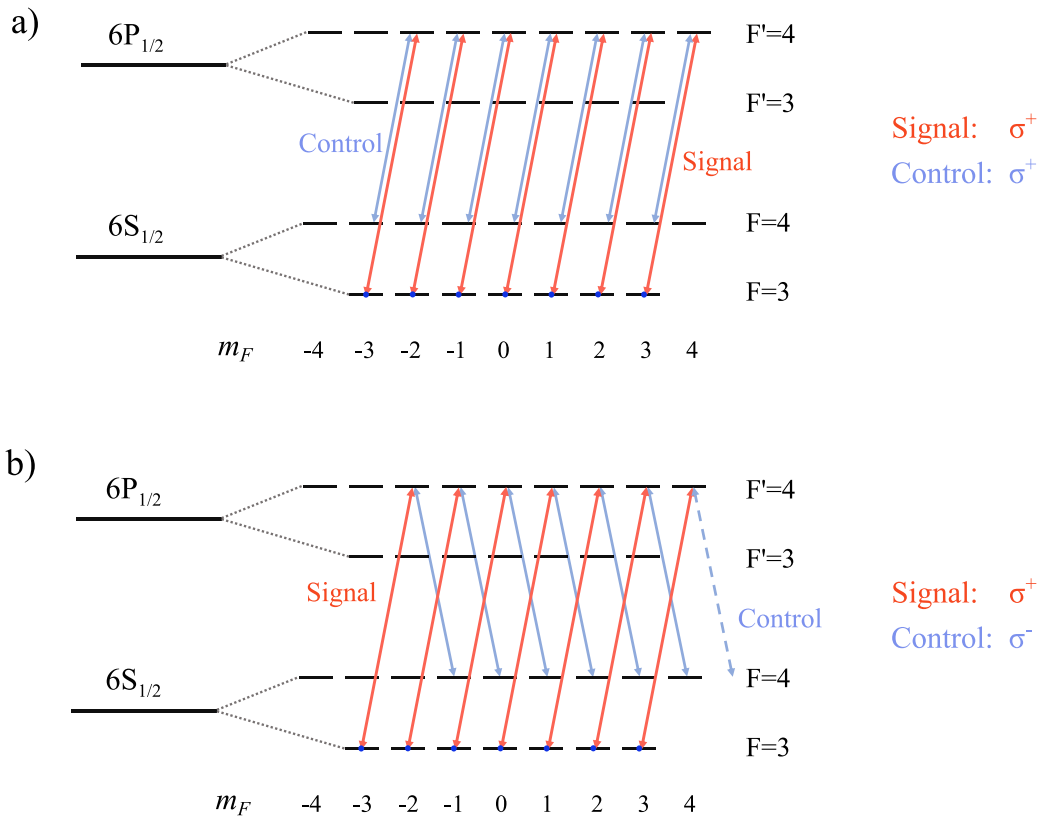

Fig. 2.7 *Example of two configurations for EIT on the D_1 line of cesium where all the atoms are initially in the ground state $|F = 3\rangle$ distributed among all the zeeman sublevels. a) Both signal and control have the same circular polarization. All excited levels $|F' = 4,m_j\rangle$ are coupled to another ground state. Full transparency can be achieved. b) Signal and control have opposite circular polarization. Here, one transition is not coupled to another sublevel leading to partial absorption in the EIT transparency window.*

same polarization. In that case, a fully transparent EIT window is theoretically possible. In practice, this is impossible to realize if the signal and control propagate with a large angle because $\sigma^{\pm}$ and π represent projections of polarization on the quantization axis z. Therefore, keeping a low angle is also a requirement to optimize the polarization conditions.

5.2 Signal pulse shape and optical depth

One of the downsides of EIT storage is the bandwith which is limited compared to other platforms. The first condition for optimal storage in EIT is that the signal spectrum must be narrower than the transparency window. Around resonance, $\Delta \simeq 0$ and we can expand in Eq. 2.19 the susceptibility $\chi(\Delta)$ in a power series to find that the EIT transparency window scales like a Gaussian $T(\Delta \simeq 0) = exp\left(-\omega^2/2\sigma_{EIT}^2\right)$ with width

$$\sigma_{EIT} = \sqrt{\frac{c\Omega_c^4}{2\Gamma L g^2 \mathcal{N}}} = 2\frac{\Omega_c^2}{\Gamma\sqrt{\mathrm{OD}}} \tag{2.46}$$

where L is the length of the atomic cloud. As expected, the EIT window becomes wider for larger intensity of the control beam. Besides, we observe that the on-resonance optical depth of the signal appears in the denominator since the OD can also be expressed as [Duan et al. 2001]:

$$\mathrm{OD} = 4\frac{g^2\mathcal{N}L}{c\Gamma}. \tag{2.47}$$

If we consider a signal pulse of caracteristic time length σ_t and caracteristic bandwidth $1/\sigma_t$ then the first condition is expressed as:

$$\frac{1}{\sigma_t} \gg \sigma_{EIT} \tag{2.48}$$

On the other hand, a critical requirement to prevent leakage of the memory before storage is that the spatial length of the compressed pulse fits as a whole inside the atomic cloud. In other terms, the delay induced by slow light propagation in the medium must be larger than the duration of the pulse σ_t. The group delay $\mathcal{T}$ can also be expressed as a function of OD:

$$\mathcal{T} = \frac{L}{v_g} - \frac{L}{c} = \frac{\Gamma}{4\Omega_c^2}\mathrm{OD} \gg \sigma_t \tag{2.49}$$

It is important to note that the two conditions are antagonistic. Increasing the intensity of the control field will make the EIT window larger but will reduce the delay. Experimentally, a trade off must be found in order to satisfy both conditions in an acceptable way. If we combine these two conditions we find the requirement that

$$\mathrm{OD} \gg 1 \tag{2.50}$$

which shows the importance of optical depth in dynamic-EIT memory schemes.

5.3 D1 and D2 line comparison

The choice of the excited state in EIT memories is crucial in the quest for highly efficient memories. The level structure around the excited state plays an important role since off-resonant absorption might take place, and cannot be prevented with any choice of polarization. Since we work in a regime of high optical depth, these effects can become significant,

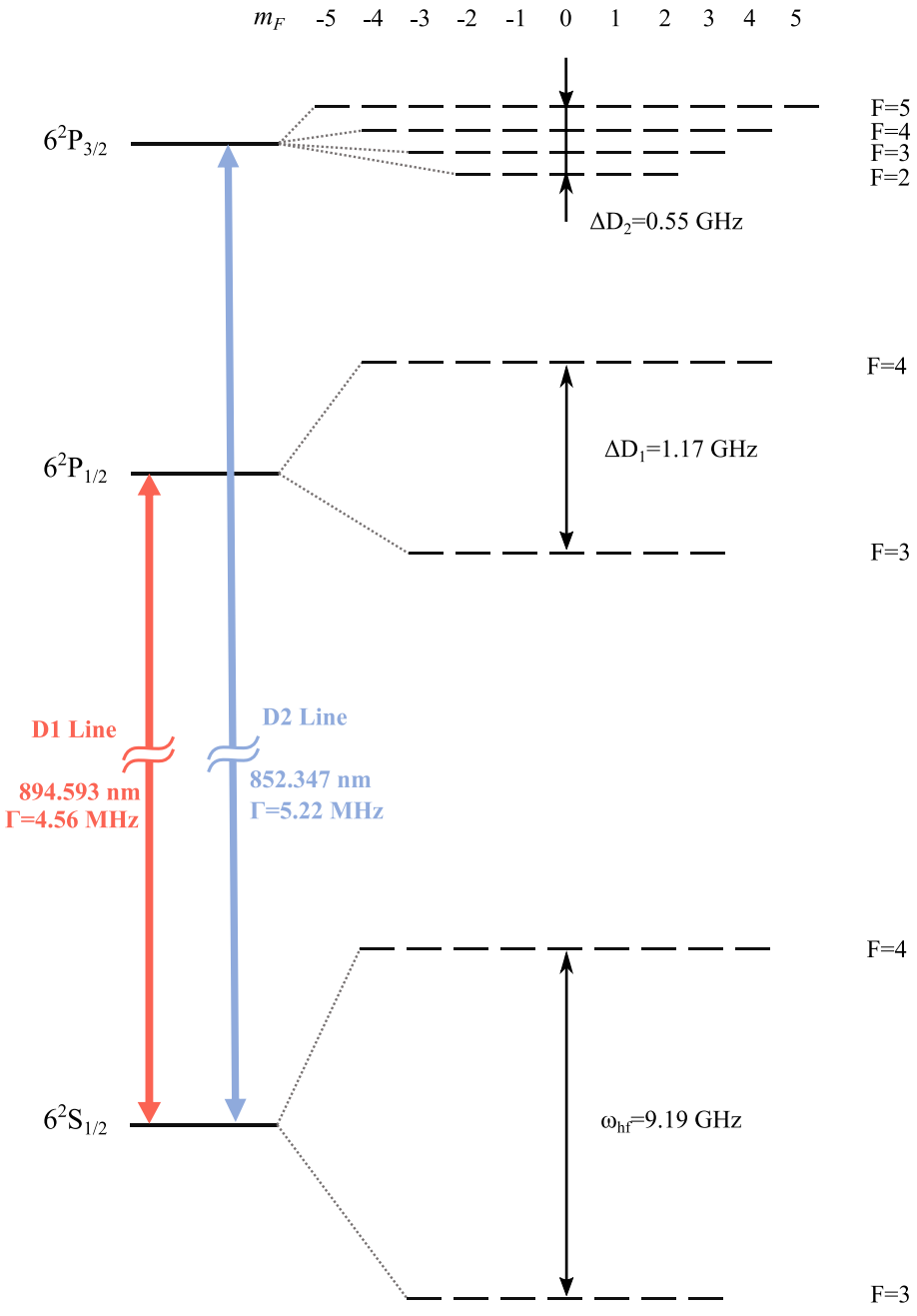

Fig. 2.8 *Scheme of ^{55}Cs energy levels of D_1 and D_2 line. Both transitions are used in our experiments.*

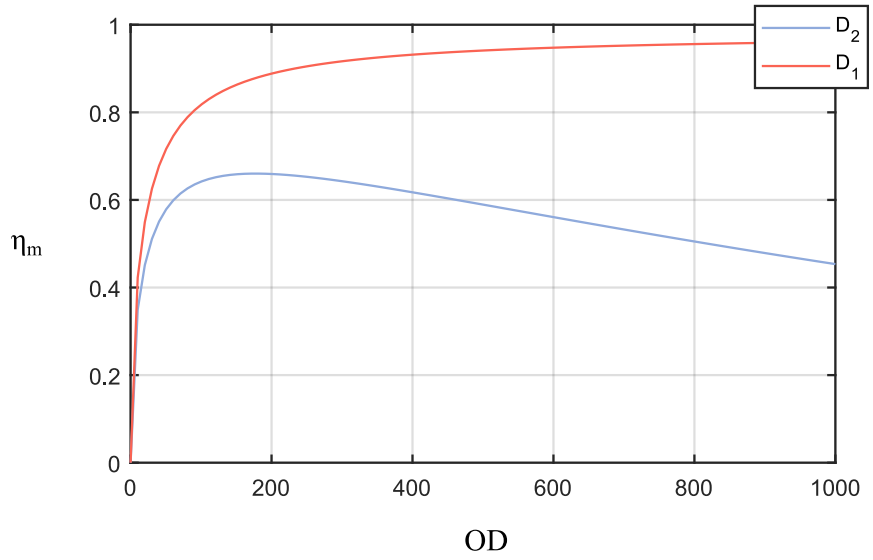

Fig. 2.9 *Evolution of the storage-and-retrieval efficiency of the EIT memory as a function of optical depth as it is calculated by a comprehensive model taking into account all off-resonant interactions with neighbouring excited states. We observe that the effective decoherence induced by these couplings leads to a limited efficiency if the memory is performed on the D_2 line. However, these effects are negligible on the D_1 line since the other excited state is far away in energy. Based on this computation, we decided to change our experiment at LKB in order to develop the ability to perform memories on the D_1 line.*

leading to a decrease of the total achievable efficiency. A full model involving all off-resonant excitations with the Zeeman sub-levels of neighbouring states has been developed in our group at LKB [Vernaz Gris, Huang, et al. 2018] to quantify this incoherent absorption and its effects on the storage-and-retrieval efficiency of the process. This model has also been used to fit the data obtained in the single-photon experiment presented in Chapter 4. Our group has a long history in the theoretical study of EIT in complex structure [Mishina et al. 2011; Sheremet et al. 2010] but this model is the most complete to date and provides a comprehensive overview of the involved physics. The model starts by considering all possible dipole transitions associated with all possible excited levels from $|g\rangle$ and $|s\rangle$, including all Zeeman sub-levels. This more complex dipole interaction gives rise to a set of several coupled Bloch equations that can be resolved by computation taking the Fourier transform of the atomic coherences. From the solutions, we can define the linear response of the medium characterized by its first order susceptibility $\chi(\omega,z)$ and then derive all useful quantities from it. We compare the results of this model for quantum memory on the D_2 and D_1 line of cesium. We start by considering an EIT memory relying on the levels $|g\rangle = \left|6S_{1/2},F=3\right\rangle$, $|s\rangle = \left|6S_{1/2},F=4\right\rangle$ and $|e\rangle = \left|6P_{3/2},F=4\right\rangle$ on the D_2 line. The model shows that the coupling to the neighboring excited states $F'=3$ and $F'=5$ induces an effective Stark shift on the excited state $|e\rangle$ and increases the ground state radiative decay relative to the ideal

Λ-type three-level system. The effective detuning of the probe that includes this Stark shift can be expressed as:

$$\Delta_{D_2}^{(eff)} = \Delta + \sum_{m=-3}^{3} \sum_{F' \in \{3,5\}} \frac{|\Omega_{c,F',m}|^2/4}{\omega_{ee,F',m+1}} \tag{2.51}$$

and the effective decoherence rate of the ground state coherence writes:

$$\gamma_{gs,D_2}^{(eff)} = \gamma_{gs} + \sum_{m=-3}^{3} \sum_{F' \in \{3,5\}} \frac{|\Omega_{c,F',m}|^2}{\omega_{ee,F',m+1}} \frac{\Gamma}{8}. \tag{2.52}$$

Here, $\hbar\omega_{ee,F',m}$ is the energy difference between the hyperfine level $|e_{F',m}\rangle$ and $|e_{F'=4,m}\rangle$, and $\omega_{ee,F',m}$ is the detuning of the control for the dipole transition between $|g_m\rangle$ and $|e_{F',m+1}\rangle$ (considering a σ^+ polarisation of the control field).

On the D_1 line, we choose our Λ-type three-level system with $|g\rangle = \left|6S_{1/2},F=3\right\rangle$, $|e\rangle = \left|6P_{1/2},F'=4\right\rangle$ and $|s\rangle = \left|6S_{1/2},F=4\right\rangle$. Again, these choices of states are made in order to optimize the achievable optical depth on the signal transition and optimize the transparency of the EIT with the polarization conditions. In this case, there is only one hyperfine level $\left|6P_{1/2},F'=3\right\rangle$ (seven Zeeman excited states) that contributes to off-resonant excitations and leads to a Stark shift of the state $|e\rangle$. The effective detuning and effective decoherence rate are expressed as

$$\Delta_{D_1}^{(eff)} = \Delta + \sum_{m=-3}^{3} \frac{|\Omega_{c,3,m}|^2/4}{\omega_{ee,3,m+1}} \tag{2.53}$$

and

$$\gamma_{gs,D_1}^{(eff)} = \gamma_{gs} + \sum_{m=-3}^{3} \frac{|\Omega_{c,3,m}|^2}{\omega_{ee,3,m+1}} \frac{\Gamma}{8}. \tag{2.54}$$

At this point, we emphasize here the two main differences between the D_1 and D_2 line leading to this effective decoherence to be much less significant in the D_1 case. As we see on Fig. 2.8, we note that there is contribution from only one excited level, which makes less terms in the sum of the above expressions. More importantly, we observe that the energy difference $\hbar\omega_{ee,F',m}$ between the state $|e\rangle$ and the off-resonant excited states is more than 4 times larger in the D_1 line. Since $\omega_{ee,F',m}$ appears in the denominator of each contribution, it leads to the reduction of the strength of each contribution in the D_1 line case.

On the other hand, we observe that each term increases with the control field Rabi frequency. Since the group delay $\mathcal{T}$ is proportional to $\mathrm{OD}/|\Omega_c|^2$ and needs to be kept constant for efficiency optimization, it makes this decoherence more significant with large OD since the Rabi frequency needs to be increased. As a result, there is now a trade-off to find in order to optimize the efficiency, since increasing the OD provides both favorable and unfavorable conditions. To quantify this effect, we can calculate the efficiency of the memory process via the susceptibility $\chi(\omega,z)$ derived by the model. The efficiency is defined as

$$\eta_m = \frac{\int dt |E(z=L,t)|^2}{\int dt |E(z=0,t)|^2} \tag{2.55}$$

where $E(z = L,t)$ is given by the solution of the propagation equation:

$$E(z = L,t) = \int_{-\infty}^{+\infty} \frac{d\omega}{2\pi} e^{-i\omega t} \tilde{E}(z = 0,\omega) \exp\left[-2\pi i \frac{\omega}{c} \int_0^L \chi(\omega,z) dz\right]. \tag{2.56}$$

We suppose that our input probe pulse is a Gaussian of standard deviation σ_t. We plot in Fig. 2.9 the efficiency of the memory as a function of OD as it is expressed in Eq. 2.55. For the calculations, we fix $\mathcal{T}/\sigma_t = 2$ and we keep the group delay constant $\mathcal{T} = 200$ ns. Since the effective decoherence $\gamma_{gs}^{(eff)}$ is prominent on the D_2 line, we see that the trade off happens quite quickly around OD=200 yielding a maximal achievable efficiency of $\simeq 65\%$. On the bright side, these effects are negligible on the D_1 line in this range of OD, therefore making it an ideal candidate for a quantum memory with a value of storage-and-retrieval efficiency near unity.

6 Conclusion

In this chapter, we started by setting up the basic requirements of light-matter interactions in order to understand the physics at play in a Λ-type three-level system. We introduced the concept of EIT in a collection of $\mathcal{N}$ atoms and showed that the group velocity of the signal light can be significantly reduced in the medium. Then, we discussed the collective excitation and its main decoherence mechanisms. In our experiment, the main decoherence arise from the residual magnetic field around the atoms during memory implementation, leading to storage time of the order of a few tens of microseconds. We then described the storage and retrieval process as the propagation of a dark-state polariton made of both light and spin components. Finally, we discussed the essential requirements to perform efficient storage and we demonstrated that storing light pulses via the D_1-line excited state gives realistic access to an efficiency above 90%. This is the motivation for this thesis which needed to modify the experimental setup accordingly and reaching high values of optical depth. In the following of the manuscript, we will describe how these challenges were overcome and led to a highly efficient memory implementation.

Chapter 3

Tools for atomic ensemble preparation

Our system relies on a magneto-optical trap (MOT) [Raab et al. 1987]. The MOT is indeed a robust trap that does not depend on precise alignment of laser beams or very high degree of polarization control. Its magnetic field gradients can be achieved with air-cooled coils and kinetic temperature of the order of a few tenth of microkelvin can be achievable thanks to further polarization-gradient cooling of the cloud. It is also possible to shape the geometry of the MOT like a cigar to obtain high absorption of a probe and to precisely control the magnetic environment for experimental purposes. This is what we show in this Chapter. We start by describing the basic interactions involved in the production of a MOT and then focuse on the techniques that we use in order to characterize the properties of atomic ensembles. We also discuss the various processes to optimize the optical depth of our MOT and we end by presenting our experimental apparatus at LKB.

1 Cooling and trapping atomic ensembles

Cooling and trapping atomic ensembles rely on the ability to exert a force on the atoms thanks to the use of laser light fields. Different techniques of atomic trapping exist depending on the nature of the atom. Neutral atoms, for example, can be trapped by an inhomogeneous magnetic field thanks to the interaction between their magnetic moment $\boldsymbol{\mu}$ and the field $\mathbf{B}$ that produces a force given by $\mathbf{F} = \boldsymbol{\nabla}(\boldsymbol{\mu} \cdot \mathbf{B})$. This type of trap can be done very simply by taking two identical coils carrying opposite currents. The first observation of magnetically trapped neutral atoms has been realized at NIST in 1985 for times exceeding one second [Migdall et al. 1985]. On the other hand, neutral atoms can also be trapped optically due to the interaction between eletric fields and dipole moments and the exchange of kinetic energy between photon and atoms. These interactions result in two dinstinct forces: the dipolar force and the radiation pressure respectively. The dipolar force can be used to realize optical tweezers, lattices [Salomon et al. 1987] and dipole traps, whereas radiation pressure is a key feature of the MOT. In this section, we describe the principles behind the optical and magnetic components of a MOT, and how the trapping and cooling arise from the combination of these effects.

1.1 Radiation pressure

Radiation pressure arises from the momentum kick during the transfer of an atom to an excited state $|e\rangle$ by the absorption of a photon. The incoming photon carries a momentum $\hbar\mathbf{k}$ that is fully transferred to the atom. In the presence of a light that couples the ground state and an excited state and considering the stationnary case, the rate at which these absorption occur is simply Γ times the average population in the excited state. This population is expressed as a function of the resonant saturation parameter $s_0 = I/I_{sat}$, with I_{sat} the saturation intensity of the atoms, in the following form:

$$\rho_{ee} = \frac{1}{2}\frac{s_0}{1+s_0}. \tag{3.1}$$

The atom will also emit a photon when it decays back to the ground state at rate Γ, however this spontaneous emission is isotropic and therefore does not contribute to the net force. Therefore, the average radiation pressure force writes:

$$\mathbf{F}_{rp} = \frac{\Gamma}{2}\frac{s_0}{1+s_0}\hbar\mathbf{k}. \tag{3.2}$$

In pratice, the "trapping" beams of the MOT are detuned by a few units of Γ. Out of resonance, the saturation parameter can be expressed as a function of detuning Δ.

$$s(\Delta) = \frac{I}{I_{sat}}\frac{1}{1+4\Delta^2/\Gamma^2}. \tag{3.3}$$

1.2 Doppler cooling

Thanks to the Doppler effect, detuned light can still be seen resonant for a specific class of atomic velocities $\mathbf{v}$. From Eq. 3.3, by replacing $\Delta(\mathbf{v}) = \Delta_0 - \mathbf{k}\cdot\mathbf{v}$ and using the fact that $I/I_{sat} = 2\Omega^2/\Gamma^2$, we can express the velocity-dependent radiation pressure force as:

$$\mathbf{F}_{rp}(\mathbf{v}) = \frac{\Gamma}{2}\hbar\mathbf{k}\frac{\Omega^2/2}{\Omega^2/2+\Gamma^2/4+\Delta(\mathbf{v})}. \tag{3.4}$$

In the case when the cooling light and the velocity are on the z-axis, $\mathbf{v} = v\mathbf{u}_z$ and $\mathbf{k} = k\mathbf{u}_z$, and supposing that velocities are small enough, we can expand the previous expression to the first order in $(\mathbf{k}\cdot\mathbf{v})$ to get the following expression :

$$\mathbf{F}_{rp}(v) = \mathbf{F}_{rp}(0) + \alpha v\mathbf{u}_z \tag{3.5}$$

where

$$\alpha = s_0\hbar k^2\frac{\Delta_0\Gamma}{\Delta_0^2+\Gamma^2/4} \tag{3.6}$$

which has the sign of the detuning Δ_0. Thus, a negative detuning will make the force to act like a friction force. In practice, trapping beams are sent from all six directions of space, effectively reducing the atoms kinetic energy in the region of space where the beams overlap. Note that with real atoms, the excited state can decay to another ground state which makes the atoms invisible to the trapping beams. To counter this effect, we use an additional beam to restore these atoms to the initial ground state, generally called "repumper".

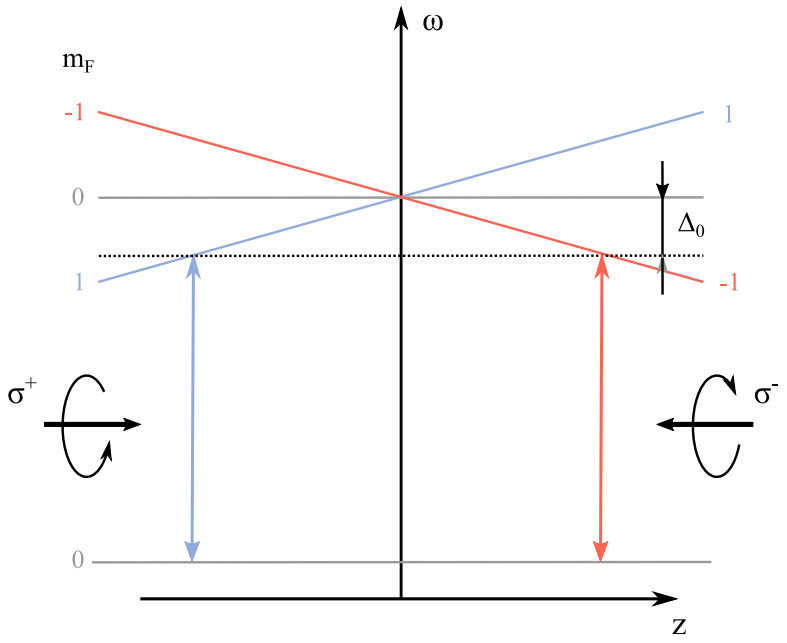

Fig. 3.1 *Simple representation of a MOT in one dimension. The horizontal dashed line represent the frequency of the trapping beams which counterpropagate in the z-direction, with opposite polarization. Because the magnetic field shifts the Zeeman sub-levels, atoms at z>0 are closer to resonance with the σ^+ beam leading to a push toward the center of the trap. The same effect takes place for the σ^- beam at positions z<0.*

1.3 Magneto-optical trapping

Magneto-optical trapping combines the use of these trapping beams with a gradient of magnetic field. Still considering the one dimensional case for simplicity, we apply a first order magnetic gradient along the axis $\mathbf{B} = bz\mathbf{u}_z$ that has the effect of lifting the degeneracy of Zeeman sub-levels by the following amount :

$$\Delta_{m_F}(z) = \Delta_0 - \frac{\mu_B g_F m_F b z}{\hbar}. \tag{3.7}$$

This detuning, and thus the radiation pressure force, is not only position-dependent but also depends on the considered m_F state. Now, we send two trapping beams of negative detuning that are circularely polarized $\sigma_\pm$ relative to the axis of the m_F decomposition, in opposite directions $\pm z$. For simplicity, we consider a ground state of $F = 0$ and an excited state of $F = 1$. Consider an atom at distance $z > 0$, the transition with $m_F = -1$ is closer to resonance with the laser frequency. Due to the selection rules defined in Section 5.1 of dipolar transitions, the σ_- light propagating in the $-z$ range of positions will be absorbed and this gives a scattering force that pushes the atom back toward the trap center. The chosen Δ_0 detuning and the strength of the magnetic field gradient will determine the capture range of the atomic cloud which is in pratice of the order of the centimeter. We can inject this

detuning $\Delta_{m_F}(z)$ in the expression of the radiation pressure force Eq. 3.4 and expand the expression in the same fashion as in the last section to get the following expression when $\Delta_0 < 0$:

$$\mathbf{F}_{rp}(v,z) = \left[-|\alpha|v - \frac{|\alpha|\beta}{k}z\right]\mathbf{u}_z \tag{3.8}$$

where $\beta = g\mu_B b/\hbar$. We see that the imbalance in the radiation pressure force leads to an additional spring-type force that has the effect of pushing the atoms toward the region where $\mathbf{B} = 0$. This expression fully grasps the dynamics at play during the loading of a MOT where both Doppler cooling and Zeeman trapping are performed. Note that for cesium atoms we choose $|g\rangle = \left|6S_{1/2},F=4\right\rangle$ and $|e\rangle = \left|6P_{3/2},F=5\right\rangle$, which is a more complicated system than the one presented in Fig. 3.1 since the ground state now has to be decomposed into a set of Zeeman sub-levels. In these types of atoms, the scheme still works but involves optical pumping where atoms that scatter mainly from the $\sigma^{\pm}$ trapping beams will be pumped towards the $m_{|g\rangle} = \pm 4$ state thus forming a closed system with the $m_{|e\rangle} = \pm 5$ state.

1.4 Polarization gradient cooling

After loading the MOT, temperature can still be of the order of hundreds of μK because of the Doppler limit. Further cooling can be performed thanks to a particularly important mechanism by which atoms dissipate energy as they move through a standing wave. This is known as polarization gradient cooling (or Sysiphus cooling) and was theoretically explained by Jean Dalibard and Claude Cohen-Tannoudji in 1989 [Dalibard and Cohen-Tannoudji 1989]. The idea lies in the fact that the counter-propagation of two opposite circular-polarization beams creates a standing wave of polarization. A cesium atom in the standing wave will undergo a light shift of the two ground state $|m_J = 1/2\rangle$ and $|m_J = -1/2\rangle$ where its magnitude depends on the polarization of the standing wave. Specifically, consider a position where the light has a σ^+ polarization and a negative detuning Δ; here the $|m_J = +1/2\rangle$ state is shifted to a lower energy than $|m_J = -1/2\rangle$. Similarly, for a σ^- polarization it is the state with $m_J = 1/2$ that has the highest energy. This change in light shift happens over a distance of $\lambda/4$ and an atom moving in this potential will see its kinetic energy increase and decrease if nothing else happens. However, if we consider absorption and spontaneous emission, the absorption of an atom at the top of a hill followed by a decay to the bottom of the valley is a lot more likely than the opposite scenario. Therefore, the kinetic energy lost by the atom climbing the hill is dissipated trough the emitted photon and the atoms end-up in having less velocity. This process is repeated until all the atoms do not have enough energy to climb another hill, resulting in a cooled down ensemble of atoms. The temperature limit of this process is reached when the loss in energy in going from the top of a hill to the valley is balanced by the recoil acquired by spontaneous emission. The lowest achievable temperature are therefore of the order of the recoil energy divided by the Boltzmann constant: $T_r = E_r/k_B$. As a function of the frequency ω_{ge} of the transition it writes:

$$k_B T_r = \frac{\hbar\omega_{ge}^2}{c^2 M} \tag{3.9}$$

which is as low as 198nK for cesium. In pratice, we do not reach this temperature. This is mainly due to the complicated hyperfine structure of cesium which has not been considered in the previous description. A more detailed analysis can be found in [Ungar et al. 1989].

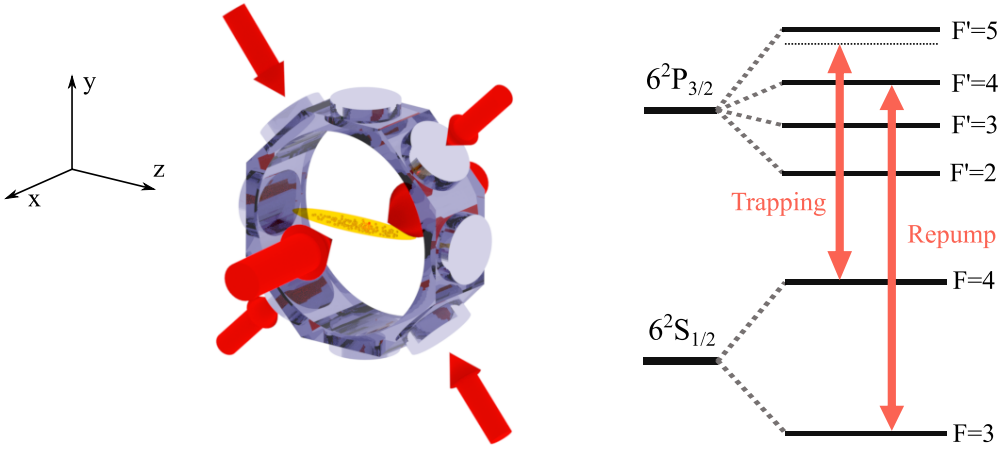

Fig. 3.2 *Representation of our MOT in its glass vacuum chamber. The relative size of the atomic cloud has been increased for clarity. Trapping beams are sent from all three directions of space and retroreflected. A repumper beam is also sent from the same direction in order to keep the atoms in the cooling cycle. The trapping beams are red detuned by* $\Delta_0 = -17MHz$ *from the* $F = 4 \rightarrow F' = 5$ *transition during the loading phase and the repumper is resonant with the* $F = 3 \rightarrow F' = 4$ *transition.*

1.5 Elongated MOT at LKB

We will now describe the basics of the geometry design of our MOT at LKB. A more detailled description of the optimization of timings and sequences is given in Section 3. As explained in Chapter 2, it is of major interest to optimize the optical depth of our cloud. One way to increase the OD is to increase the proportion of atoms that interacts with the laser. This can be done by building an elongated ensemble, meaning that the atomic cloud is shaped like a cigar with its axis corresponding to the optical propagation axis. This idea was first demonstrated in [Lin et al. 2008] and is now used in a few experiments involving high-OD MOT.

The main idea is to replace the usual circular anti-Helmholtz coils by a set of two pairs of rectangular coils in the xz and yz plane. This configuration generates a magnetic field which has a weak longitudinal gradient allowing the atoms to spread along the z direction. Sometimes, a pair of coils in the third direction can be added (called cap-coils) to implement a small gradient in order to confine the atoms in the overlapping region of the trapping beams. The measurements presented in this thesis were performed with a set of coils that does not include cap-coils since it did not improve the overall OD after testing it out. Note that over the last year, the coils degraded and a new pair was built.

The trapping beams are detuned by $\Delta_0 = -17$ MHz from the $F = 4 \rightarrow F' = 5$ transition and sent from all six directions of space. The total power is around 300 mW where 180 mW is sent in the front beams. The balance between these powers can be adjusted with a set of

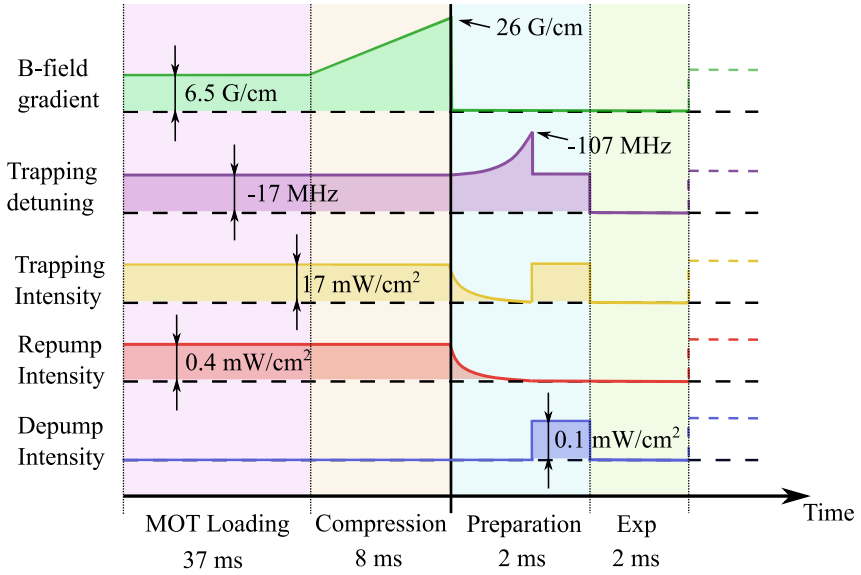

Fig. 3.3 *Typical timings for the preparation of our PG-cooled and compressed MOT.*

waveplates but it is usually best to keep the same power in both left and right beams for geometry purposes. The decay $F = 5 \rightarrow F' = 3$ is forbidden thanks to the selection rules. However, off resonant scattering of $F' = 4$ towards the $F = 3$ ground state is possible which makes atoms leave the cooling cycle. In order to counter this effect, we add a repumper beam (8 mW), resonant with the $F = 3 \rightarrow F' = 4$ transition in order to repopulate the other ground state and maintain the cooling. We send this beam through the same fiber couplers as the trapping beams. There are three fiber couplers that output the beams and each of them is followed by a collimator that shapes the beam as a Gaussian of diameter 50 mm. Each beam is retroreflected by a mirror placed after a $\lambda/4$ waveplate that rotates the polarization. Therefore, sending one trapping beam in a σ^+ polarization makes the retro-reflected polarization σ^- and fulfill the setup of 1.3. Moreover, the propagation of each trapping beam and its reflection with opposite circular polarization generates a standing wave with a position dependent polarization, as required for polarization gradient cooling. We perform this polarization gradient cooling after the extinction of the magnetic field where we also ramp down the detuning of the trapping beams and repump beams, having the effect of reducing their overall power. Before the extinction of the magnetic field, a fast increase of current in the rectangular coils compresses the cloud and increases its density. A typical time sequence is presented in Fig. 3.3. After PG-cooling, we send a strong pulse of trapping beams in order to prepare our cloud in the $F = 3$ ground state.

1.6 Temporal dark MOT preparation

It is possible to increase the density of a cloud of atoms by preparing a dark MOT (in contrast to what we call a bright MOT). The dark MOT was first proposed in 1993 [Ketterle et al.

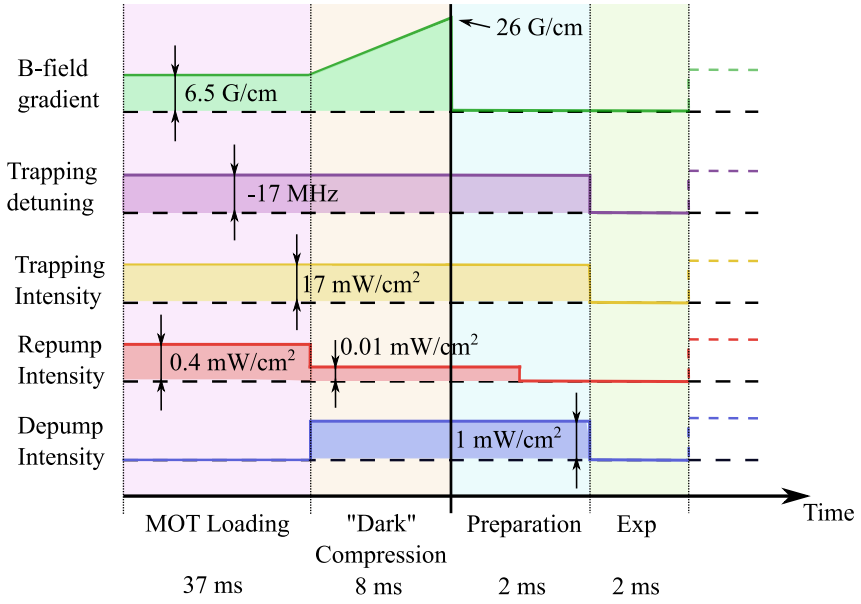

Fig. 3.4 *Typical timings for the preparation of our temporal dark MOT.*

1993] in a "dark spot" fashion. The idea was to cast a shadow in the center of the repumper beam allowing atoms in this region to optically pump to the state which is out of the cooling cycle, called dark state. In the volume outside of this region, trapping forces operate as usual. The idea lies in the fact that atoms in this dark region will not undergo recoil kicks from reabsorbing scattered photons, therefore reducing the rate of atomic light-induced collisions. Thus, the density increase in this volume since all surrounding atoms are pushed toward this zone. Dark-spot MOT for cesium atoms has been realized at Cambridge University in 1995 [Townsend et al. 1996] where an increase of density of up to an order of magnitude was shown, although it is shown to be more difficult to realize since it requires the use of another beam to pump the atoms to the dark-state (a depump beam). The temporal dark-MOT relies on the same principle of reducing light-induced collision but this time in the whole MOT. It is realized by reducing the repumper intensity up to a regime where the fraction p of atoms in the $F = 4$ state is much smaller than 1. This fraction $p = N_{F=4}/(N_{F=3} + N_{F=4}) < 1$ can be controlled by adjusting the repumper intensity, and a trade-off needs to be found between the loss of atoms from the cycle and the loss coming from the induced collisions. We followed the method proposed by [Hsiao et al. 2014] where the repump intensity is maintained high enough in the loading phase such that $p \simeq 1$ and then reduced during the compression phase. A depump beam is also added during this dark compression phase. The timing diagram of such a MOT is shown in Fig. 3.4 and a detailed optimization is described in Section 3. In the end, the OD appears to be much higher (around 500) but the temperature is above 300μK which is unfavorable for memory experiments.

This increase in temperature is however unexpected since a significant fraction of the atoms are confined in the dark state and therefore become invisible to the trapping beams. Indeed, this reduces significantly the reabsorption of scattered light which is supposed to prevent heating effects [Drewsen et al. 1994; Cooper et al. 1994]. The excess heating due to

multiple scattering is the result of a two-body event and should decrease as p^2 [Townsend et al. 1996]. However, there is a major difference when considering dark MOT with heavy alkali-metal atoms such as cesium rather than sodium. The larger hyperfine splitting makes the natural depumping rate into the dark state much lower and the use of a depumper beam to achieve low values of p is mandatory. Townsend and colleagues [Townsend et al. 1996] show that if the depumping rate is large enough to reduce the average time spent in the $F = 4$ ground state below the molasses characteristic damping time, the temperature increases. They also show that for a MOT that uses a low field gradient to load the trap and then performs a compression by gradually increasing this gradient, the optimization of density by varying the fraction p leads to a molasse temperature of 105 μK. This increase in temperature also seemed to be observed in [Hsiao et al. 2014], in which they managed to obtain an OD of up to 1000. Although they did not provide the real temperature value, they say that *"an increase of 0.5 ms free flight time causes a reduction in OD of ∼35%"*. Considering the model described later in section 2.2.2, such a reduction in OD could account for a temperature higher than 500 μK.

In the end, altough the temporal dark-MOT easily gives high values of OD, it seems that high values of temperature are unavoidable. We tried to pump back the atoms in the $F = 4$ state after extinction of the B-field to further perform PG-cooling but this process resulted in a great loss of OD.

2 Characterization of atomic ensembles

Several experimental tools are needed in order to fully characterize a cloud of cold atoms. In this section we mostly focus on the measurement of optical depth as well as temperature. A novel method of temperature measurement developed during this PhD related to the decrease of optical depth in time during the experimental time-window is presented. Finally, our method to estimate residual unwanted magnetic fields in our cloud during the experiment phase, and how we can optimize its magnitude in a static and dynamic way is presented.

2.1 OD measurement

As previously stated, the optical depth of our atomic cloud is a crucial parameter. The method to measure this value is described hereafter. If $I_{in} \ll I_{sat}$, the on-resonance optical depth is given by the formula derived in Chapter 2:

$$\mathrm{OD} = \left(1 + 4\frac{\delta^2}{\Gamma^2}\right) \ln\left(\frac{I_{in}(\delta)}{I_{out}(\delta)}\right). \tag{3.10}$$

One can see that only one detuned measurement would be enough to measure the OD. However, when the OD is large, lensing arising from the dispersion around resonance can deviate light differently for each frequencies leading to a deformation of the absorption profile. It is generally safer to measure the full absorption profile for different detunings and then fit the formula to find a corresponding optical depth. Our experimental setup is presented in Fig. 3.5. Since it is inconvenient to measure light at the input of the cloud and then switch to a measurement at the output of the cloud, we define $I_{in,out}(\omega) = I_2(\omega)/I_1(\omega)$ where the measurement for I_{in} is performed by removing the atoms along the path and I_{out} with the

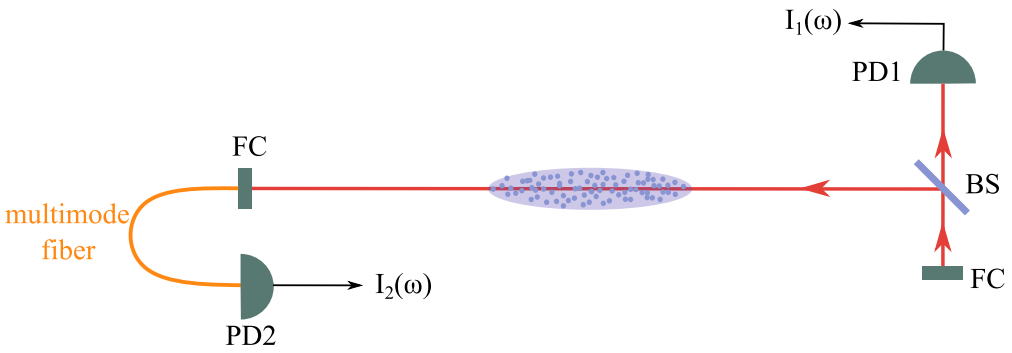

Fig. 3.5 *Setup for the measurement of optical depth. FC : fiber coupler, PD1(2): photodiode 1(2), BS: beamsplitter. The multimode fiber fiber is used in order to better capture the light after its propagation through the ensemble since, in the case of bad probe alignment, the light can be deflected due to a lensing effect.*

atomic cloud overlapping the probe path. This setup also has the advantage to bypass the variation of total power as a function of detuning. A typical absorption profile is presented in Fig. 3.6.

2.2 Temperature

The temperature of a gas is defined by the kinetic theory of Maxwell and Boltzmann to be a parameter that governs the distribution of velocities of all particles in that gas. This is a rather macroscopic quantity that might not always be relevant for cold atomic ensembles however it captures most of the related physics.

There are several ways of measuring the temperature - or velocity distribution - of an atomic cloud. The simplest one is to measure the doppler shift with absorption measurements. In the presence of Doppler broadening, the absorption profile is given by a Voigt function which results from the convolution of the Lorentzian natural absorption of linewidth Γ and the Gaussian broadening due to thermal velocity. However, this method is not suitable for cold atomic clouds since other sources of broadening might be at the same order of magnitude leading to false estimations (magnetic broadening). Another method consists in probing the absorption above the cloud and for different distances from the cloud. Performing these measurements at different times after the release of the trap allows to measure the velocity distribution since interacting atoms will reach this probing area depending on their velocities [Lett et al. 1988]. Another method, proposed by [J. León-Montiel and Torres 2012] consists in measuring the angular distribution of Stokes photons emitted by Raman scattering. For a $T = 0$ cloud, the distribution is supposed to be isotropic and for a hot atomic vapor, most of the scattering probability gathers in a cone oriented in the propagation direction. The aperture of this cone depends on the temperature.

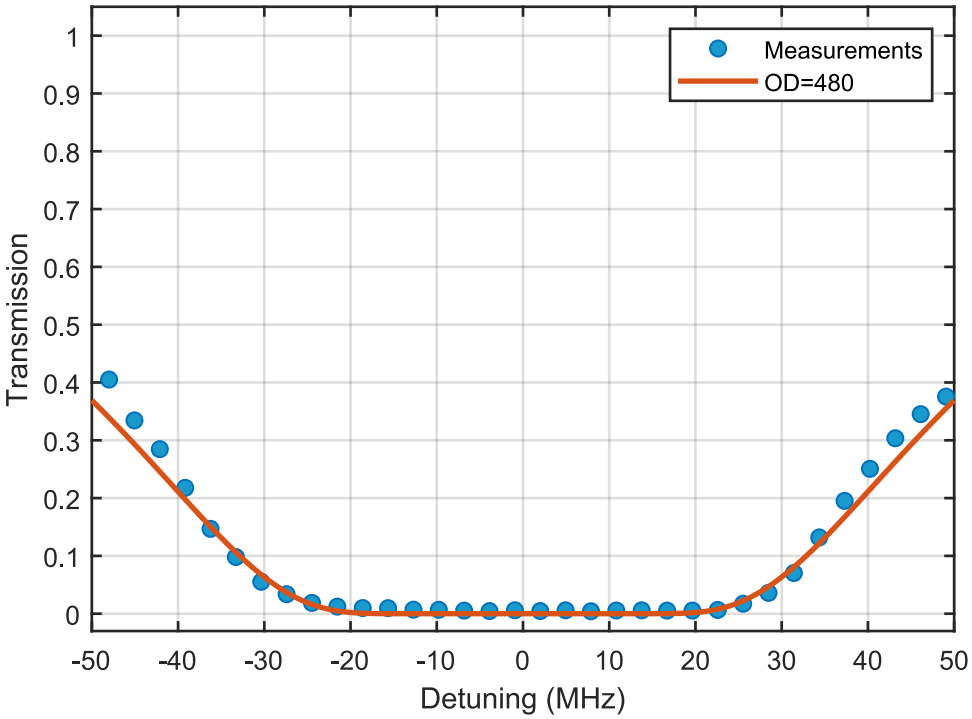

Fig. 3.6 *Typical absorption spectrum measured for a high-OD atomic cloud. Several absorption measurements are performed and fitted with Eq. 3.10. In this case, this measurement is performed on the D_1 line of cesium between the levels $|g\rangle = \left|6S_{1/2}, F = 3\right\rangle$ and $|e\rangle = \left|6P_{1/2}, F = 4\right\rangle$ where $\Gamma = 2\pi \cdot 4.56$ MHz. An optical depth around 480 is measured here.*

In this section we present the standard method to measure the temperature of our cloud called time-of-flight technique and show some results. After that, we present a model developped during this thesis. This model aims to describe the decay of optical depth as a function of time for different temperatures and compare it to experimental results.

2.2.1 Time of flight

The time-of-flight technique relies on the free-fall of the atomic cloud after its release from the trap, accompanied by what is called ballistic expansion. Indeed, when free from any external forces, the cloud expands due to the non-zero velocity distribution of atoms. The speed of this expansion is directly related to the distribution of velocities and therefore to the temperature. The width of the cloud after a time t is given by :

$$\sigma_t^2(t) = \sigma_0^2 + \frac{k_B T}{m} t^2. \tag{3.11}$$

Experimentally, we perform an absorption imaging measurement of the cloud on a CMOS camera at different times to retrieve this width. In order to retrieve the exact size of the width, it requires to know the distance between each pixel of the camera. To calibrate this distance, the free-fall of the center of mass which is only affected by gravity is monitored. We can write $x(t) = x_0 - gt^2/2$ if we consider that gravity acts along the x-axis. Therefore, both quantities need to be fitted to some parabola from which each measurement can provide one data point. Results of such a procedure are illustrated in Figs. 3.8 and 3.7 for both PG-cooled MOT and Dark MOT (without PG-cooling). For the PG-cooled MOT, the temperature go as low as 20μK and we can clearly see the MOT falling down in the camera shots. However, for the Dark-MOT preparation, the measured temperature rise up to 320μK and we clearly see the quick ballistic expansion of the MOT in the pictures.

2.2.2 Decrease of OD after B-field off

In our experiment, it is usually easier to measure the optical depth of our atomic ensemble rather than measuring its temperature with a full time of flight measurement. When working on the temporal dark-MOT we noticed that the OD was decreasing quite rapidly with time since one half of OD was lost after 2 ms. This is generally not suitable for a memory implementation since we want to perform the experiment trials in this 1 or 2 ms window. To keep a constant OD we would need to reduce this acquisition time, meaning that the rate at which we can take some data would be greatly decreased.

To better understand how the decrease of optical depth is affected by the temperature, we designed a model that takes into account the ballistic free-fall of the atomic cloud, as presented in the previous section and illustrated on Fig. 3.9. The idea is to infer the temperature of our ensemble from OD measurements.

Model We first consider a Gaussian density distribution for the atomic cloud, for all 3 directions of space. We set z as the propagation axis, and x as the vertical axis. We consider that the cloud will fall due to gravity, with no initial velocity. We also consider the ballistic expansion of the cloud due to temperature, i.e. the width of the axial distributions depend

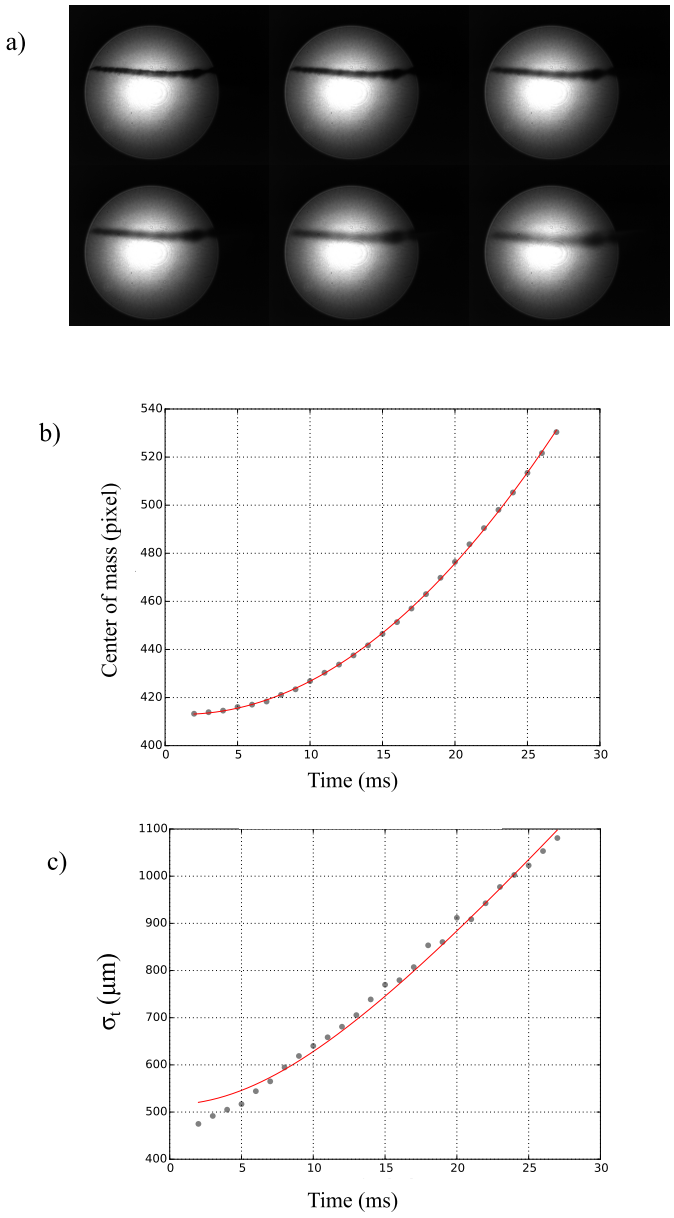

Fig. 3.7 *Time-of-flight measurement for the PG-cooled MOT. a) Pictures of imaging measurements at times {2,4,6,8,10,12} ms. We select one vertical cut of these image and record the evolution of the atomic distribution with time. b) The free-fall of the atomic cloud makes the maximum of the distribution to fall according to* $x(t) = x_0 - gt^2/2$. *This allows us to calibrate the distance between each pixel. c) Expansion of the cloud as a function of time. The temperature is extracted from the fit of Eq. 3.11 and is found to be 20* μK.

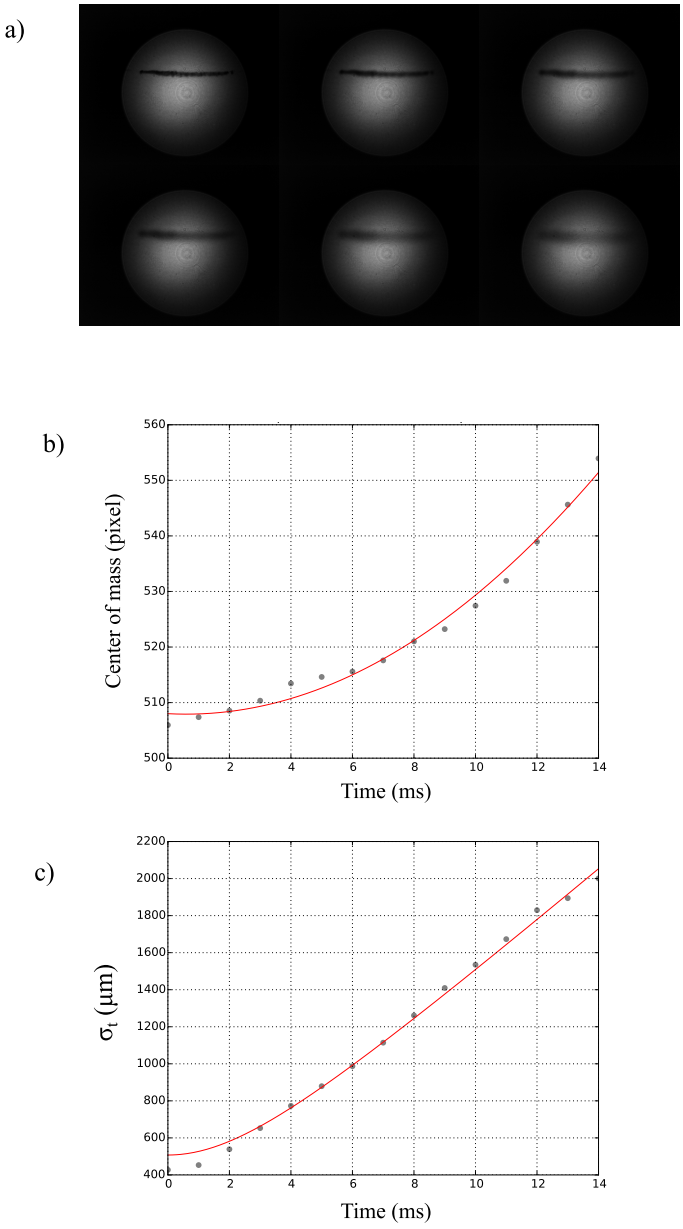

Fig. 3.8 *Time-of-flight measurement for the temporal dark MOT. a) Pictures of imaging measurements at times {2,5,8,11,14,17} ms. We select one vertical cut of these image and record the evolution of the atomic distribution with time. b) The calibration is done similarly to that of Fig. 3.7. c) The expansion of the cloud as a function of time. The temperature is extracted from the fit of Eq. 3.11 and is found to be 320 μK.*

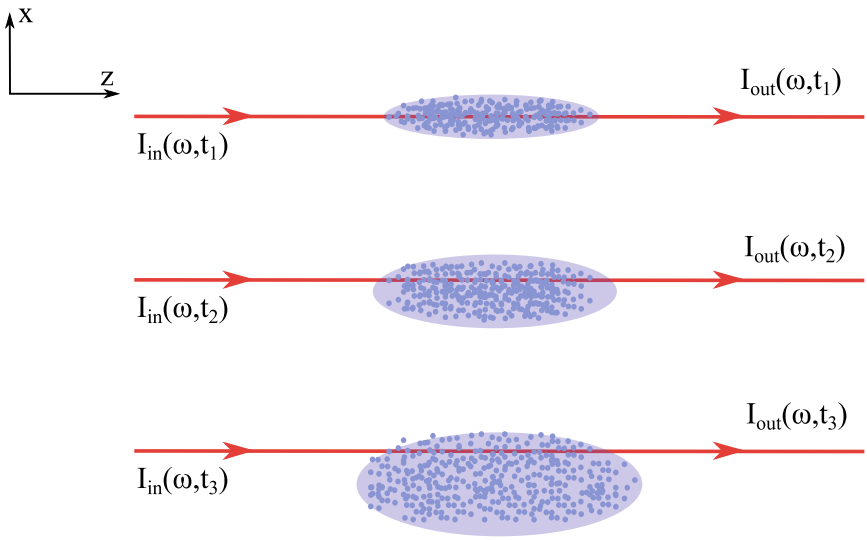

Fig. 3.9 *Considered scheme for the decrease of OD after release due to gravity and ballistic expansion. We represent here three times at which we probe the OD* $\{t_1, t_2, t_3\}$.

on time. The density distribution can thus be written :

$$n(x,y,z,t) = \frac{1}{\mathcal{N}_{3D}(t)} \exp\left(\frac{-(x+\frac{gt^2}{2})^2}{2\sigma_x^2(t)}\right) \exp\left(\frac{-y^2}{2\sigma_y^2(t)}\right) \exp\left(\frac{-z^2}{2\sigma_z^2(t)}\right) \tag{3.12}$$

with

$$\sigma_{x,y,z}^2(t) = \sigma_{x_0,y_0,z_0}^2 + \frac{k_B T}{m} t^2 \tag{3.13}$$

and

$$\mathcal{N}_{3D}(t) = \sqrt{(2\pi)^3 \sigma_x^2(t)\sigma_y^2(t)\sigma_z^2(t)} \tag{3.14}$$

being the normalization constant that depends on time. We consider that our probe has a Gaussian transverse intensity profile and that it is perfectly collimated, which is in most cases a valid approximation in our experiment since the rayleigh range z_R is much larger than the length of the cloud.

$$I(x,y,z) = \exp\left(\frac{-x^2}{w_0^2}\right) \exp\left(\frac{-y^2}{w_0^2}\right) I(z). \tag{3.15}$$

The probe detuning from the considered transition is Δ. The steady state photon scattering rate per atom is given by the following equation [Steck 1998]:

$$R_{sc} = \frac{\Gamma}{2} \frac{I_{in}/I_{sat}}{1 + 4(\Delta/\Gamma)^2 + I_{in}/I_{sat}}. \tag{3.16}$$

Therefore, the variation of probe power through the propagation axis z can be written as:

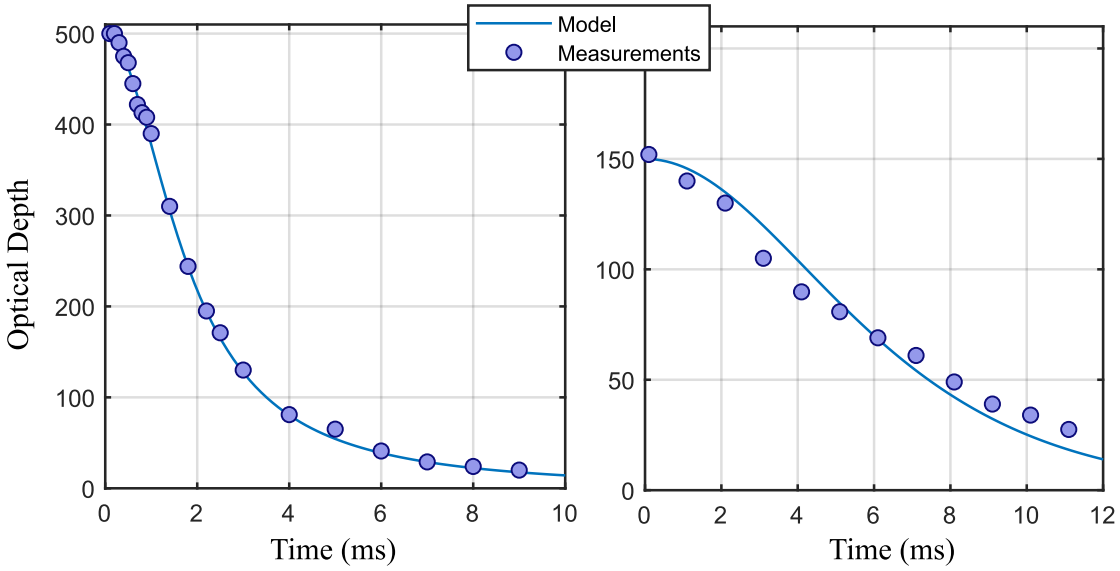

Fig. 3.10 *Decrease of optical depth as a function of time after release. (left): Decrease of the temporal dark-MOT. We experimentally observe a fast decay of the OD (from 500 to 200 after 2 ms). This is well fitted by the model which predicts a temperature of 340 μK, which agrees with the 330 μK found by the time-of-flight method. (right): Decrease of the PG-cooled MOT. The fit gives a temperature of 25 μK, also in agreement with the measured 20 μK with the time-of-flight technique.*

$$\frac{dP}{dz} = -\hbar\omega N_0 \iint R_{sc}(x,y,z)n(x,y,z,t)dxdy \tag{3.17}$$

where N_0 is the number of atoms seen by the probe. Now, from $dP = P(z+dz) - P(z)$, with $P(z) = I(z)\iint dxdyI(x,y)$, we obtain the following differential equation :

$$\frac{dI}{dz} = -\frac{K_1 K_2(t)}{K_3} I(z) \exp\left(\frac{-z^2}{2\sigma_z(t)}\right). \tag{3.18}$$

For simplicity we have defined K_1, K_2 and K_3 as :

$$K_1 = \frac{\Gamma}{2I_{sat}} \frac{\hbar\omega}{1+4(\Delta^2/\Gamma)^2}, \tag{3.19}$$

$$K_2(t) = \frac{N_0}{\mathcal{N}_{3D}(t)} \iint \exp\left(\frac{-x^2}{w_0^2}\right) \exp\left(\frac{-y^2}{w_0^2}\right) \exp\left(\frac{-(x+\frac{gt^2}{2})^2}{2\sigma_x^2(t)}\right) \exp\left(\frac{-y^2}{2\sigma_y^2(t)}\right) dxdy \tag{3.20}$$

and

$$K_3 = \iint \exp\left(\frac{-x^2}{w_0^2}\right) \exp\left(\frac{-y^2}{w_0^2}\right) dxdy. \tag{3.21}$$

We define $K(t) = K_1K_2(t)/K_3$ and $B(t) = 2\sigma_z(t)$ for simplicity. Equation 3.18 has an analytical solution given by :

$$I(z,t) = C_1(t)\exp\left[-\frac{1}{2}\sqrt{\pi}K(t)\sqrt{B(t)}\,\mathrm{erf}\left(\frac{z}{\sqrt{B(t)}}\right)\right]. \tag{3.22}$$

$C_1(t)$ being the integration constant which is defined by the initial condition $I(-\infty) = I_{in}$:

$$C_1(t) = I_{in}\exp\left(-\frac{1}{2}\sqrt{\pi}K(t)\sqrt{B(t)}\right). \tag{3.23}$$

From this expression, one can easily retrieve the optical depth at a given time since the absorption of the probe at a given time is $A(t) = 1 - I(\infty,t)/I_{in}$, and the on-resonance OD is : $-\ln(1-A)(1+4\Delta^2/\Gamma^2)$.

Also, it may be easier to define the ratio N_0/I_{sat} as a function of $\mathrm{OD}(t=0) = \mathrm{OD}_0$ since it is difficult to know precisely the number of atoms in the interaction zone, or the I_{sat} value with precision, but it is easy to experimentally measure the optical depth of our ensemble. This ratio is given by :

$$\frac{N_0}{I_{sat}} = \frac{2\,\mathrm{OD}_0\,K_3}{\hbar\omega\Gamma K_2(t=0)\sqrt{\pi B(t=0)}/N_0}. \tag{3.24}$$

Results The results are presented in Fig. 3.10 with absorption measurements. The model fit to the data gives temperatures that correspond to the time-of-flight measurements: 25 μK for the PG-cooled MOT (20 μK with time-of-flight technique) and 330 μK for the temporal Dark MOT (320 μK with the time-of-flight technique). Two regimes appear from this model: for low temperatures, the loss of OD is only due to the free-fall of the cloud and for high temperatures the ballistic expansion dominates the dynamics.

2.3 Magnetic field cancellation

We have previously seen that the presence of a magnetic field during the storage process induces a decoherence of the collective excitation, leading to a decay of efficiency with storage time. The DC component of the Earth's magnetic field is the first contributor to this stray field, and has a typical value of 0.5 G. The next residual magnetic field contribution is due to the Eddy currents in surrounding electrical conductors, induced by the fast extinction of the trapping B-field. These unwanted magnetic fields are cancelled by a set of compensation coils that aims to generate an opposite field around the probe propagation axis during the time memory experiments are performed.

2.3.1 Microwave spectroscopy

To assess the magnitude of this magnetic field in our interaction area, we perform Raman spectroscopy of the atoms [Ringot et al. 2001]. The principle of Raman spectroscopy is shown in Fig. 3.11 for atoms prepared in the F=3 ground state. The residual magnetic field lifts the degeneracy of magnetic Zeeman sublevels along a quantization axis defined by the magnetic field. A pulse of microwave at frequency close to the ground state splitting resonance $\omega_{hf} = 9.2$GHz is sent to the atoms. If this pump has a frequency that corresponds

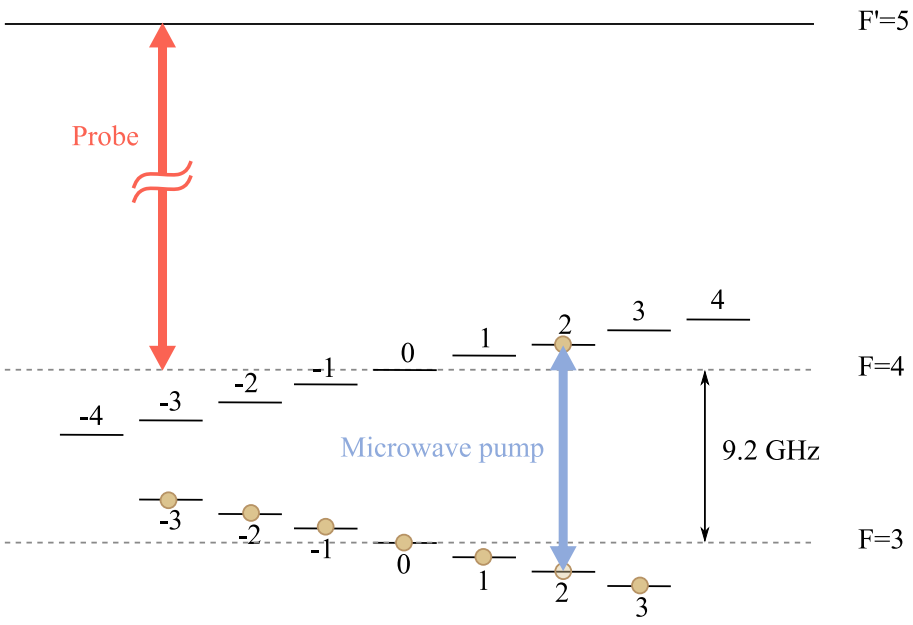

Fig. 3.11 *Level scheme and involved fields for microwave spectroscopy. Atoms are prepared in $F = 3$. A microwave pump pulse transfers some atoms in the Zeeman sublevels of $F = 4$ and the absorption of the $F = 4$ to $F' = 5$ is probed. This measurement is repeated for several values of microwave frequencies.*

to a transition $|F = 3,m_F\rangle \rightarrow |F = 4,\{m_F - 1,m_F,m_F + 1\}\rangle$, some atoms will be transferred in the corresponding $F = 4$ Zeeman state depending on the pulse duration. Shortly after, a probe pulse resonant with the $|F = 4\rangle \rightarrow |F' = 5\rangle$ is sent through the same path than the one described in Fig. 3.5 in order to measure absorption. This measurement is repeated for several frequencies of the microwave pump and the obtained profile in OD displays absorption peaks that correspond to each Zeeman transition. A typical Zeeman spectrum is displayed on Fig. 3.12 where we observe all 15 possible π, σ^+ and σ^- transitions. Although it is not straightforward to come back to the distribution of population in the Zeeman levels, this spectrum can still give some information about it. For an optically pumped ensemble to the $|F = 3,m_F = +3\rangle$ state, only three peaks will appear on the right side of the spectrum. Also, if there is imperfect pumping to one side of the Zeeman levels, it also possible to see it through the assymmetry of the peak heights.

2.3.2 Static and dynamic cancellation

The residual B-field can be estimated from the distance between the spectroscopic peaks, since the distance between each Zeeman levels depends on the B-field magnitude. In order to compensate the magnetic field, three pairs of coils are placed around the chamber where each coil has an independent controllable current source. Therefore, we are able to cancel DC magnetic fields and first order gradients. We optimize these currents by monitoring

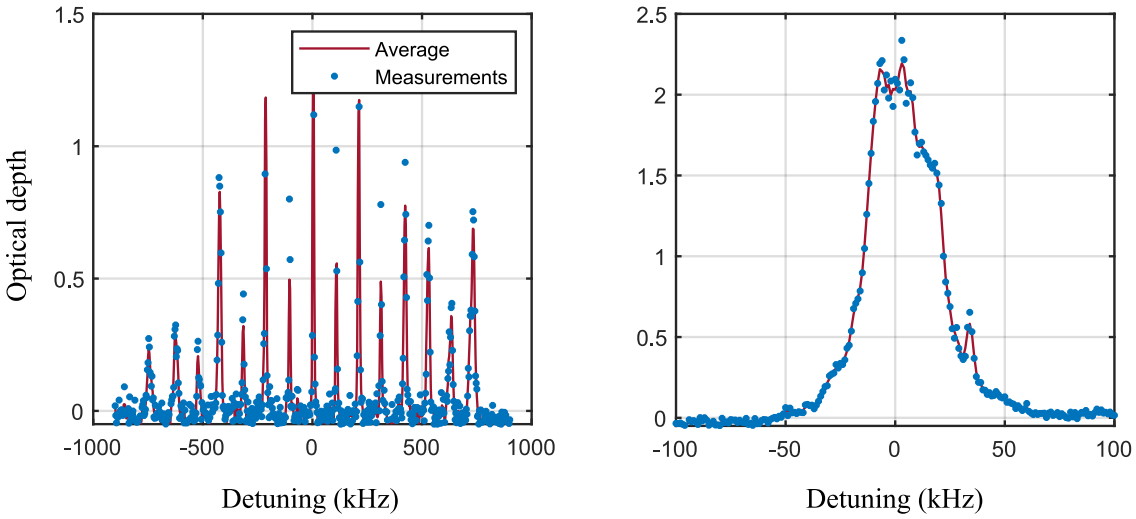

Fig. 3.12 *Microwave spectroscopy. (left): When a magnetic field is applied on the atoms, the degeneracy of Zeeman sub-levels is lifted and we observe a set of 15 peaks corresponding to each transition between the Zeeman sub-level of $F = 3$ and $F = 4$. (right): We cancel the residual magnetic field by applying an opposite field thanks to individually controllable additional coils placed around the chamber. When the magnetic field is cancelled, inhomogeneous broadening of the order of 30 kHz can be obtained, equivalent to an effective B-field gradient of 50 mG/cm.*

the spectrum and trying to gather all the peaks in the center by changing the currents. A cancelled spectrum is displayed on Fig. 3.12 (right). The inhomogeneous broadening of the ground state is limited to 30 kHz, which can be translated into an effective gradient of $B_1 = 50$ mG/cm along the probe axis (see Section 4.2). This value of inhomogeneous broadening limits the memory time to 15 μs in our experiment.

The time at which we perform this measurement is also important. Usually in our experiment, magnetic field fluctuations can persist for up to 2ms after the extinction of the MOT magnetic field. Therefore we decided to perform the experiment after this 2ms time in order to have a stable cancellation of the magnetic field. However, during my PhD we noticed that this was not the case anymore since the inhomogeneous broadening was not stable over time. For a cancelled residual magnetic field of 50 kHz at a time of 2.5 ms we obtained values as high as 200 kHz 150 μs after. As we see on Fig. 3.13 a), one pair of coil was producing long-lived Eddy currents during a time superior than 5 ms. Using a current clamp to measure the current in the coils after the extinction of magnetic field, we did not notice any problem as the current vanished in less than a millisecond. We did not find the exact reason of this unwanted non-stationnary magnetic field after extinction and it ultimately lead to developping a method to cancel this non-stationnary residual magnetic field by dynamically controlling the cancellation coils.

To optimally cancel this non-stationnary field during a time of 1 ms, we start by cancelling the field in the static way at ten different times during this millisecond, each one separated by steps of 100 μs. For each step, we save the values of current of each coils. Then, we apply a current with a time dependent profile to each coil, in which we applied the interpolation of

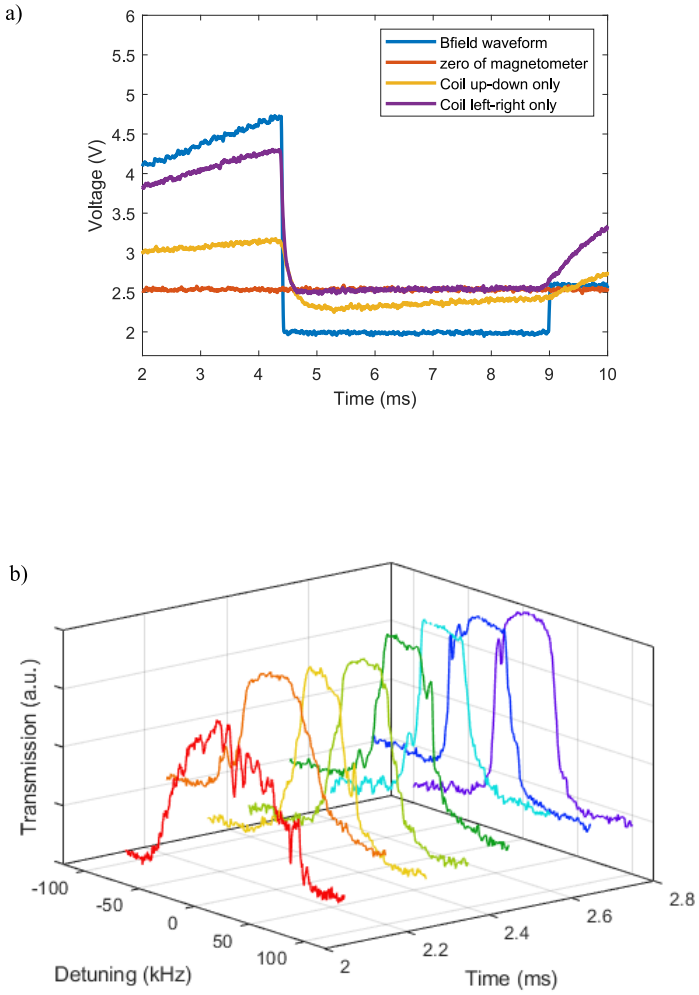

Fig. 3.13 *Dynamic cancellation of magnetic field. a) Magnetometer measurements. The yellow and purple curve represent the magnetic field as measured by a magnetometer placed near the chamber in the case of only one pair of coils working. The purple curve goes to zero less than one millisecond after the B-field is shut-down as expected. The yellow curve however shows that a non zero field is present during the short period after the coils current is turned off. b) Microwave spectroscopy after applying the procedure to dynamically cancel the magnetic field. The current in the cancellation coils is individually ramped in each coil to always keep a cancelled magnetic field around the probe. Inhomogeneous broadening of around 50 kHz is obtained in average over the millisecond of interest.*

each values that were previously measured. After that, we checked that the cancellation was properly done by measuring the inhomogeneous broadening in between the previous selected time steps. More points can be added if some profiles are too large. Typical results obtained from this procedure are shown in Fig. 3.13 b. We get satisfying results that allow us to keep an inhomogeneous broadening of the order of 50 kHz along the millisecond in which we perform memory experiments. We note that this technique was developed at the end of this thesis and not used for the result reported in Chapter 4. This technique opens new opportunities to be explored for the preparation of the atomic ensemble.

3 MOT optimization

As we have previously seen, the optical depth is a crucial parameter to achieve highly efficient memories. In this section, we describe the main parameters that influence the optical depth and the optimization method we implemented. We also compare our temporal dark-MOT and regular PG-cooled MOT as well as we discuss the potential ameliorations that Zeeman pumping could provide.

3.1 MOT shape and probe direction

In order to make the MOT as optically thick as possible, the first consideration should be to optimize the MOT shape. We already said that we opted for a cigar-shaped MOT for the obvious reason that the probe will interact with more atoms along its path. This shape can be optimized by changing the direction of the six incoming trapping beams, and by changing the power balance between each pair of beams while monitoring the absorption. This balance can be easily modified by just turning a set of waveplates. The shape must be optimized in such a way that the MOT is really distributed along a straight line without any curvature. Sometimes, this optimization can lead to a slight change in the MOT position and the probe path needs to be realigned in the optimal path that maximizes the OD. Changing the probe path also modifies the magnetic cancellation since the residual magnetic field landscape might not be exactly similar in this new position. Changing the magnetic cancellation can also result in changing the shape and position of the MOT. Therefore, this optimization must be done in a highly recursive way by going back and forth between all of these optimization steps. This is a tedious operation since for example, a simple change of the probe direction involves the necessity to realign all the optics placed after the MOT.

3.2 Experimental parameters

Optimized time sequences are presented in the first section of this chapter. Here we will present the evolution of OD as a function of several experimental parameters, both for the PG-MOT and dark-MOT optimization.

PG-Cooled MOT One of the first parameter to optimize is the trapping detuning Δ_0 since this parameter sets the size of the trap and the magnitude of both forces described in Section 1.3. The magnitude of both the molasses friction force and pressure force is proportional to the parameter $|\alpha|$ given by Eq. 3.6 which is dependent on Δ_0. The force is maximum when $\Delta_0 = \Gamma/2$. However, for this detuning the corresponding size of the trap confinement

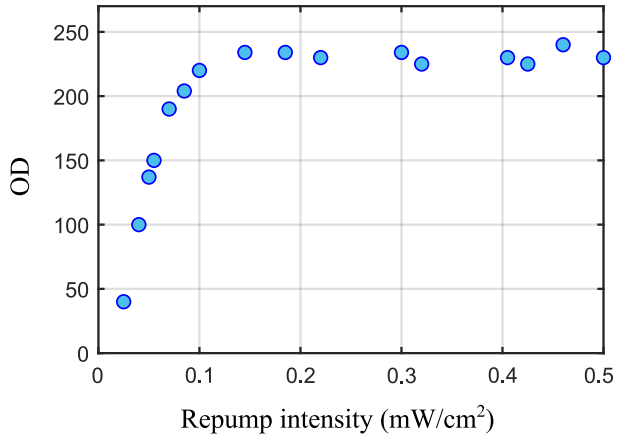

Fig. 3.14 *Optical depth as a function of repump intensity for the PG-cooled MOT. Once the intensity is greater than 0.2mW/cm^2, the average time spent by an atom in the dark state is zero.*

is small and therefore the OD is small too. This could be compensated by increasing the power of the trapping beams rather than increasing the detuning. However, in practice we are limited in power and a tradeoff must then be found to optimize this number. In our experiment the highest ODs are obtained around $\Delta_0 = -17$ MHz.

During the cooling cycle, there is a non-zero probability that an atom might decay via an off-resonant interaction to the other ground state $F = 3$, escaping the cycle. To counter this effect, we shine a repump beam on the ensembles, resonant with the 3-4 transition. For a regular MOT, the optical depth is maximized when the repump intensity reaches a saturation value which means that the average time spent in the dark state vanishes. For our system this value is found to be 0.2 mW/cm^2.

The optical depth can be further increased by compressing the MOT at the end of the loading phase. This is done by ramping up the current in the magnetic coils. Experimentally, it is observed that for a higher gradient we obtain a better OD. Eventually, we are limited by the coils to a maximum value of current of around 18A.

Temporal dark MOT In order to reach high OD values in an easier manner, we decided to experiment with a temporal dark MOT as this would yield access to denser atomic cloud. Recent demonstrations with cesium have proven the ability to reach optical depths as high as 1000 [Hsiao et al. 2014], which can translate to an efficiency greater than 95% for a D_1-line memory. By using the timing sequence presented in Fig. 3.4, we are easily able to reach optical depths greater than 500. The idea is to reduce the repump intensity during the compression phase in order to have a fraction of atoms in the dark state $\left|6S_{1/2}, F = 3\right\rangle$. The atomic density increases due to the reduction of photon reabsorption. However, if the repumping intensity is too weak, the atomic density starts to decrease again due to the reduction of the trapping force. There is therefore an optimal intensity that needs to be found in order to optimize the OD. This is shown of Fig. 3.15 where the optimal intensity is found to be around 0.01 mW/cm^2. On the other hand, we found experimentally that adding

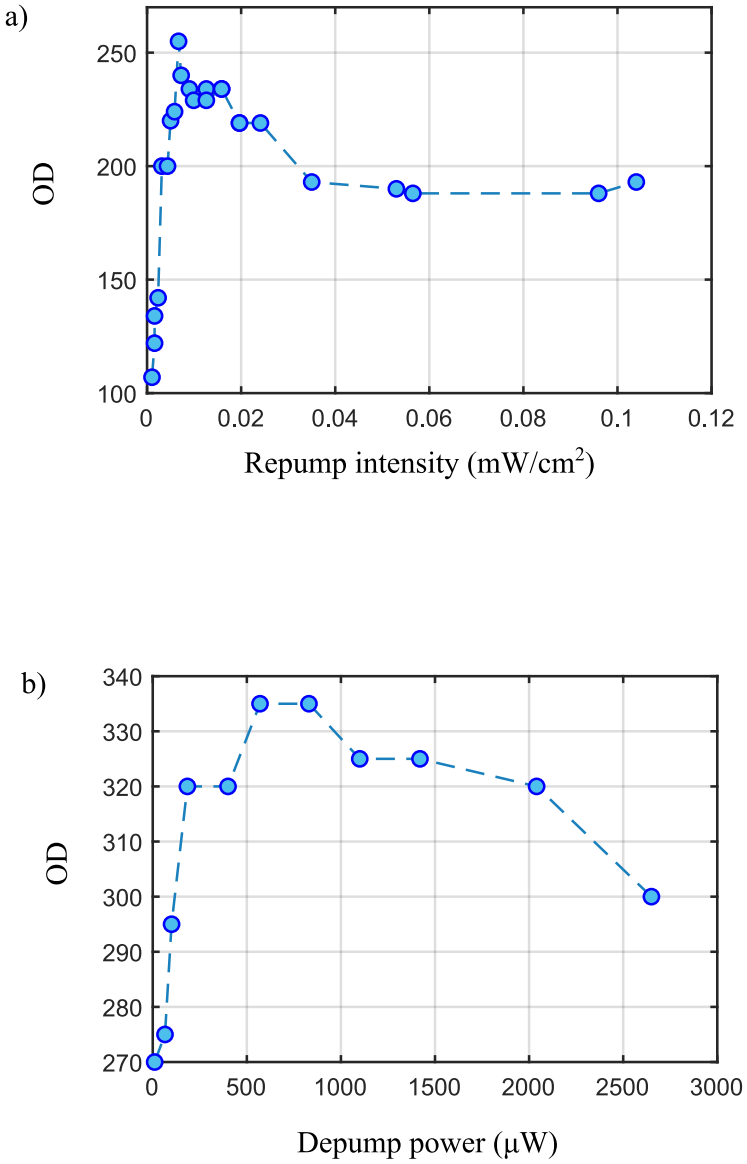

Fig. 3.15 *Temporal dark MOT. (top): Evolution of the optical depth as a function of the repump intensity in the cloud. The optimal intensity is found to be around 0.01 mW/cm^2. (bottom): Adding a depumping beam is essential to optimize the temporal dark-MOT. The evolution of OD for various powers in the depumping beam is maximum for around 1 mW of power.*

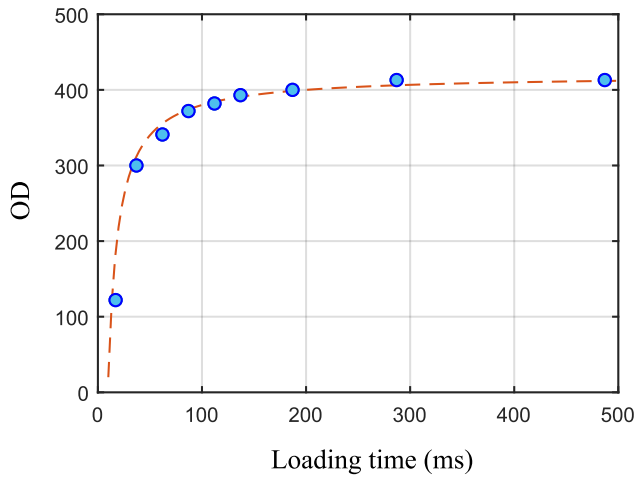

Fig. 3.16 *Evolution of OD as a function of loading time for the temporal dark MOT. The OD saturates at time around 200 ms however, operating at this time reduces significantly the experiment's repetition rate and we usually choose to perform our experiment with a 50 ms loading time.*

a depumping beam to help the dark-state pumping was essential. The addition of this beam also shifts the optimal repump intensity to slightly higher values. This optimization must be performed in an iterative way to solve this two-parameter optimization. Fig. 3.15 displays the evolution of the OD as a function of depumping power when the repumping intensity is 0.02 mW/cm^2. At the optimal value, the OD is increased by a factor 1.25.

Loading time It is also possible to further improve the optical depth by increasing the loading time of the MOT as shown in Fig. 3.16. However, we also want to optimize the duty cycle of the experiment defined by the ratio of the time window in which the experiment is performed and the overall time period of one cycle:

$$\mathcal{T}_{dt} = \frac{t_{exp}}{T}. \tag{3.25}$$

If $\mathcal{T}_{dt}$ is too large, the time to take a statistically significant amount of data might be too long. We usually set the loading time between 50 ms and 120 ms depending on the experiment we want to perform.

3.3 Zeeman pumping

Another way to improve the optical depth is to pump to a specific Zeeman state. We have previously seen that the optical depth of a transition $F \to F'$ is directly proportional to the coupling constant squared g^2 (see Eq. 2.47). The atom-photon coupling constant is derived from the interaction Hamiltonian to be

$$g = \langle F | \, d \, | F' \rangle \sqrt{\frac{\omega_{FF'}}{2\hbar\epsilon_0 \mathcal{V}}} \tag{3.26}$$

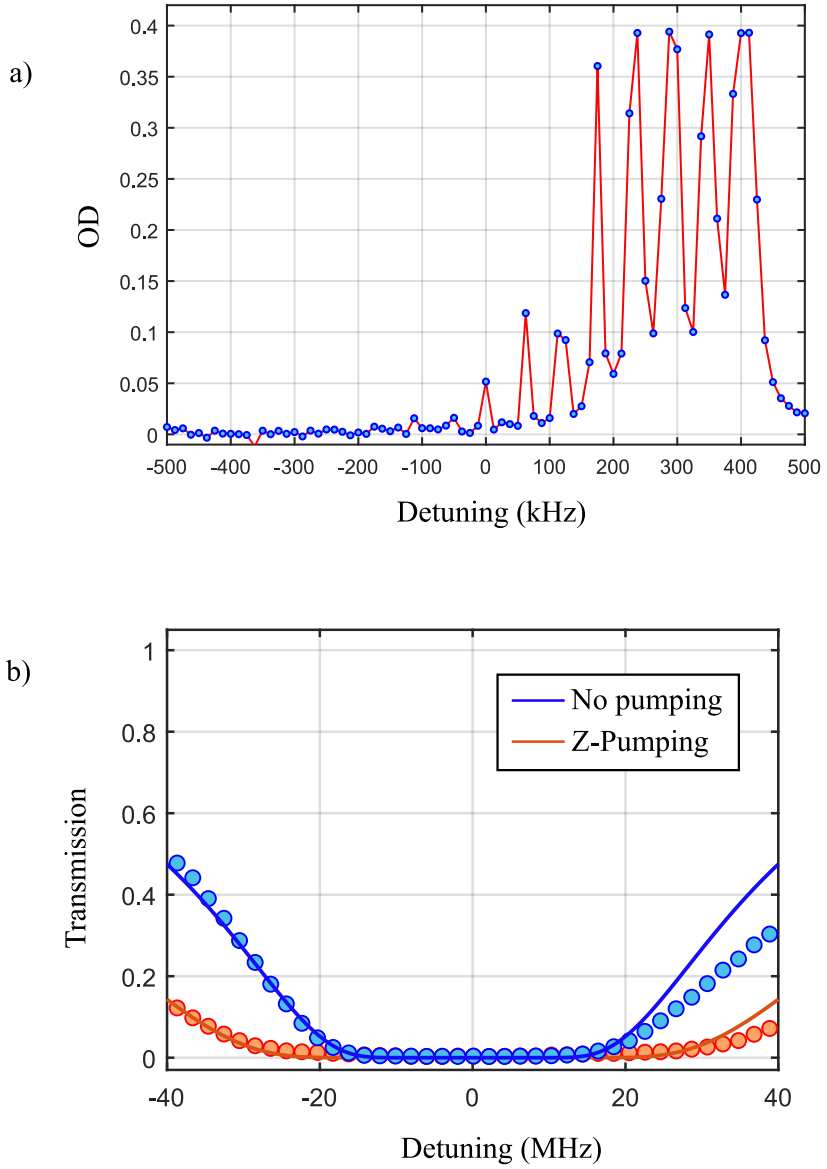

Fig. 3.17 *Zeeman pumping. a). Microwave spectroscopy of atoms after Zeeman pumping in the edge state $m_F = +3$. A perfect pumping would lead to only three visible transitions in this spectrum which is not the case here. There are no atoms that populate the left side of the Zeeman levels manifold. b) The optical depth can be greatly increased by this technique. The blue curve represent an OD of 250, without any pumping. After pumping, the OD is measured to be around 600 (in red).*

where $\omega_{FF'}$ is the frequency of the transition, $\mathcal{V}$ is the mode volume and $\langle F|\, d\, |F'\rangle$ is the dipole matrix element. The optical depth is thus proportionnal to the square of the dipole matrix element. For a specific $F,m_F \rightarrow F',m_{F'}$ transition it writes

$$\mathrm{OD} \propto \left|\langle F,m_F|\, d\, |F',m_{F'}\rangle\right|^2 \propto \left(\mathcal{C}_{F,m_F}^{F',m_{F'}}\right)^2 \tag{3.27}$$

where $\mathcal{C}_{F,m_F}^{F',m_{F'}}$ is the Clebsch-Gordan coefficient of the considered transition. If we consider a circularly polarized probe σ^+ relative to the quantization axis, resonant with the $|F=3\rangle \rightarrow |F'=4\rangle$ transition of the D_1-line and an homogeneous distribution of population in the Zeeman sublevels, the relative strength of the transition is equal to the mean of each squared Clebsch-Gordan coefficient of all possible σ^+ transitions, which is equal to 0.25 in that case. The case where only the $m_F = 3$ ground state is populated gives a relative strength of the transition equal to 0.58. In that case, it means that the OD could theoretically be increased by a factor 2.3.

We attempted to experimentally make use of this pumping. A small magnetic field was applied on the probe propagation direction to split the Zeeman sub-levels along this axis and a 20 μs pulse resonant with the $|F=3\rangle \rightarrow |F'=2\rangle$ transition was sent to the atoms just after the molasses phase. The pumping beam had a 5 mm diameter and was sent from both forward and backward directions. Its polarization was fine-tuned by a set of two $\lambda/2$ and one $\lambda/4$ waveplates. We performed microwave spectroscopy to observe the influence of the pumping on the Zeeman levels distribution and observed a significant pumping to the edge of the manifold (see Fig. 3.17). Perfect pumping would yield three absorption peaks on the edge of the microwave spectrum accounting for all $m_F = 3 \rightarrow m_{F'} = 2,3,4$ microwave transitions. However even after fine-tuning the polarizations we did not manage to reach a perfect pumping. The optical depth was nevertheless increased by a large amount, from 250 to 600 as shown in Fig. 3.17. This 2.4-fold improvement is greater than expected for an imperfect pumping and can be explained by the slight assymmetry in the initial distribution of the population without pumping. If the population is larger in the negative sub-levels, the resulting average transition strength is smaller than the case of an homogeneous distribution. Such assymetry can be caused by the multiple interactions and pumping effects taking place during the molasses phase, for example.

The downside of this technique is that a magnetic field is necessary to define the quantization axis. Even if the optical depth can be significantly increased, the use of a DC-field induces a fast decoherence of the collective excitation which decreases the storage time by a great amount. A good alternative would be to pump the atoms to the magnetically insensitive state $m_F = 0$ which offers the benefit to completely cancel the magnetically induced decoherence and increases the optical depth by a factor of 1.25 compared to the homogeneous population distribution. However, this type of pumping is quite complex to achieve and is beneficial only in the case of perfect pumping.

4 Experimental apparatus

We now come to the description of our experiment, giving details of our apparatus. We start by describing our sources of light and their locking techniques, since at the beginning of my PhD we have installed two new laser-diodes and made them fully operationnal for performing

memory experiments on the D_1-line. After that, we detail various important aspects of the experiment and explain our detection system.

4.1 Light manipulation

4.1.1 Lasers

We use four main lasers in our experiment. The first one is a Ti:Sapphire laser (MSquared, SolsTiS) pumped by a 10 W continuous-wave laser at 532 nm (Lightouse photonics, Sprout-G). The Ti:Sa laser outputs a 852 nm light with a power of around 2 W. This light is locked on a saturated absorption peak of the cesium D_2-line and its power is distributed between our experiment and the neighbouring nanofiber experiment. We use this light for the trapping beams and aim to get as much power as we can. This laser seeds a tapered amplifier (Toptica Photonics, BoosTA). Eventually, we are able to deliver a total of 500mW for the trapping beams of our MOT. All other lasers are external-cavity diode lasers (Toptica Photonics, DL100) and are used for the probe, control, write, read and repump beams.

4.1.2 Pulse shaping and frequency manipulation

All lasers are going through a set of acousto-optical modulators (AOM) in double-pass configuration, allowing the efficient generation of square pulses by turning on and off the RF voltage seeding the AOMs. The AC voltage is produced by a voltage-controlled oscillator (VCO) designed by our electronic workshop at LKB. By changing the oscillation frequency, we are able to tune the light frequency in a range of a few tens of MHz. To change the temporal shape of the square pulses, we can modulate the VCO output with a standard function generator using a frequency mixer (Mini-Circuits, ZAD-1-1). This allows us to go to length-tunable Gaussian pulses for the read beam of the DLCZ experiment, for example.

4.1.3 Locking techniques

Locking our lasers on specific atomic transitions is a mandatory requirement when working with cold atoms. In the following we present the main locking technique we use to lock our lasers and give some tips about their pratical realization.

Saturated absorption locking Both the Ti:Sapphire and the Toptica DL100 probe laser are locked via saturated absorption. It is done by shining the laser through an atomic vapor, retroreflecting the beam in the opposite direction and detecting the intensity of this retroreflection. The first beam saturates the desired transition for a specific class of atomic velocities. The retroreflection will adress different atoms due to thermal motion except for those who have a velocity vector perpendicular to the wavevector of our beam. When some light of the second beam sees an excited atom, there is a good chance that this atom undergoes stimulated emission, thus leading to a dip in the standard Doppler absorption line, centered around resonance. By scanning the laser frequency, we get absorption profiles as in Fig. 3.18 where we can observe the four transitions of the D_1-line. To get an error signal from this setup, we modulate the frequency of the laser and demodulate the detected signal with a lock-in amplifier. This produces an error signal which is easy to lock onto with standard PID systems with feedback on the piezo of the laser cavity. However, we noticed the

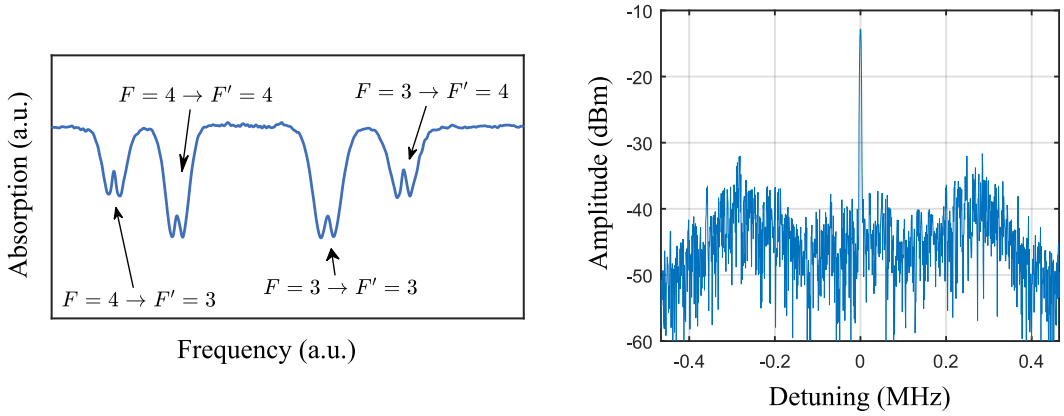

Fig. 3.18 *Laser locking. (left): Absorption profile of a scanning laser around the D_1-line in a saturation absorption setup. (right): Locked beatnote of the probe and control diodes. The amplitude difference between the peak and the noise is around 30 dBm.*

importance of modulating the laser externally rather than directly modulate the current of the diode. Indeed, we observed that this internal modulation produces some phase noise that is not negligible in our applications, this can be seen for example by probing the absorption on a steep absorption slope and observing that the signal oscillates a little bit. Reducing the amplitude of the modulation degrades the lock quality and thus this implementation was not satisfactory. We finally opted for an external modulation done using an AOM.

Beatnote Locking Once a first laser is locked on resonance to a specific transition, for example the D_1 probe laser locked to the $\left|6S_{1/2},F=3\right\rangle \rightarrow \left|6P_{1/2},F'=4\right\rangle$ transition, we perform phase locking on a second laser. This phase-locking, or beatnote-locking, relies on the comparison between the beatnote of the interference of the two lasers and a reference microwave signal. For example, the control laser on the $\left|6S_{1/2},F=4\right\rangle \rightarrow \left|6P_{1/2},F'=4\right\rangle$ transition should give a beatnote with the probe laser centered on the hyperfine frequency $\omega_{hf} = 9.12$ GHz. This beatnote is produced by mixing the two lasers and focusing the mixed light on a very fast photodiode with a time response of 30 ps (Hamamatsu G4176). This electronic signal is amplified by 30 dB and is sent to a commercial locking circuit (Vescent D2-135) which allows the locking of this beatnote to the microwave signal by feedbacking on the current of the diode laser. A typical locked beatnote between the signal and the control is presented in Fig. 3.18.

Polarisation spectroscopy locking During the installation of the new D_1-line lasers we tried to lock the probe using polarization spectroscopy since it does not invlove any modulation of the field. We followed the scheme presented in [Pearman et al. 2002]. The idea is to use a weak probe beam to analyse the birefringence in a vapour cell induced by a strong counterpropagating pump beam with a circular polarization. This probe is then sent onto a polarizing beam splitter in order to detect separately the horizontal and vertical polarization

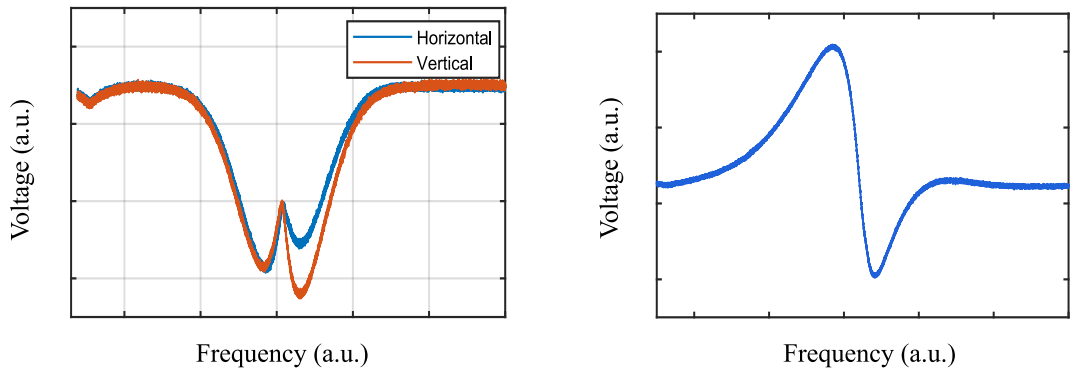

Fig. 3.19 *Polarization spectroscopy locking. (left): Probe intensity for detectors placed in the horizontal and vertical outputs of the polarizing beam splitter. Notice the assymetry of the two signals. (right): Error signal obtained by substracting both signals. This error signal is obtained without any modulation of the probe light.*

components on a photodiode. Each signal corresponds to a saturated absorption signal but they are assymmetric due to the induced birefringence in the medium. An error signal to lock on can be obtained by performing a balanced substraction of the two electric signals generated by the photodiodes. The obtained absorption profiles and error signal are presented on Fig. 3.19. This technique has the advantage to deliver a nice error signal with no modulation of the light. However, we observed after some time that the zero-crossing of the error-signal was not stable with time on relatively short-scale, inducing instability of the laser frequency on a range of a MHz which is significant in our experiments. This is due to small variation of the pump power and the fact that a few optics have temperature-dependent birefringence properties. We eventually sticked to the external-modulation locking for stability reasons.

4.2 Atomic trap setup

We now turn on to the description of the atomic trap setup. We describe the vacuum components, our magnetic apparatus and finish with our detection system.

4.2.1 Vacuum components

Glass chamber In order to limit the Eddy currents around the atoms, we prepare our MOT in a glass chamber. This chamber has an anti-reflection coating on both sides to limit optical losses at 852 nm and keep the wavefront intact. For the D_1-line frequency, the probe is reflected by 3%. This glass chamber also has the advantage of having excellent optical access with 8 view ports on the $\{x,z\}$ plane and two large open windows on the $\{x,y\}$-plane (see picture). This chamber was designed before the beginning of this thesis work.

Dispensers The cesium source is provided by dispenser (or getters). A dispenser consists in a slitted metallic container which, once heated, releases a cesium vapor. The temperature of the dispenser is controlled by applying a current through it. We have 3 dispensers placed a few centimeters below the chamber that can be used separately or in series. The experiment

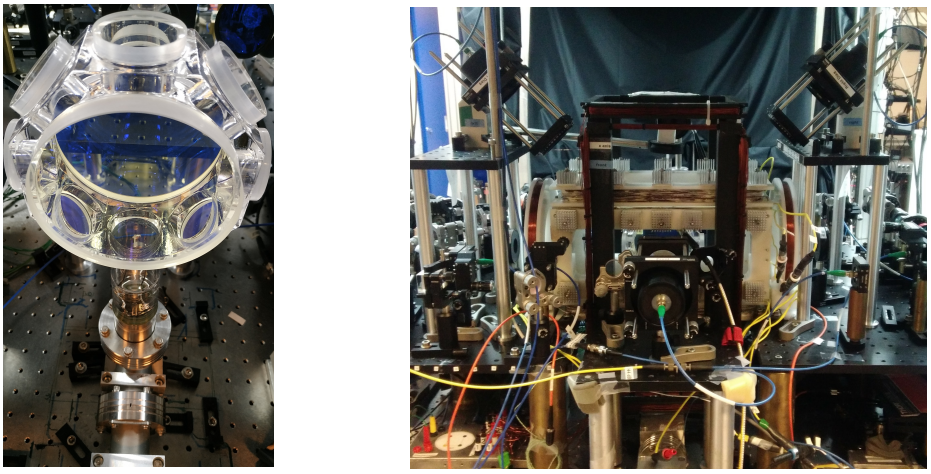

Fig. 3.20 *Experimental setup for the MOT. (left): Glass vacuum chamber. All surrounding optics and coils have been removed in this picture. (right): Setup for the MOT. The chamber is surrounded by two pairs of rectangular MOT coils, three pairs of cancellation coils, one pair of cap-coils and three collimators that output the trapping and repumping beams. The light beams are tuned on another optical table and sent with optical fibers to the collimators.*

is equipped with dispensers from SAES (SAES CS/NF/3.9/12FT10) with a typical lifetime of about 3 years.

During the course of this PhD work, we replaced the getters with new ones. To do so, we removed the vacuum chamber while nitrogen flowed in the vacuum system. The dispensers were then replaced while this flow was maintained to prevent any contamination of the vacuum system. Once the dispensers were installed and the vacuum pressure reached once again 10^{-9} Torr, we needed to "burn" the getters to activate them. Starting from 0A, the dispenser current was increased by 0.1A, while waiting for the pressure to go back down to its initial value before increasing again the current. This procedure was repeated until the pressure no longer went back down but, instead, increases with the current - this meant that a continuous flow of cesium was now coming out of the dispensers.

4.2.2 Magnetic field

Magnetic coils The magnetic gradient needed for the MOT is created by two pairs of rectangular coils to generate a quasi 2D-MOT. We decided to replace the system with a new set of coils during the course of my PhD to improve the system. Our first consideration was the wire radius, which had to be large enough to endure the heating produced by the resistivity of the coils. A larger coil radius allows a larger maximum current limit but increases the volume taken by the coils. Moreover, a larger wire is less bendable, making the winding more challenging. We decided on a wire radius of 0.8 mm, 0.05 mm thicker than the previous coils. Second, we decided to increase the number of turns in order to reach higher magnetic-field gradients, from 90 to 108 turns limited by the dimension of the holders. We

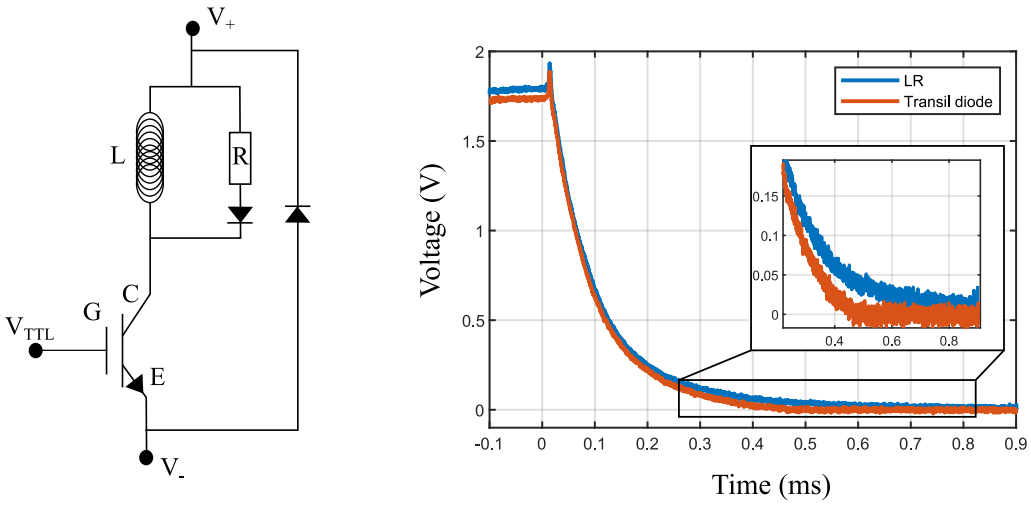

Fig. 3.21 *Fast switch of the main coils. (left): Schematic of the electronic circuit. The coils have an inductance L and are connected in parallel to a high power resistor and a diode to from a LR circuit. If we replace the resistor and diode by a transil diode, we can improve the decay time of the current. (right): Current decay as measured with an ampermetric claw. The tail of the exponential is suppressed in the circuit containing the transil diode such that there is zero current in the coils after* t=400μs.

built these new coils following a procedure in order to optimize the winding. To limit the heat, we applied a thin coating of thermal paste (RSpro, 2.9 W/mK) in between each row of wires and added some aluminum to the ertacetal rectangular holder. We measured the coils inductance to be 3.7 mH each with a resistance of 0.8 Ω. The coils can endure up to 20 A in continuous for an equivalent B-field gradient of 36 G/cm. Since the number of turns has been increased, the coils also need less current to load the MOT, which limits the heating. To further surpass the heating limitations, some experiment [Zhang et al. 2012] have opted for the construction of coils made of hollow-core copper wire in which water is flowing to cool the system in a more efficient way.

Electronic switch The main limitation in our experiment comes from the residual magnetic field around the atoms after the extinction of the main coils current. This limitation comes from Eddy currents, and residual current in the coil after its exctinction. Our goal is thus to completely shut down the current in less than a millisecond. To reduce the decay-time of the current extinction in the coils, which should decay as L/R, we designed a homemade fast switch with the help of the electronical workshop at LKB. The idea is to quickly discharge the load in a high-power resistor placed in parallel to the coil system. Decay times of the order of hundred of microseconds are achieved for both pairs of coils. We further improved the system by replacing the resistor and the diode with a transient-voltage-suppression diode (BZW-50). This transil diode operates by completely shutting down the current to zero such that any magnetic-field time variation vanishes. As we see on see Fig. 3.21, the tail of the exponential decay in L/R is supressed after 400μs in the transil diode circuit.

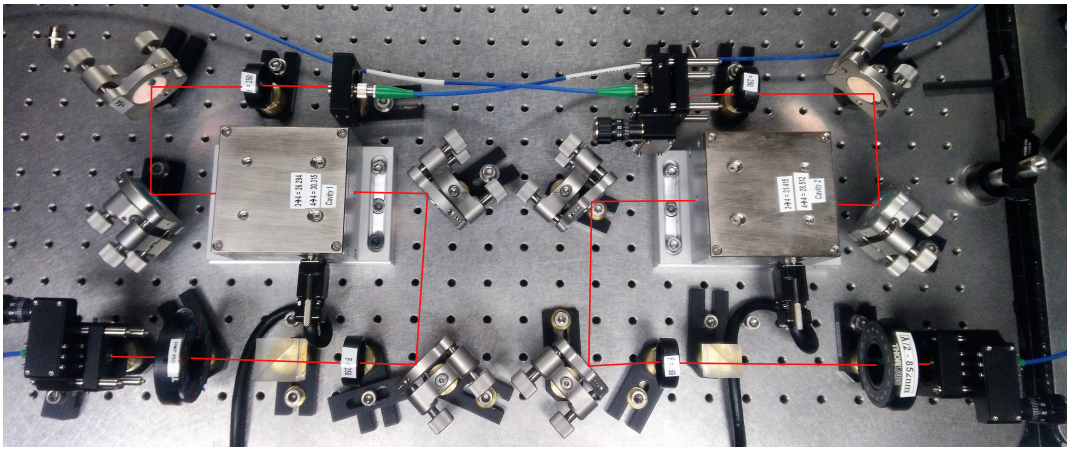

Fig. 3.22 *Filtering system. Two Fabry-Perot cavities are setup in a plug-and-play fashion and placed in a protective box on the optical table. Temperature stability to the mK is achieved and allow to filter out 40dB of control light background.*

Current sources The current source for the main coils must be capable of delivering 5 A in continuous to load the MOT and should also be able to deliver specific current profiles up to ∼20 A for the compression stage. We chose to use the commercial Delta Elektronika SM 52-30 that can be controlled by an external analog voltage. The compensation coils are driven by six homemade current generators that are also tunable in time with analog voltage ramps.

4.3 Detection system

4.3.1 Filtering of background noise

Memory experiments usually involve the storage of weak coherent states or single photons that must be distinguished from any background light. In our case, the control beam used to store and retrieve the signal pulse is the main source of background noise and its power is in the mW scale.

Most of the control light is filtered out by introducing a small angle with the signal beam propagation. Indeed, the signal pulse is collected after retrieval in a single-mode fiber, which effectively filters out control background. Increasing the angle could further reduce the amount of background, but as seen previously in this manuscript, a greater angle induces some additionnal decoherence due to motional dephasing (see sec 4.2). We are thus limited to angles ranging from 0.5° to 1.5°.

Further filtering is done by a set of Fabry-Perot etalon cavities (Quantaser FPE 001A). These cavities have a bandwidth of 60 MHz and a free-spectral range of 16 GHz. They are kept resonant with the desired frequency thanks to a set of temperature controllers that change the length of the cavity. To ensure a good temperature stability, the setup is placed in a plexiglas box on the optical table and stability at the mK level is achieved. This system allows for an additional filtering of 40dB while keeping a transmission of 70% for the signal frequencies. They can be used in series or in parallel for the storage of two distinct modes,

for example.

4.3.2 Single-photon detection

To detect single-photon events, we use avalanche photodiodes (APD) from the commercial company Excelitas (AQRH 14-FC). They have a detection efficiency of about 50% at 852 nm wavelength and a dark count rate of 50 Hz. We couple these APDs to an acquisition system based on a field-programmable gate array (FPGA). This allows us to perform logic operations on the electronic clicks and record coincidence events (two-fold coincidence and three-fold coincidence for the heralded $g^{(2)}$ measurement for instance, which will be presented in the next Chapter).

5 Conclusion

In this chapter we presented the tools and techniques for the preparation of atomic ensembles with high optical depth. We described the advantages and disadvantages between two main approach, the PG-cooled MOT and the temporal dark MOT. In general, the temporal dak MOT can give high values of OD at the price of a higher temperature (around 300μK), which is problematic in memory experiments. Besides, we described the techniques that we developped to optimize the absorption in the cloud, ranging from alignment considerations to optimization of parameters values. Eventually, we detailed our experimental apparatus by explaining which lasers we use and how we tune them to the desired frequencies, how we filter unwanted background noise and what kind of electronics we designed to cut-off unwanted magnetic field. Some of the improvements described here, as new coils or dynamical control of bias fields, were implemented at the end of this thesis and were not used for the experiment reported in the next Chapter.

Chapter 4

Efficient reversible mapping of photonic entanglement

Quantum networks rely on the transfer of quantum states of light and their mapping into stationary quantum nodes. Central to this endeavor is the distribution of entanglement between the material nodes, which opens a variety of major applications. The distribution of entanglement would be feasible with quantum repeaters made of segments that can store entanglement before swapping operations. In this context, the efficiency of the entanglement mapping is a key parameter. Working towards this goal, quantum state transfer and entanglement mapping between photonic modes and stationary quantum nodes has been demonstrated in different physical platforms. Seminal experiments of quantum memories with cold neutral atoms [Choi et al. 2008] or doped crystals [Clausen et al. 2011] have enabled the storage and retrieval of heralded single photon entanglement. Extensions toward high-dimensional [Zhou et al. 2015] and continuous-variable entanglement [Jensen et al. 2011] have also been reported. However, in all these implementations, the overall transfer efficiency was limited between 15% and 25%. Efficient entanglement transfer is a major challenge for network scalability and in this thesis we push this number close to 90%.

Our implementation relies on temporally shaped single photon pulses generated via the DLCZ protocol and on the dynamical EIT technique for reversible storage. The demonstrated capability required operating at a very large optical depth of the atomic ensembles on the D_1 line of cesium, and with a strong and preserved suppression of the two-photon component.

This chapter starts with a short review about entanglement storage before presenting the principle of our experiment. Then, we describe the work we did to build a single-photon source based on DLCZ that can match our quantum memory. We finish the chapter by showing the results of two experiments: the storage of single photons with high efficiency and the mapping of entanglement in and out of two quantum memories. This work was published in Optica [Cao et al. 2020].

1 Overview

In general, we distinguish experiments of measurement-induced remote entanglement generation compared to direct storage of entanglement experiments. Remote entanglement experiments focus on the generation of high quality entangled state between remote memo-

ries. Conversely, entanglement storage experiments usually involve an input entangled state and its mapping into and out of quantum memories. The quantum memories may not be remote, similarly to our experiment where the two modes are stored in the same atomic ensemble. More importantly, entanglement of remote memories requires active phase locking as demonstrated in [Chou et al. 2005] with cold atoms and more recently in [Lago-Rivera et al. 2021] with crystals, which is not the case in our implementation. Some experiments involve both aspects by storing an input entangled state into and out of remote quantum memories.

1.1 Seminal work

Remote entanglement Entangling quantum memories is the building block of the envisionned quantum repeater [Briegel et al. 1998], allowing scalable entanglement distribution over a network. The first demonstration of entanglement between remote memories has been realized in 2005 by Kimble's group at Caltech [Chou et al. 2005]. This experiment was motivated by the DLCZ protocol [Duan et al. 2001], initially proposed for the realization of scalable quantum communication networks in 2001. This protocol was demonstrated with two cold atomic ensembles separated by 2.8 meters.

Since then, several entanglement demonstrations between two individual nodes have been accomplished in different systems. In 2007, entanglement between remote ions separated by a few mm was demonstrated [Moehring et al. 2007] and the next year, entanglement between solid-state crystals doped with rare-earth ions was realized [Usmani et al. 2012]. Macroscopic diamonds were entangled in 2011 [Lee et al. 2011] and more recently, R. Hanson's team demonstrated high fidelity remote entanglement between NV centers in diamond that can be stored for more than 200 ms thanks to dynamical decoupling [Humphreys et al. 2018]. Heralded entanglement between two room-temperature atomic ensembles has also been shown [Li et al. 2021]. Jian-Wei Pan team's in China has recently demonstrated entanglement of cold atomic ensembles over a great distance of 50km [Yu et al. 2020].

Entanglement storage The ability to store an input entangled state into two quantum memories is a different kind of experiment. The first one has been realized in Kimble's group in 2008 [Choi et al. 2008] using atomic ensembles. Similarly to the experiment that will be presented in this chapter, a single photon is created with DLCZ, split on a beam displacer and stored in two quantum memories. Note that this experiment is not labeled as remote since the two memories are made of the same atomic-ensemble. The storage of heralded single photons entanglement has also been developed in doped crystals in 2011 [Clausen et al. 2011]. Recently, storage of heralded single photons entanglement into two remote crystal quantum memories was achieved at ICFO [Lago-Rivera et al. 2021]. Other experiments have demonstrated the ability to store entanglement using other degrees of freedom such as orbital angular momentum entanglement [Zhou et al. 2015] and continuous-variable entanglement [Jensen et al. 2011].

Efficient memories The realization of an efficient entanglement transfer into and out of quantum memories is made possible thanks to the recent improvement in efficiency with cold atomic ensemble memories. The recent work in our group [Vernaz Gris, Huang, et al. 2018] features a quantum memory for polarization qubit with 70% storage-and-retrieval efficiency.

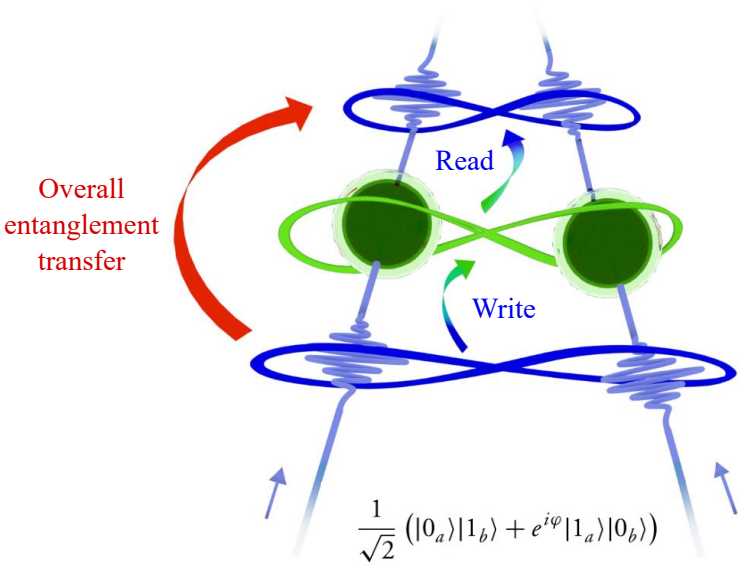

Fig. 4.1 *Reversible entanglement transfer. single photon entanglement is heralded, stored into two quantum memories, and read out on demand. We focus our study on the overall entanglement transfer of this process.*

It was at the time the largest recorded value for qubit quantum memories, improving the efficiency by 40% compared to previous work. Extension of this work to the D_1 line was demonstrated shortly after [Hsiao et al. 2018], showing a memory with 90% efficiency but not in the quantum regime. Recently, the team of Shengwang Du and Shi-Liang Zhu [Wang et al. 2019] presented a 90% efficiency memory for single-photon polarization qubits. We obtained similar results and extended the work to the storage of entanglement between to memories.

1.2 Principle of the experiment

We now explain the principle of the experiment we have done at LKB. As illustrated in Fig. 4.1, single-photon entanglement is first heralded and then stored into two quantum memories based on elongated atomic ensembles of cold cesium atoms. After readout, entanglement is detected and compared to the input.

The input entanglement state is created by impinging a heralded single photon with linear 45° polarization on a beam-displacer that separates $|H\rangle$ and $|V\rangle$ components into two distinct spatial modes. In the ideal case, the generated states write

$$|\Psi_{in}\rangle = \frac{1}{\sqrt{2}}\left(|0_a\rangle\,|1_b\rangle + e^{i\varphi}\,|1_a\rangle\,|0_b\rangle\right)$$

where a and b denote the two optical paths and φ is the phase difference between the two paths. This state is stored in a multiplexed way in our EIT memory, effectively generating entanglement between two separated spin-waves (in green on Fig. 4.1). After a programmable delay, the atomic memories are read out and the state is mapped back to its photonic form. The two modes are recombined and sent to an analysis platform that reconstructs the density

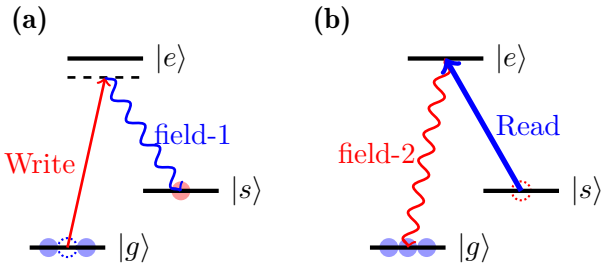

Fig. 4.2 *The atomic scheme for the DLCZ protocol.* ***(a)*** *A weak detuned write pulse is sent to the ensemble. It creates a field-1 photon via Raman scattering to the* $|s\rangle$ *state.* ***(b)*** *After a short delay, a strong read pulse is sent to read out the collective excitation. A field-2 photon is generated in a well defined spatio-temporal mode defined by the mode-matching condition.*

matrix of the state. We characterize the state with and without storage to assess the overall entanglement transfer λ of the process. The focus of our study is here on the efficiency of the entanglement transfer that can be achieved, rather than the achieved entanglement between the two memories.

2 Creation of a DLCZ heralded single photon source

In order to realize this experiment, we first need the capability to generate single photons. For that we use the Duan-Lukin-Cirac-Zoller (DLCZ) protocol that was first proposed in 2001 [Duan et al. 2001]. Initially, the proposal offered a novel way to distribute long-distance entanglement in a quantum network. Based on induced Raman transitions and phase-matching between the scattered photons, the idea lies in the heralding capability. Using this scheme, two-node entanglement has been experimentally realized by Kimble's group in 2007 [Chou et al. 2007] for a few microseconds. Since DLCZ produces single photons that are resonant with specific atomic transitions, it can be used as a single-photon source for devising atom-photon experiments in the single excitation regime. With this perspective in mind, we carried out a single-photon source based on the DLCZ protocol with the goal of demonstrating storage of single photons and entanglement.

2.1 Theoretical overview

2.1.1 Two-mode squeezed state

We model our atomic ensemble as $\mathcal{N}$ atoms all prepared in the ground state $|\bar{g}\rangle = |g_1,g_2,...,g_{\mathcal{N}}\rangle$ before the experiment. A weak write pulse, with detuning Δ relative to the $|g\rangle \rightarrow |e\rangle$ transition is sent to the atomic cloud, inducing with probability $\mathcal{P}$ a Raman transition to the state $|s\rangle$ for one atom and the emission of a field-1 photon. The atom-light state can be described by a two-mode squeezed state :

$$|\psi_{1,at}\rangle = \sqrt{1-\mathcal{P}} \sum_{n=1}^{\infty} \mathcal{P}^{n/2} \frac{\left(a_1^\dagger s_n^\dagger\right)^n}{n!} |0_1,\bar{g}\rangle \tag{4.1}$$

where $a_1^\dagger = \int a_{\mathbf{k}_1}^\dagger d\mathbf{k}_1$ is the creation operator for the field-1 photon and $s_i^\dagger$ is the operator that transfers the i-th atom in state $|s\rangle$. The detection of a field-1 photon in mode $\mathbf{k}_1$ projects the atomic ensemble into the collective state :

$$|\bar{s}\rangle = \frac{1}{\sqrt{\mathcal{N}}} \sum_{n=1}^{\mathcal{N}} |g_1,...,s_n,...,g_\mathcal{N}\rangle = \frac{1}{\sqrt{\mathcal{N}}} \sum_{n=1}^{\mathcal{N}} \hat{s_n}^\dagger |g_1,...,g_\mathcal{N}\rangle . \tag{4.2}$$

Upon detection of a field-1 photon in a specific $\mathbf{k}$ mode, a strong read pulse, resonant with the $|e\rangle \rightarrow |s\rangle$ transition, is sent after a short delay to the atomic ensemble. This pulse reads out the collective excitation by transferring back the atomic ensemble to state $|\bar{g}\rangle$ with the emission of a field-2 photon. Its wavevector $\mathbf{k}_2$ is defined by the phase matching condition $\mathbf{k}_2 = \mathbf{k}_W + \mathbf{k}_R - \mathbf{k}_1$ where $\mathbf{k}_{W,R}$ are the write (read) wavevectors. The state of the write/read photons can then also be written as a two-mode squeezed state :

$$|\psi_{1,2}\rangle = \sqrt{1-\mathcal{P}} \sum_{n=1}^{\infty} \mathcal{P}^{n/2} \frac{\left(a_{\mathbf{k}_1}^\dagger a_{\mathbf{k}_2}^\dagger\right)^n}{n!} |0_{\mathbf{k}_1},0_{\mathbf{k}_2}\rangle . \tag{4.3}$$

If we set $\mathcal{P} \ll 1$, we can discard high-order terms and write the state as

$$|\psi_{1,2}\rangle = \sqrt{1-\mathcal{P}} \left(|0_{\mathbf{k}_1},0_{\mathbf{k}_2}\rangle + \mathcal{P}^{1/2} |1_{\mathbf{k}_1},1_{\mathbf{k}_2}\rangle + \mathcal{P} |2_{\mathbf{k}_1},2_{\mathbf{k}_2}\rangle\right) . \tag{4.4}$$

We see that if a field-1 photon is detected, it mostly projects field-2 into a single-photon Fock state with a small multiphoton component. If the write and read beams are counter-propagating, field-2 will be emitted in the opposite direction to that of field-1 such that $\mathbf{k}_1 = -\mathbf{k}_2$. Experimentally, this makes the field-2 photon easy to collect in a fiber for later use.

2.1.2 Critical parameters

In a similar way to EIT-based memories, the optical depth of the atomic ensemble plays a crucial role in the DLCZ photon retrieval efficiency. The atomic ensemble is prepared in a collective state and then read out to emit a photon thanks to collective enhancement. With cold atoms, the main source of loss is coming from the so called spontaneous emission loss, described in [Duan et al. 2002]. The idea is that some detections of field-1 photons in the specific $\mathbf{k}_1$ do not herald the corresponding spin-wave mode and thus lead to inefficiencies after reading out. It is shown in this analysis that this probability is inversely proportionnal to the optical depth of the ensemble and that the signal-to-noise ratio in the field-2 detection, and thus the retrieval efficiency of the process, is directly proportional to the optical depth.

An experimental study of this effect can be found in [Simon et al. 2007] where the dependence of the retrieval efficiency is shown as a function of optical depth. In this case, the optical depth is virtually increased by putting the atomic ensemble inside an optical cavity. Interestingly, the authors also observe that if the optical depth becomes too high, the retrieval efficiency decreases. This effect is directly related to off-resonant excitations with neighbouring excited states, exactly like in the read out process of EIT-based memories.

At first glance, it seems rather easy to reach a high retrieval efficiency in DLCZ since all it requires is a high optical depth. However, it appears that the length L of the atomic

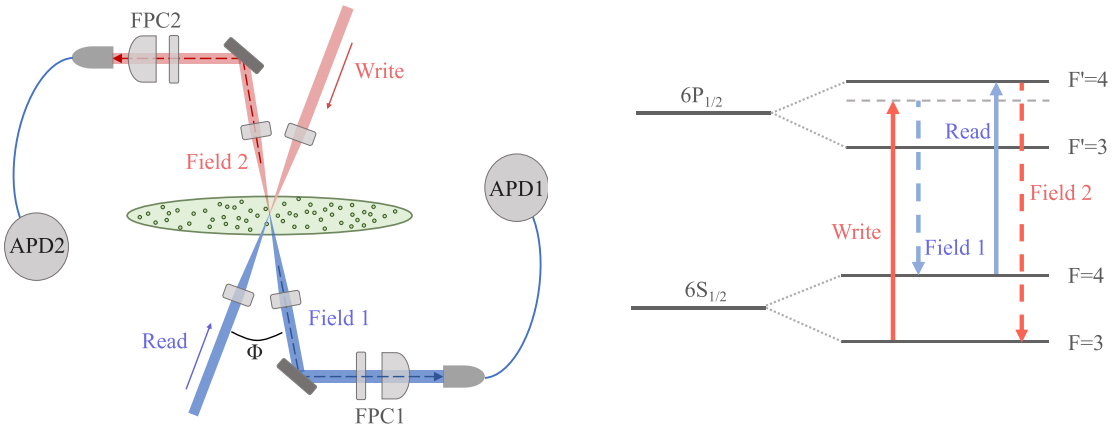

Fig. 4.3 *(left) : Scheme of the single photon source setup. Write and read beams have opposite* $\boldsymbol{k}$ *vectors such that field-1 and field-2 are collected in opposite directions. The angle* Φ *between* $\boldsymbol{k}_W$ *and* $\boldsymbol{k}_1$ *is 3°. Single photons are collected into avalanche photodetectors (APD1,2) after passing through Fabry-Perot cavities to filter out unwanted noise (FPC1,2). (right) : Frequencies of the involved fields. The experiment is performed on the D1-line in order to generate field-2 photons that are resonant with the* $|F = 3\rangle \rightarrow |F' = 4\rangle$ *transition.*

ensemble is also a critical parameter. After performing DLCZ in the longitudinal part of the MOT with high optical depth, the retrieval efficiency was near zero. In the transverse part, with less optical depth but smaller L, DLCZ was performing much better. This effect is explained in [Gorshkov, André, Fleischhauer, et al. 2007] and is due to the non-degeneracy of the $|g\rangle$ and $|s\rangle$ state. This non-degeneracy gives an additionnal momentum on the spin-wave $\Delta k = (\omega_s - \omega_g)/c$ and leads to a phase mismatch $\delta\chi = L\Delta k$ that depends on the length L of the ensemble [Surmacz et al. 2008]. This effect only happens in backward-retrieval schemes such as this DLCZ experiments but should not appear in forward retrieval schemes like the regular EIT storage performed in this thesis.

2.2 Experimental realization

We now describe our experimental implementation of this DLCZ single-photon source.

2.2.1 Setup

We prepared our DLCZ-based single photon source on the D_1 line of cesium. We choose $|g\rangle = \left|6S_{1/2}, F = 3\right\rangle$, $|e\rangle = \left|6P_{1/2}, F' = 4\right\rangle$ and $|s\rangle = \left|6S_{1/2}, F = 4\right\rangle$. The advantage of choosing such levels is to get a field-2 photon resonant with the $|F = 3\rangle \rightarrow |F' = 4\rangle$ transition. This transition has the highest transition strength in the D1 line, meaning the optical depth is the highest [Steck 1998]. The optical depth on the $|F = 3\rangle \rightarrow |F' = 4\rangle$ transition is three times higher than on the $|F = 3\rangle \rightarrow |F' = 3\rangle$ transition.

We send a weak write beam detuned by $\Delta = -10$ MHz to the $|g\rangle \rightarrow |e\rangle$ transition in order to induce the Raman scattering of a field-1 photon. Before detection, field-1 passes by a Fabry-Perot optical cavity (FPC1) in order to filter out the noise coming from the write

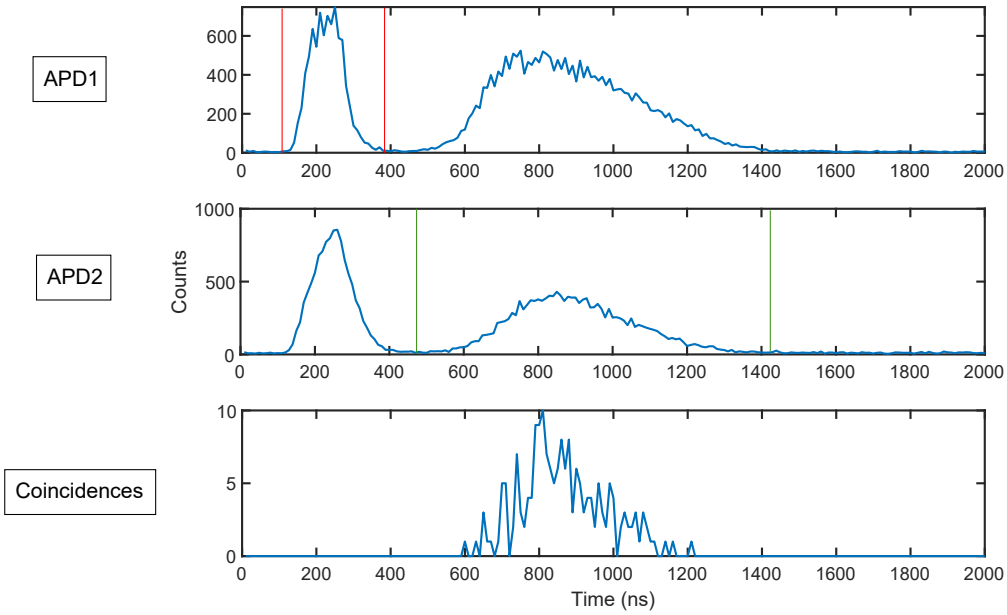

Fig. 4.4 *Typical detections results after DLCZ acquisition. This 2 μs experiment is repeated over many trials and histograms of the detections counts are build. The red and green lines indicates the detection windows where a consecutive detection triggers the creation of a coincidence event.*

beam, a necessary task to efficiently herald the excitation. The cavity is resonant on the $|s\rangle \rightarrow |e\rangle$ transition with a transmission of about 60% and a bandwith of 80 MHz. After a programmable delay - usually chosen to be less than a microsecond to achieve the best retrieval efficiency - we send a read beam with 3 mW of power to read out the excitation. We detect the field-2 photon in the opposite direction of field-1. To filter out the noise from the read beam, field-2 goes through a Fabry-Perot cavity (FPC2) resonant with the $|g\rangle \rightarrow |e\rangle$ transition. The photons are detected by avalanche photodiodes (APD1,2). The angle Φ between $\mathbf{k}_W$ and $\mathbf{k}_1$ is chosen to be around 3°. The optical depth in the single photon's path is measured to be 7.

In order to optimize the phase-matching conditions such that $\mathbf{k}_W = -\mathbf{k}_R$ and $\mathbf{k}_1 = -\mathbf{k}_2$, we carefully mode-match two optical paths between fiber couplers. The first path that serves as a collector for the single photons is focused inside the MOT with a 150 μm waist such that both photons are detected with the same solid angle. The read and write beam are also mode-matched and cross the MOT at the same position than the first path, with a waist of 500 μm. For both optical paths, the coupling between one mode and the other is greater than 95%.

2.2.2 Detection results

A typical detection result of the DLCZ protocol is represented on Fig. 4.4. The experiment is executed 250 times per MOT cycle and the data is acquired for several MOT cycles. Each

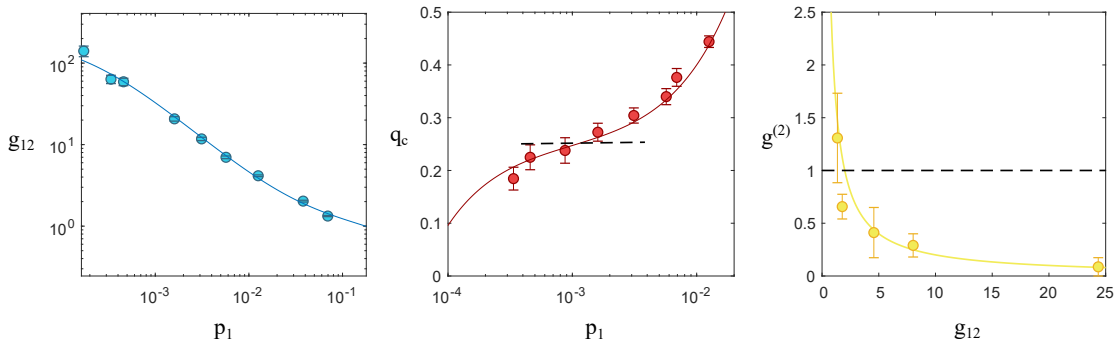

Fig. 4.5 *Characteristics of our single photon source. (left) : Cross-correlation function as a function of excitation probability. Strong non-classical correlations are observed. (middle) : Retrieval efficiency as a function of excitation probability. The single excitation regime corresponds to a detection probability of* $\sim 25\%$*. (right) : Antibunching parameter as a function of the cross-correlation function. The solid-line represents the behavior of* $g_2 = 4/g_{12}$*, expected for a two-mode squeezed state. The functions used to fit the behavior of* g_{12} *and* q_c *with* p_1 *are derived from a theoretical model described in [Corzo et al. 2019] which describes the output state as a two-mode squeezed state with a contribution of coherent and incoherent background noise. In this figure, there was no temporal shaping applied to the read beam.*

trial lasts 2 μs and the detection time bin is 10 ns. As the write beam is sent to the ensemble, APD1 records the possible arrival of a field-1 photon (here between 150 ns and 400 ns). The probability to detect one event in APD1 is noted p_1. Starting at 500 ns, the read beam is sent to the ensemble and APD2 records the arrival of field-2 photons (during 500 ns and 1400 ns). If both APDs record a detection event during these time windows (represented in red and green in Fig. 4.4), a coincidence event is registered at the arrival time of the field-2 photon.

Background noise coming from the write and read beams is expected during detection. The use of Fabry-Perot cavities allow filtering of the read beam by 30dB. For a read beam operating at 3 mW of power, this gives a background detection probability of the order of 10^{-5} for a 500 ns time window. The dark-count rate is at 50 Hz on our APDs, about the same order of magnitude than the background detection probability. These numbers allow us to get a good signal to noise ratio when operating at a low excitation probability p_1, usually chosen to be around 10^{-3}.

From these data, we can extract the excitation probability p_1, the probability of detection p_2 in APD2, and the conditional probability p_c to retrieve a field-2 photon upon prior detection of a field-1. These numbers are enough to make a full caracterisation of our photon-source and show non classical correlations between field-1 and field-2 photons.

2.2.3 Caracterization of our single photon source

Cross-correlation function In order to characterize our single photon source, we first measure the normalized cross-correlation function $g_{12} = \frac{p_{12}}{p_1 p_2}$ of field-1 and field-2 photons. Non-classical correlations are expected when this value exceeds the classical bound of $g_{12} = 2$ [Laurat et al. 2006]. Fig. 4.5 displays the cross correlation function as a function of the excitation probability p_1. We observe values of g_{12} greater than 100, attesting the strong non-classical behaviour of the correlations for the field-1 and field-2 photons. Due to higher multiphoton components, the quantity g_{12} decreases when the excitation probability p_1 increases

Retrieval efficiency Another critical parameter of our single photon source is the retrieval efficiency q_c. It accounts for the success of the reading process given a heralded collective excitation. Starting with the conditional probability p_c, we can correct this probability by the losses induced in the optical path to get the instrinsic retrieval efficiency q_c of the process. By varying p_1 we observe three regimes for the retrieval efficiency (see Fig. 4.5). When the excitation probability is large, the multiphoton component of eq. 4.4 is not negligible anymore and the retrieval efficiency thereby artificially increases. In the low-excitation regime, p_1 is of the same order of magnitude as the background noise which induces false heralding events, thereby decreasing the retrieval efficiency. Inbetween, we observe that q_c reaches a plateau, corresponding to the single-excitation regime where retrieval effiencies of $\sim 25\%$ are obtained. We also observed that the retrieval efficiency is optimized by maximizing the read beam power, varying in a linear fashion before reaching a plateau around 3 mW.

Antibunching of field-2 To measure the purity of our field-2 photon, we use a Hanbury Brown–Twiss setup with a 50:50 beamsplitter and two photodetectors to measure the anti-bunching parameter

$$g^{(2)} = \frac{\langle a_1^\dagger a_{2a}^\dagger a_{2b}^\dagger a_{2b} a_{2a} a_1 \rangle \langle a_1^\dagger a_1 \rangle}{\langle a_1^\dagger a_{2a}^\dagger a_{2a} a_1 \rangle \langle a_1^\dagger a_{2b}^\dagger a_{2b} a_1 \rangle} = \frac{p_1 p_{1,2a,2b}}{p_{1,2a} p_{1,2b}} \tag{4.5}$$

where $p_{1,2a}(p_{1,2b})$ accounts for a joint detection of APD 1 and APD 2a(2b), where the subscript a(b) denotes for the photodetectors placed after the beamsplitter in the HBT setup. We write $p_{1,2a,2b}$ as the probability for a three-fold coincidence detection on the three APDs. The smallest value we obtain is $g^{(2)} \sim 0.1$, a value well below the classical threshold of 1 for a coherent state. We also confirm the scaling of $g^{(2)} = 4/g_{12}$ as expected for a two-mode squeezed state (see Fig. 4.5).

2.3 Temporal mode shaping

In EIT-based memories, the bandwidth and the temporal mode of the stored photon is a critical parameter when optimizing the efficiency. Thankfully, these aspects can be partially controlled with DLCZ by temporally shaping the read beam as it is shown in [Farrera et al. 2016].

To shape the read beam, we mix the signal of the VCO that drives the AOM with a Gaussian voltage function. Experimentally, we observe that the field-2 pulse duration evolves linearly with the read pulse duration. Furthermore, the temporal shape of the field-2

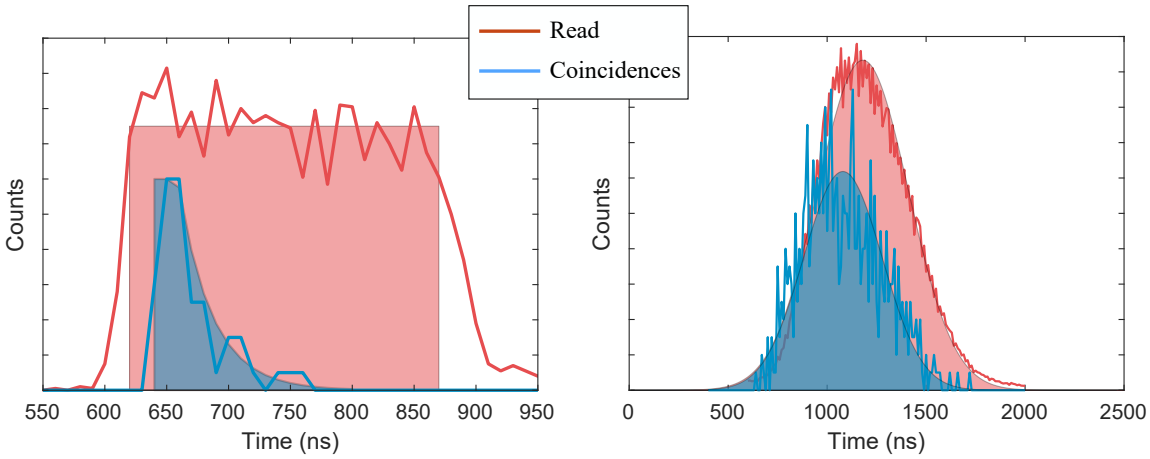

Fig. 4.6 *Single-photon mode shaping. (left) : When the read beam is a square pulse with high power, the read-out is saturated and the emitted photon has a decreasing exponential shape (blue). (right) : Generation of a 500 ns Gaussian shaped single photon. The read beam has a 600 ns Gaussian shape and a low-enough power such that the read out is not saturated. In both figures the read counts have been scaled down to fit the size of the coincidences counts.*

mode can be tuned by sending a specific temporal shape for the read beam. For example, a Gaussian field-2 is created by reading the collective excitation with a temporally Gaussian read beam. Nevertheless, we observed that in order to preserve the shape of the field-2 single photon, it is important to limit the power of the read beam. As represented in Fig 4.6, if the read beam has a too large power (square pulse here) it saturates the read-out and the shape transforms into a decreasing exponential. This is also the case when we aim to shape a field-2 photon as a Gaussian ; if the power is too high in the Gaussian read beam, the single photon will not acquire the desired Gaussian-shape. Even though this is not observed in the aforementioned paper, we also observed in our case that the retrieval efficiency after proper shaping was lower due to this effect (around 10%).

2.4 Discussion

Our heralded single photon source now has the right properties to make an EIT quantum storage experiment. We have the ability to generate 500 ns Gaussian shaped single photons with 10% retrieval efficiency at an excitation probability of $p_1 = 10^{-3}$, ensuring an anti-bunching parameter of $g^{(2)} = 0.1$. This low retrieval efficiency is mainly due to low optical depth and reduced power of the read beam in order to preserve a good shape for the single photon.

3 Experimental procedure

In this section we discuss our implementation for the experiment and optimization of memory efficiency.

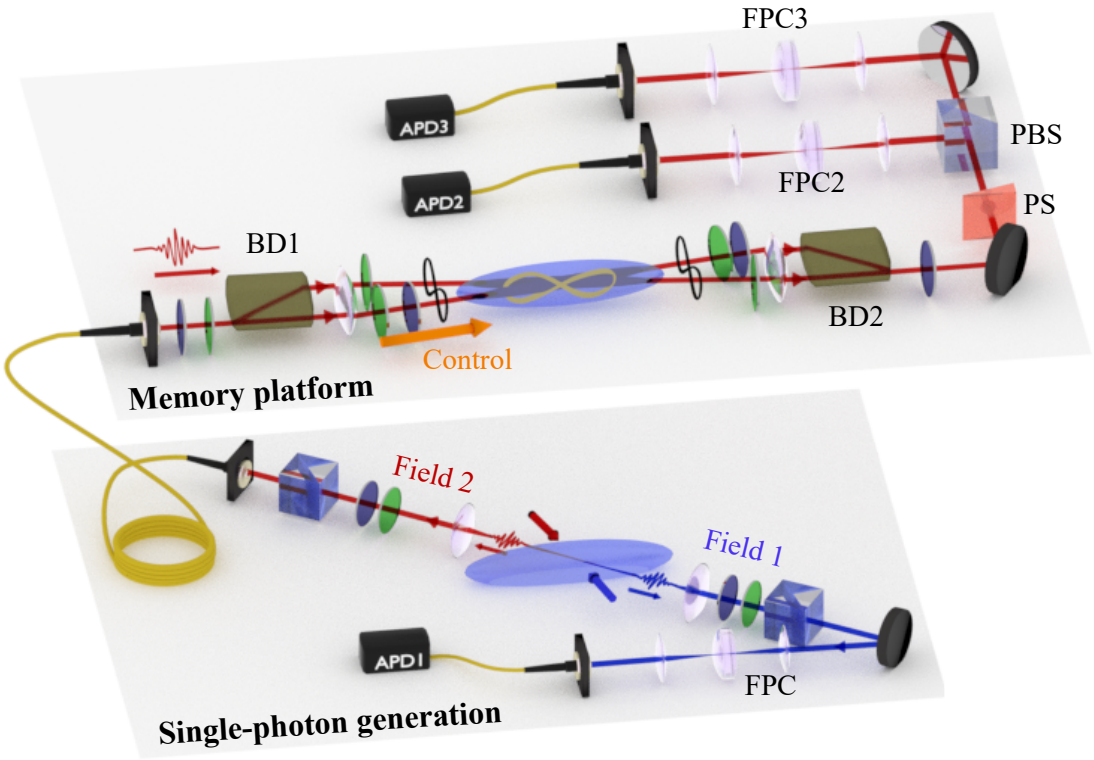

Fig. 4.7 *A 2.5-cm-long ensemble is prepared in a compressed MOT, with an OD up to 500. At first, a single photon is generated using the DLCZ protocol in a small transverse part of the ensemble. After sending a write pulse, the detection of a Field-1 photon, with a probability p_1, heralds the creation of a single collective excitation. A read pulse produces then a Field-2 single photon that propagates in a 1-μs fibered delay line and impinges on a beam displacer (BD). The resulting single-photon entanglement is mapped into and out-of two memory ensembles via EIT, with a control propagating at 1° angle. Entanglement is finally characterized using a phase shifter (PS), a polarizing beamsplitter (PBS) and two APDs. Before detection, Fabry-Perot cavities (FPC) filter the control background.*

3.1 Experimental setup

As hinted above, the experiment consists of two stages operated with the same ensemble of cesium atoms. A 2.5 cm-long atomic ensemble is prepared in a compressed MOT with an optical depth up to 500. The first stage consists in the generation of a heralded single photon using the DLCZ protocol as described in the previous section. A weak write pulse, detuned by $\Delta = -15$ MHz from the $\left|6S_{1/2},F=3\right\rangle \rightarrow \left|6P_{1/2},F'=4\right\rangle$ induces with probability p_1 the detection of a field-1 photon on APD1. We then read out the excitation to create a field-2 photon that will be used in the second stage. This photon is collected in a fibered delay-line of 1 μs duration (200 m length) before being sent on a birefringent beam displacer (BD1) with a polarization at 45° to the axis, generating in the ideal case the single photon entangled state of Eq. 4.1. Thanks to the use of a control beam resonant with the $\left|6S_{1/2},F=4\right\rangle \rightarrow \left|6P_{1/2},F'=4\right\rangle$ transition, the two modes are stored in parallel using dynamical EIT storage with the two paths crossing in the middle of the atomic ensemble. During propagation, the control is turned off for a programmable delay and is turned on again to map back the state to its photonic form. The two modes of the output state $|\Psi_{out}\rangle$ are recombined on a second beam-displacer (BD2) and the state is finally sent to a detection platform for the reconstruction of the reduced density matrix of the state. A phase-shifter (PS) varies the phase between the two modes and the state is measured on the $\{|H\rangle, |V\rangle\}$ basis by APD2 and APD3. Unwanted background noise coming from the control and read beam is filtered in frequency thanks to a set of Fabry-Perot cavities (FPC2 and FPC3) whose properties have been described in 4.3.1.

3.2 Experimental timings

We perform this experiment using a compressed MOT followed by polarization gradient cooling of our atoms (see Fig. 3.3). Two milliseconds after the B-field is turned off, we start the experiment in a repetitive fashion, each trial containing two stages. The first one is the generation of a heralded single photon, and the second one is the storage of entanglement. Only one atomic-ensemble is used for the whole experiment. In order to give the time for field-2 to fully leave the ensemble after its generation, and before storing it, we send the photon to a 200-m-long fibered delay line (Thorlabs SM800-5.6-125) introducing a delay of 1 μs. Meanwhile, a repump pulse resonant with cesium $\left|6S_{1/2},F=4\right\rangle \rightarrow \left|6P_{1/2},F'=4\right\rangle$ transition is sent to the atomic cloud to prepare all the atoms back to the ground state $\left|6S_{1/2},F=3\right\rangle$, in case the excitation has not be fully read out. After the optical delay, we start the storage experiment where we perform either single-mode storage or entanglement storage. When the single-mode (or entangled) field-2 photon propagates through the ensemble, the control field is switched on and off adiabatically, which coherently transforms the entangled photons to an entangled collective atomic excitation within our atomic could. After a storage time of 1 μs, the control is switched on again to read the collective excitation back into our entangled photonic modes. In total, each subsequence has a duration of 4 μs and 250 trials are performed during each cycles, for a total experiment duration of 2 ms per MOT.

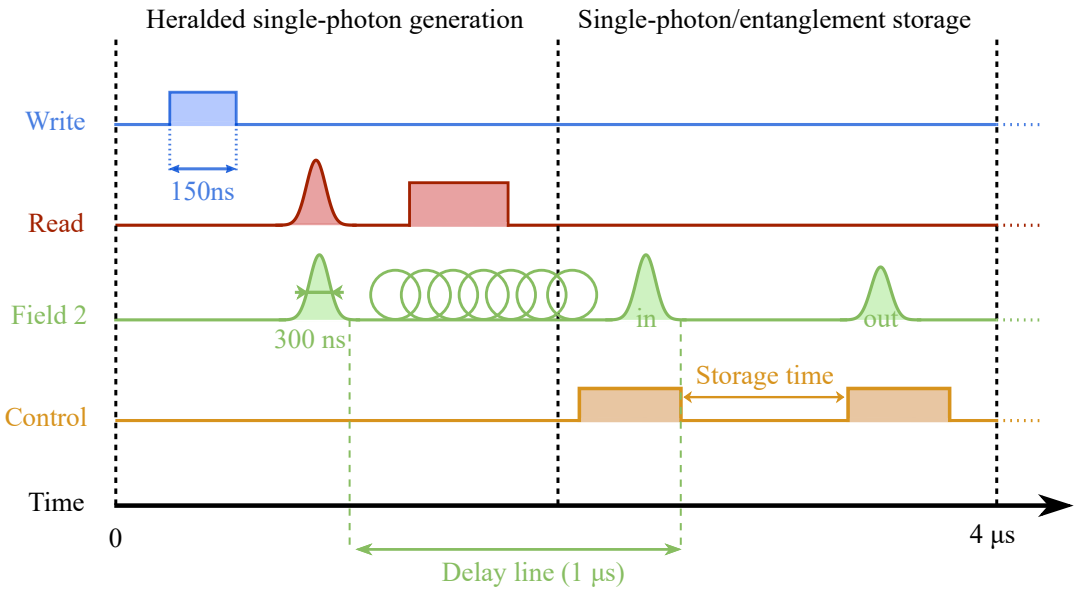

Fig. 4.8 *Timing of the experimental sub-sequence procedure. Each subsequence lasts 4 µs and is repeated 250 times per MOT cycles. Two stages are performed in these 4 µs. The first one consists in the generation of heralded single photon via DLCZ and the second one consists in the storage of this photon.*

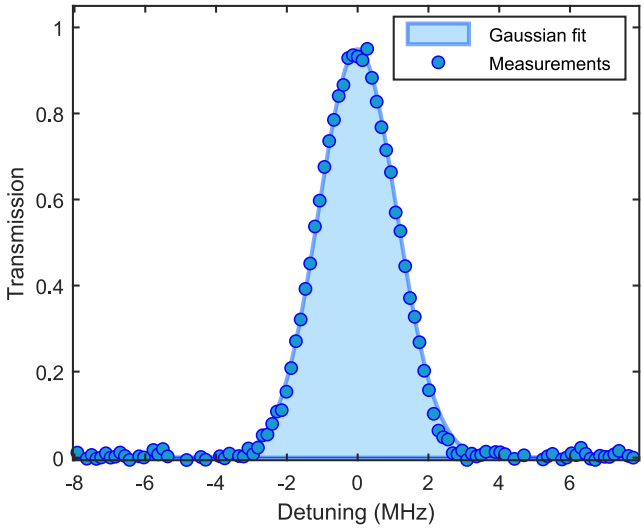

Fig. 4.9 *Typical EIT spectrum for memory experiments, zoomed in from the high-OD absorption line.*

4 Single-mode storage

Before performing the entanglement mapping experiment, we realize a single-mode storage experiment by using one path of the interferometer in order to optimize the efficiency of the memory and certify the preservation of the single-photon caracter through the mapping. In this section, we detail our efficiency optimization procedure and present the results of single-photon storage with $(87 \pm 5)\%$ efficiency, the highest efficiency ever achieved for a single-photon quantum memory regardless of the platform considered. Similar results were published by [Wang et al. 2019] at the time we were collecting the data for an efficient single-mode storage.

4.1 Efficiency optimization

The first task to realize an efficient memory is to optimize the optical depth. Following the techniques discussed in chapter 2, we managed to reach an OD of approximatively 500 for the $|g\rangle \rightarrow |e\rangle$ transition. We then optimize the critical parameters defined in Sec. 5 of Chapter 2.

Pulse length

Once a large enough OD (superior than 400) has been achieved (see Fig. 3.6), we need to optimize the memory itself by optimizing the power of the control field and the bandwidth of the single photon (see 5.2). We choose to work with a Gaussian shaped photon with an envelope $A_t(t)$ equal to

$$A_t(t) = \frac{1}{\sqrt{2\pi}\sigma_t} exp\left[-\left(\frac{t}{\sqrt{2}\sigma_t}\right)^2\right] \tag{4.6}$$

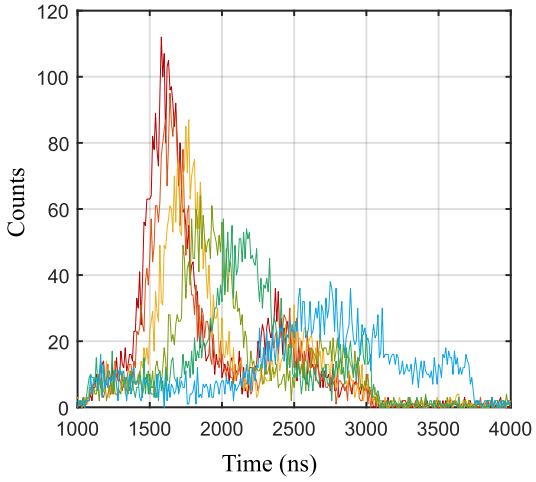

Fig. 4.10 *Single photon slow-light through the atomic ensemble in single-mode configuration. Traces are detection couts on APD2. Each color represents a specific power for the control field (red: 3.4 mW, orange: 3 mW, yellow: 2.5 mW, light green: 2 mW, dark green: 1.5 mW, blue: 1 mW). We observe the augmentation of slow-light delay with the decrease of power of the control field, accompanied by time distorsion due to frequency absorption.*

with $\sigma_t = 175$ ns for a 350 ns full width at half maximum (FWHM) photon. Its frequency counterpart is given by the Fourier transform of A_t

$$A_\omega(\omega) = \int e^{-2\pi i\omega t} A_t(t)dt = \frac{1}{\sqrt{2\pi}\sigma_\omega} exp\left[-\left(\frac{\omega}{\sqrt{2}\sigma_\omega}\right)^2\right] \tag{4.7}$$

with $\sigma_\omega = 1/(2\pi\sigma_t) = 0.9$ MHz. Here, the frequency envelope is also a Gaussian with standard deviation σ_ω. The goal in the optimization is now to obtain an EIT window with a half width at half maximum (HWHM) of the same order of magnitude but higher than σ_ω. By changing the power of the control beam, it is easy to modify the width of the EIT-window. In fig. 4.9 we show one typical EIT-spectrum for high efficiency storage.

Pulse delay

The storage can be optimized only if the pulse is well contained in the atomic ensemble when the control beam is turned off. This is also controlled by the EIT bandwidth σ_{EIT} since it influences the group velocity of light in the medium (see Sec. 5 of Chapter 2). For a narrower EIT-window we obtain a larger reduction of group velocity and an increased slow-light delay which better compresses the pulse in the ensemble. In Fig. 4.10 we show the results for delayed propagation of single photons through the atomic ensemble where we observe that the delay increases when the control power diminishes. We also notice that the pulses get distorted when σ_{EIT} get narrower, this is the effect of the absorption of side frequencies that makes the pulse thinner in frequency space, inducing its expansion in time. Note that the noise of the control beam that we observe on this figure is reduced when looking at

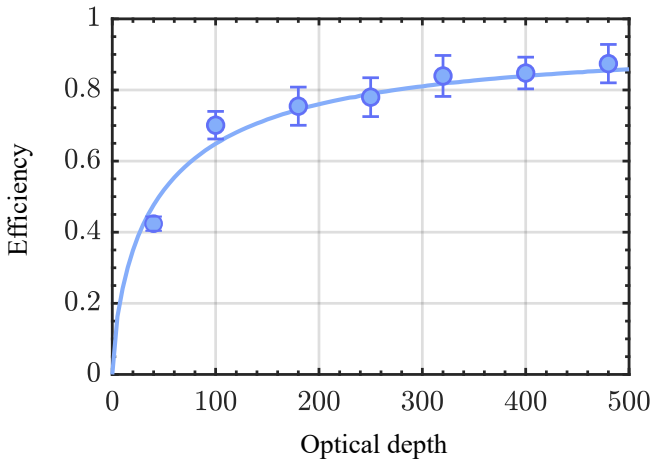

Fig. 4.11 *Single photon storage-and-retrieval efficiency as a function of optical depth. Blue dots represent the data while the solid line is the theoretical prediction based on Maxwell-Bloch equations. The best value of efficiency reaches (87 ± 5)% and is the maximal achievable value at this optical depth on the D_1 line of cesium.*

the coincidence counts thanks to the heralding process. After optimization, we choose to perform the experiment with a 2-pulse delay, as plotted in green in fig. 4.12.

4.2 High efficiency results

After full optimization, we measured the single photon storage-and-retrieval efficiency as a function of the optical depth in one arm of the interferometer. Similar results are obtained for both memories. The efficiencies are compared to a full model based on Maxwell–Bloch equations, which takes into account the interaction of the signal and control with all the Zeeman and excited levels. For this model, we consider an intrinsic ground state decoherence rate $\gamma_0 = 10^{-3}\Gamma$, as extracted from EIT spectra measurement, where $\Gamma/2\pi = 4.56$ MHz is the decay rate for the D1 line. The data agree well with this model and the maximal achieved efficiency reaches (87 ± 5)% for an OD of about 500. A typical histogram plot is shown in Fig. 4.12.

4.3 Preservation of the single-excitation

To characterize the retrieved single photon, we measure the suppression of the two-photon component relative to a coherent state via a Hanbury Brown-Twiss (HBT) setup. In a similar way than in Section 2.2.3, we measure this parameter defined as :

$$g^{(2)} = \frac{p_1 p_{1,2a,2b}}{p_{1,2a} p_{1,2b}} \tag{4.8}$$

In the same way, APD2 is replaced by a fibered beam-splitter and each port is connected to an APD (APD2a and APD2b). We record three-fold coincidences between the three involved APDs, with probability $p_{1,2a,2b}$. We perform this experiment with and without storage for

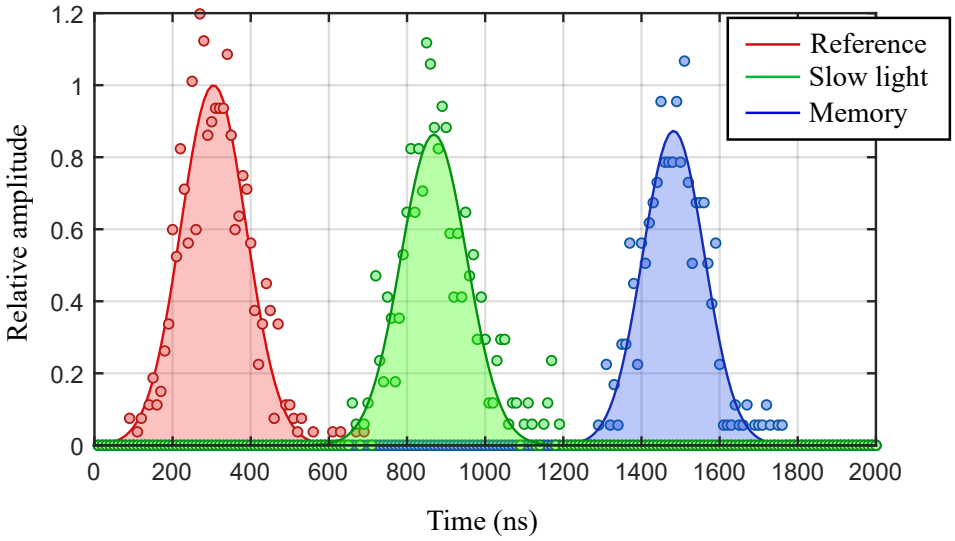

Fig. 4.12 *Typical results of normalized coincidence counts for reference, slow-light and memory heralded single photon waveform. Solid lines are Gaussian fit to the data.*

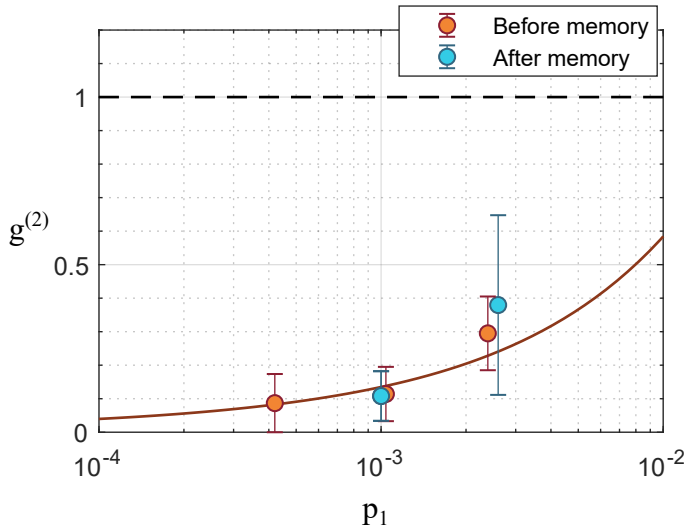

Fig. 4.13 *Antibunching measurement before and after the storage process, as a function of excitation probability. The error bars come from Poissonian uncertainties of the detection. The large error bars is due to the rarity of the three-fold detection probability. The solid line is the expected value before the memory for a two mode squeezed state.*

different excitation probabilities and we observe that the single photon character is well preserved during the storage.

During the next experiment where we store entanglement, we set $p_1 = 10^{-3}$ such that $g^{(2)} = 0.1$. Operating deeply in the single-excitation regime is a challenging task but is a stringent requirement for scalable quantum networks and their envisionned applications.

5 Entanglement mapping

5.1 Entanglement characterization

We now turn to the storage of entanglement and its characterization. For this purpose, we follow the model-independent determination introduced in [Chou et al. 2005] that consists in measuring a reduced density matrix $\tilde{\rho}$ by restricting oneself to the subspace with no more than one photon per mode and assuming that all off-diagonal elements between states with different numbers of photons are zero. This method provides a lower bound for the presence of entanglement in the state.

In the basis $|i_a,j_b\rangle$ with the number of photons $\{i,j\} = \{0,1\}$, $\tilde{\rho}$ can be written as

$$\tilde{\rho} = \frac{1}{P}\begin{pmatrix} p_{00} & 0 & 0 & 0 \\ 0 & p_{01} & d & 0 \\ 0 & d^* & p_{10} & 0 \\ 0 & 0 & 0 & p_{11} \end{pmatrix} \tag{4.9}$$

where $p_{i,j}$ corresponds to the probability to find i photon in mode a and j photon in mode b, $P = p_{00} + p_{01} + p_{10} + p_{11}$, and d is the coherence between the states $|0_a,1_b\rangle$ and $|1_a,0_b\rangle$. The coherence term is given by $d = V(p_{01} + p_{10})/2$ where V is the visibility of the interference fringe between mode a and b when their relative phase is scanned. The reduced density matrix enables to calculate the concurrence $\mathcal{C}$, i.e., a monotone measurement of entanglement, as

$$\mathcal{C} = \frac{1}{P}\max\left(2d - 2\sqrt{p_{00}p_{11}},0\right) \tag{4.10}$$

where $\mathcal{C}$ takes values between 0 for a separable state and 1 for a maximally entangled state. We estimate this lower bound of the concurrence of our state before and after the memory in order to calculate the entanglement transfer efficiency λ defined by

$$\lambda = \frac{\mathcal{C}_{out}}{\mathcal{C}_{in}}. \tag{4.11}$$

5.2 Calibration and probability measurements

To estimate the transfer of entanglement, we first need to characterize it before storage. We use the same atomic ensemble to generate the single photons and store them later on, so it is unfeasible to measure the entangled state by simply removing the atoms from the path. Since the storage happens a few microseconds after the heralded generation, there is no time to remove the MOT in between. To solve this problem, we send the single photon through another path which also contains an interferometer. As shown in Fig. 4.14, the two paths

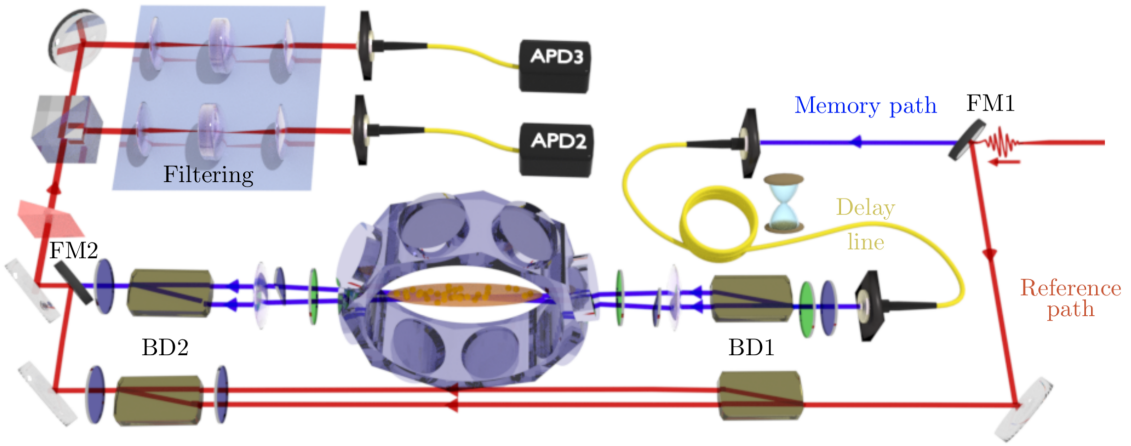

Fig. 4.14 *Experimental setup for calibration of the entanglement transfer measurement. Since the same atomic-ensemble is used for both generation and storage, it is not possible to remove the atoms to measure the reference entangelement. Two flip mirrors (FM1 and FM2) are used to deviate and recombine the path from the memory path. We want to measure the action of the memory on the transfer of entanglement from BD1 to BD2. To this end, we can correct on the ratio of channel losses induced by the two different paths.*

Table 4.1: Raw datas and probabilities directly calculated from the counts on APD21 and APD2.

	Ref	Δ	Memo	Δ
p_{01}	$4.57 \cdot 10^{-3}$	$1.2 \cdot 10^{-4}$	$2.51 \cdot 10^{-3}$	$0.6 \cdot 10^{-4}$
p_{10}	$4.95 \cdot 10^{-3}$	$1.2 \cdot 10^{-4}$	$2.71 \cdot 10^{-3}$	$0.6 \cdot 10^{-4}$
p_{11}	$2.58 \cdot 10^{-6}$	$1.8 \cdot 10^{-6}$	$7.35 \cdot 10^{-7}$	$5.20 \cdot 10^{-7}$
p_{00}	0.99	$2.4 \cdot 10^{-4}$	0.99	$1.9 \cdot 10^{-4}$
$\mathcal{C}$	$5.9 \cdot 10^{-3}$	$1.6 \cdot 10^{-3}$	$2.8 \cdot 10^{-3}$	$0.9 \cdot 10^{-3}$

Table 4.2: Corrected data, which effectively represents the transfer of entanglement through our memory as described in Section 5.2

	Ref	Δ	Memo	Δ
p_{01}	$4.57 \cdot 10^{-3}$	$1.2 \cdot 10^{-4}$	$3.87 \cdot 10^{-3}$	$0.9 \cdot 10^{-4}$
p_{10}	$4.95 \cdot 10^{-3}$	$1.2 \cdot 10^{-4}$	$4.18 \cdot 10^{-3}$	$0.9 \cdot 10^{-4}$
p_{11}	$2.58 \cdot 10^{-6}$	$1.8 \cdot 10^{-6}$	$1.35 \cdot 10^{-6}$	$9.55 \cdot 10^{-7}$
p_{00}	0.99	$2.4 \cdot 10^{-4}$	0.99	$1.9 \cdot 10^{-4}$
$\mathcal{C}$	$5.9 \cdot 10^{-3}$	$1.6 \cdot 10^{-3}$	$4.7 \cdot 10^{-3}$	$1.3 \cdot 10^{-3}$

have the same filtering and detection setup. However these two paths have different overall channel losses and we correct the raw probabilities in order to get the right transfer efficiency out of it.

When measuring the reference entanglement, we activate the flip-mirrors (FM1 and FM2) that will deviate the path of the single photon. For the memory path, FM1 and FM2 are not activated and the single photons propagate through the delay line and the vacuum chamber. Before each set of measurements, we measure the ratio $\mathcal{R}$ of transmission between the two interferometers when no atom is present along the memory path. The numerical value obtained is

$$\mathcal{R} = \frac{\eta_{ref}}{\eta_{mem}} = \frac{\eta_p^r}{\eta_p^m \eta_{dl}} = 1.54 \tag{4.12}$$

where $\eta_{dl} = 0.77$ is the transmission of the delay line (from FM1 to BD1), $\eta_p^m = 0.78$ is the transmission on memory path from BD1 to FM2 with no atoms along the path and $\eta_p^r = 0.93$ is the transmission from FM1 to FM2. Fiber-couplings and polarization stability through the delay line must be carefully checked before each set of measurement in order to set this parameter to the desired value.

Experimentally, upon the detection of a heralding photon on APD1, we first measure the $p_{i,j}$ probabilities of Eq. 4.9 with APD2 and APD3. The two detectors assess the presence of photons in mode a or b by monitoring the two outputs of a polarizing beam splitter placed after recombination of the two paths of the interferometer. When measuring the counting probabilities with APD2 and APD3 for the memory entanglement, we correct our data from this transmission ratio in order to account only for the effect of our quantum memory. We therefore multiply p_{01} and p_{10} by $\mathcal{R}$ from Eq. 4.12, and we correct p_{11} by $\left(\eta_p^r\right)^2 / \left(\left(\eta_p^m\right)^2 \eta_{dl}\right) = 1.84$ considering that each path of the interferometer contains one photon. Table 4.1 displays the raw data as they are derived from the APD counts and Table 4.2 shows the corrected probabilities.

5.3 Fringes

In order to measure the visibility between the two entangled modes, the next step is to measure interference fringes by mixing the two modes and scanning their relative phase φ. This can be done by using a set of two half-wave plates placed after BD2, with their axis parallel to the field polarizations and varying their relative angle. This allows to change the relative length between the two paths and observe fringes after splitting on a PBS. The experimental fringes are given in Fig. 4.15. The average raw visibilities are $V_{\text{in}} = 0.96 \pm 0.03$ and $V_{\text{out}} = 0.87 \pm 0.04$, derived from the sinusoïdal fit to the data. The decrease in visibility after storage is mainly due to a slight contamination by the control field. After correction of this background we measure a visibility $V_{\text{out}} = 0.94 \pm 0.03$.

5.4 Entanglement transfer results

The reconstructed density matrices $\tilde{\rho}_{\text{in}}$ and $\tilde{\rho}_{\text{out}}$ are given in Fig. 4.16. These data allow to characterize the performance of the entanglement transfer and other parameters.

The first crucial parameter is the suppression of the two-photon component. It can be evaluated here by the ratio $g^{(2)} = p_{11}/(p_{10} \cdot p_{01})$. This parameter amounts to

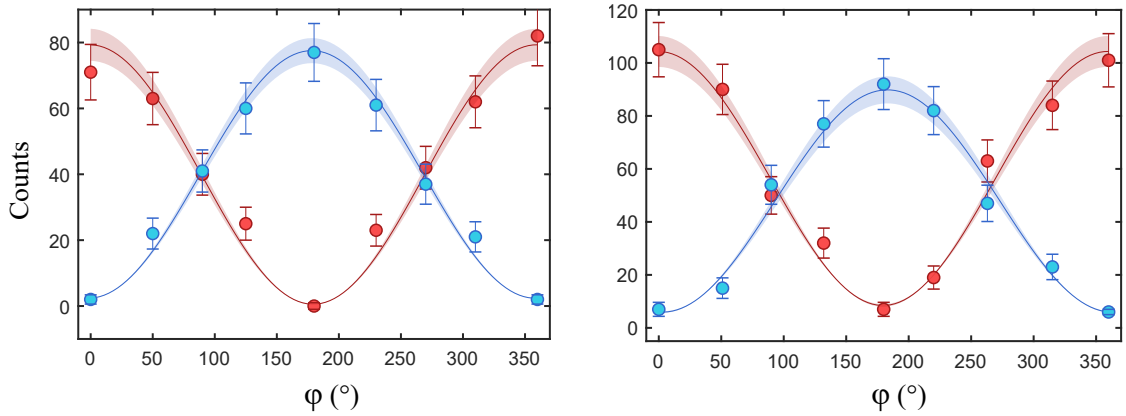

Fig. 4.15 *Experimental fringes between the two modes $|H\rangle$ and $|V\rangle$, respectively red and blue. The solid lines are sine fits to the data and the colored area represents the 1σ confidence interval of the fit. The error bars correspond to the propagated Poissonian error of the photon counting probabilities. (left): Fringes obtained without storage with visibility $V_{in} = 0.96 \pm 0.03$. (right): Fringes after storage with visibility $V_{in} = 0.87 \pm 0.04$ ($V_{out} = 0.94 \pm 0.03$ after background correction).*

$g^{(2)}_{\text{in}} = 0.11 \pm 0.07$ and $g^{(2)}_{\text{out}} = 0.08 \pm 0.06$ before and after storage respectively, thereby confirming the preservation of the single photon character, as in the single-mode storage.

Also, the overall storage-and-retrieval efficiency η is given by the ratio of the one-photon probabilities $(p_{10} + p_{01})_{\text{out}}/(p_{10} + p_{01})_{\text{in}}$. This ratio is equal to $\eta = (85 \pm 4)\%$, in agreement with the efficiencies measured for each memory operated independently. These values combined with the achieved visibilities confirm the efficient, noiseless and reversible coherent mapping.

From these data, one can estimate the concurrence of entanglement with the formula given in Eq. 4.10. Without correcting for losses, detection efficiencies and residual background noise, we obtain a value for the concurrence before storage of $\mathcal{C}_{\text{in}} = (5.9 \pm 1.2) \times 10^{-3}$ and a value after retrieval of $\mathcal{C}_{\text{out}} = (4.7 \pm 0.9) \times 10^{-3}$. We finally evaluate the entanglement transfer parameter λ. In our implementation, this parameter reaches $\lambda = (80 \pm 20)\%$. In the ideal case, this value is equal to the storage-and-retrieval efficiency of the involved memories. If the visibility of the fringes measured after retrieval is corrected from background noise, the output concurrence is increased to $\mathcal{C}_{\text{out}} = (5.3 \pm 0.9) \times 10^{-3}$ and the ratio λ to $88^{+12}_{-23}\%$. These numbers represent more than a 3-fold increase in transfer efficiency relative to previous works.

The high value of the error bar on λ is mainly due to the uncertainty present on the values of p_{11}. This parameter is known to be difficult to measure as it corresponds to events for which the occurrence decreases rapidly with the suppression of the two-photon component [Choi et al. 2008]. 180 hours of data taking were necessary to specifically access these probabilities and few coincidences were obtained. Indirect methods could be used to assess entanglement but would require specific assumptions about the initial state and noise statistics [Usmani et al. 2012] or performing homodyne measurements [Morin et al. 2013]. In the broad context of quantum networks, this result also emphasizes the topical importance

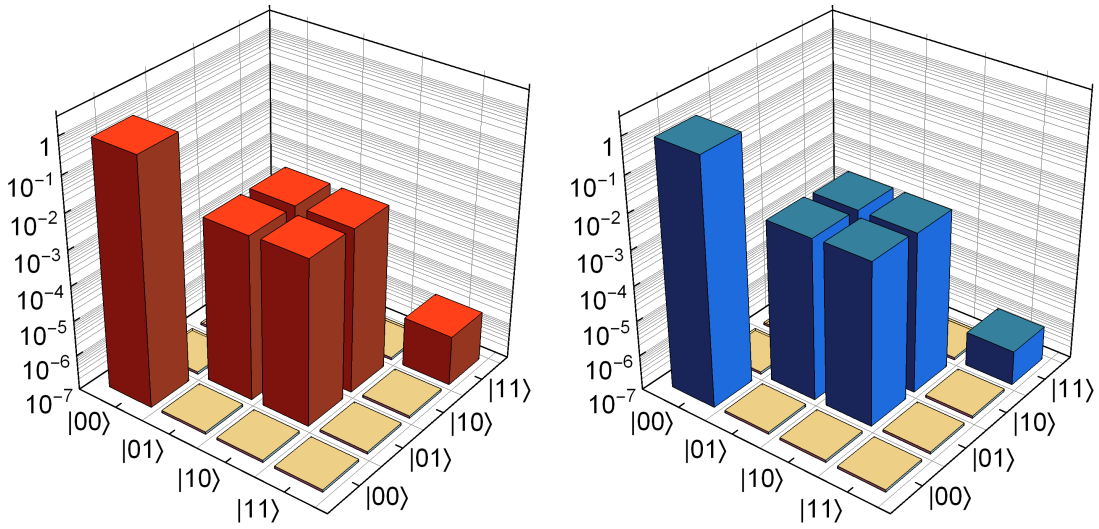

Fig. 4.16 *Reconstructed reduced density matrix of the entangled state $\tilde{\rho}_{in}$ before (red) and $\tilde{\rho}_{out}$ after (blue) the memory. The concurrence derived from these density matrices provides a lower bound for the concurrence of these states.*

of developing efficient benchmarking tools [Eisert et al. 2020].

For completeness, we give here the typical experimental rates. During the 1 ms phase when generation and storage are performed, the heralding rate to generate the single photon is of about 25 per second, and the rate of entanglement generation is reduced to 18 per second due to couplings and loss in the delay line. After storage and retrieval, propagation and filtering (30% transmission), and detection (50% efficiency), the single photon detection rate is about 1.7 per second. Given the specific duty cycle of 1/50 in our implementation, the overall entanglement generation rate and single photon detection rate are about 0.3 and 0.03 per second, respectively.

6 Conclusion

In this chapter we have reported the realization of mapping of heralded entanglement into and out of two quantum memories with high efficiency. We have first described the implementation of a single photon source based on the DLCZ scheme and reported the generation of single-photons with low two-photon contribution and tunable temporal shape. We then reported the single-mode storage of a single photon with a storage-and-retrieval efficiency of $\eta = 87\%$. Finally we detailed the experimental process of entanglement mapping and show that we have obtained an entanglement transfer parameter of $\lambda = (80 \pm 20)\%$ without any correction. The demonstrated capability is an important step toward the development of scalable networking architectures.

A central challenge remains to demonstrate a quantum link efficiency greater than unity, i.e., a preparation rate of entangled memories much larger than the decoherence rate, a cornerstone yet to be demonstrated in a cold atom setting. This kind of experiment could therefore be improved if the same entanglement transfer efficiency could be maintained for increased storage time in the memories.

Conclusion

Summary

In this thesis, we have demonstrated an efficient mapping of single-photon entanglement into and out of entangled spin-waves, with an overall entanglement transfer of $\lambda = (80 \pm 20)\%$ without background correction. We have also demonstrated the storage of single photons, with an efficiency of $\eta = (87 \pm 5)\%$. This is the maximal achievable value at this optical depth, and it is also the highest efficiency ever achieved for single-photon storage in a quantum memory regardless of the platform considered.

To that end, we first motivated our work in the context of quantum networks research. We have seen that quantum memories are essential components for the development of the envisionned quantum repeater, a device that allows the generation of long distance entanglement. In this prospect, we have seen that the efficiency of quantum memories, alongside other parameters such as lifetime and multimode capacity, is a crucial parameter in the performance of quantum repeaters. We then theoretically described the storage process in cold atomic ensembles and detailed the requirements for efficient storage. There are several requirements that need to be fulfilled, but the two crucial ingredients required are first the high optical depth of the atomic ensemble and second to perform the memory on the D_1-line. As explained in Chapter 2, the efficiency can be limited by off-resonant effects with neighbouring excited states. We noted that this effect is less prominent on the D_1-line as compared with the D_2-line, which eventually led us to modify the setup accordingly since simulations predicted that a 90% efficiency would be achievable on the D_1-line. Chapter 3 focused on the preparation of atomic ensembles to make them suitable for highly efficient memory experiments, especially on how to optimize the optical depth. Alongside the presentation of several techniques to characterize our atomic ensemble, we also discussed two main approaches to boost the optical depth of our MOT, namely a temporal dark MOT and a PG-cooled MOT implementation. We discussed both advantages and disadvantages of these approaches and explained why we sticked to the PG-cooled MOT for memory experiments. We finished this Chapter by giving details on the experimental apparatus and the setup. In Chapter 4, we described the entanglement mapping experiment in a chronological fashion. First, the creation of a heralded single photon source suitable for memory experiments was presented. Then, we described an efficient single photon storage with an efficiency of $\eta = (87 \pm 5)\%$ and we extended this result by demonstrating the efficient mapping of single photon entanglement into and out of quantum memories with a transfer efficiency of $\lambda = (80 \pm 20)\%$.

Within the scope of scalable quantum networks, this work paves the way towards a fully fledged quantum repeater for quantum internet applications. It promises the efficient read

out of memories in repeater protocols, where entanglement needs to be mapped out of the memories in order to perform swapping operations. This work also represents a milestone in the research of the QIA consortium. While it was necessary to reach this capability, other requirements still need to be fulfilled to achieve functional quantum networks. Not only long memory times, high efficiencies and high multimode capacity are required, but we need the ability to combine these assets. Even though we witnessed a lot of development in this direction over the recent years, this still remains a challenge for the community. On the other hand, quantum memories also need to be interfaced with other devices such as single photon sources or efficient Bell-state measurement platforms, which are also crucial elements for the functionality of quantum repeaters. These aspects are currently investigated in our lab and constitute the perspectives of this work.

Perspectives

In the path of these results, several extensions are considered to improve the key parameters and use the system in protocols.

Multiplexing with spatial modes Up to now, high multiplexing capabilities in atomic ensembles have been limited to small optical depth memory cells which limit the efficiency of these protocols. Combining high efficiency and high multimode capacity in quantum memories consitute an essential milestone that needs to be achieved. We are thus working in LKB towards the development of a multiplexed memory with high efficiency. The idea is to use Hermite-Gaussian modes of light, that are orthogonal, in order to store multiple excitations in parallel into our atomic cloud. Using phase plates and mirrors, it is possible to map the light of 15 single-mode fibers to a single "beam" containing 15 different Hermite-Gaussian modes. These modes will then be sent in the atomic ensemble, creating orthogonal spin-waves thus preserving the properties of each mode. Eventually, a similar technique can be employed to demultiplex the spatial modes in order to characterize the operation. From this, a few experiments are envisionned including quantum storage of 15 modes, the storage of 7 qubits in parallel and improved generation of single photons with DLCZ.

Lifetime improvement An important parameter to optimize in our setup is the lifetime of our memory. Several directions can be investigated in order to push this capability. Optical pumping in a magnetic insensitive Zeeman state is a possible candidate. It would also be possible to optically pump in an edge state as presented in Chapter 3 and then use our dynamical bias field to cancel the magnetic field during the small experiment window, increasing both the optical depth and the lifetime. Nevertheless, the temperature of the ensemble quickly becomes a limitation and it is generally required to go to dipole traps or a lattice configuration to reach the tens of millisecond scale. However, specific configurations will need to be used to preserve a large transverse size.

Quantum money Many applications are expected to emerge from the creation of the quantum internet. The quantum properties of such a network offers a lot of advantages for cryptographic protocols. An application proposed recently [Bozzio et al. 2018; Bozzio et al. 2019] is to use quantum memories to perform a protocol known as "quantum money". The

idea is to perform a transaction with a "quantum credit card" which is protected against attempts of hacking or fraud. This protocol could be feasible only if the memory, considered as the credit card, is highly efficient. If this requirement is not fullfilled, the credit card would not be secured. This experiment is undergoing in our lab and preliminary results have already been obtained. It will be the first time that a quantum memory and a cryptography protocol are combined together.

Towards a repeater segment A mid-term goal is to extend this work in order to build a basic link of a quantum repeater. This implementation would rely on multimode EIT-quantum memories using spatial modes and frequency non-degenerate photon pair sources. The quantum repeater link will be based on two parallel chains of telecom-heralded entangled quantum memories. To this end, our group is working on these type of non-degenerate sources that can produce photons at both the D_1-line and telecom frequencies. This way, entanglement on the Fock basis will be heralded and the double chain will be able to deliver polarization entanglement after a swapping operation.

Bibliography

A

Abi-Salloum, Tony Y. (May 19, 2010). "Electromagnetically induced transparency and Autler-Townes splitting: Two similar but distinct phenomena in two categories of three-level atomic systems". *Physical Review A* **81**.5, p. 053836. DOI: 10.1103/PhysRevA.81.053836.

Afzelius, Mikael and Christoph Simon (Aug. 11, 2010). "Impedance-matched cavity quantum memory". *Physical Review A* **82**.2, p. 022310. DOI: 10.1103/PhysRevA.82.022310.

Afzelius, Mikael, Christoph Simon, Hugues de Riedmatten, and Nicolas Gisin (May 21, 2009). "Multimode quantum memory based on atomic frequency combs". *Physical Review A* **79**.5, p. 052329. DOI: 10.1103/PhysRevA.79.052329.

Afzelius, Mikael et al. (Jan. 27, 2010). "Demonstration of Atomic Frequency Comb Memory for Light with Spin-Wave Storage". *Physical Review Letters* **104**.4, p. 040503. DOI: 10.1103/PhysRevLett.104.040503.

Alexander, A. L., J. J. Longdell, M. J. Sellars, and N. B. Manson (Feb. 1, 2006). "Photon Echoes Produced by Switching Electric Fields". *Physical Review Letters* **96**.4, p. 043602. DOI: 10.1103/PhysRevLett.96.043602.

Anisimov, Petr M., Jonathan P. Dowling, and Barry C. Sanders (Oct. 12, 2011). "Objectively Discerning Autler-Townes Splitting from Electromagnetically Induced Transparency". *Physical Review Letters* **107**.16, p. 163604. DOI: 10.1103/PhysRevLett.107.163604.

Appel, Jürgen, Eden Figueroa, Dmitry Korystov, M. Lobino, and A. I. Lvovsky (Mar. 5, 2008). "Quantum Memory for Squeezed Light". *Physical Review Letters* **100**.9, p. 093602. DOI: 10.1103/PhysRevLett.100.093602.

Arrazola, J. M. et al. (Mar. 2021). "Quantum circuits with many photons on a programmable nanophotonic chip". *Nature* **591**.7848, pp. 54–60. DOI: 10.1038/s41586-021-03202-1.

Arute, Frank et al. (Oct. 2019). "Quantum supremacy using a programmable superconducting processor". *Nature* **574**.7779, pp. 505–510. DOI: 10.1038/s41586-019-1666-5.

Aspect, Alain, Jean Dalibard, and Gérard Roger (Dec. 20, 1982). "Experimental Test of Bell's Inequalities Using Time-Varying Analyzers". *Physical Review Letters* **49**.25, pp. 1804–1807. DOI: 10.1103/PhysRevLett.49.1804.

Aspuru-Guzik, Alán and Philip Walther (Apr. 2012). "Photonic quantum simulators". *Nature Physics* **8**.4, pp. 285–291. DOI: 10.1038/nphys2253.

B

Bao, Xiao-Hui, Andreas Reingruber, Peter Dietrich, Jun Rui, Alexander Dück, Thorsten Strassel, Li Li, Nai-Le Liu, Bo Zhao, and Jian-Wei Pan (July 1, 2012). "Efficient and long-lived quantum memory with cold atoms inside a ring cavity". *Nature Physics* **8**.7, pp. 517–521. DOI: 10.1038/nphys2324.

Bell, J. S. (Nov. 1, 1964). "On the Einstein Podolsky Rosen paradox". *Physics Physique Fizika* **1**.3, pp. 195–200. DOI: 10.1103/PhysicsPhysiqueFizika.1.195.

Bennett, Charles H., Gilles Brassard, Claude Crépeau, Richard Jozsa, Asher Peres, and William K. Wootters (Mar. 29, 1993). "Teleporting an unknown quantum state via dual classical and Einstein-Podolsky-Rosen channels". *Physical Review Letters* **70**.13, pp. 1895–1899. DOI: 10.1103/PhysRevLett.70.1895.

Bennett, Charles H., Gilles Brassard, Sandu Popescu, Benjamin Schumacher, John A. Smolin, and William K. Wootters (Jan. 29, 1996). "Purification of Noisy Entanglement and Faithful Teleportation via Noisy Channels". *Physical Review Letters* **76**.5, pp. 722–725. DOI: 10.1103/PhysRevLett.76.722.

Bernien, H. et al. (May 2013). "Heralded entanglement between solid-state qubits separated by three metres". *Nature* **497**.7447, pp. 86–90. DOI: 10.1038/nature12016.

Berroir, Jérémy, Adrien Bouscal, Alban Urvoy, Tridib Ray, and Julien Laurat (Sept. 28, 2021). "Nanotrappy: An open-source versatile package for cold-atom trapping close to nanostructures". *arXiv:2109.13954 [physics, physics:quant-ph]*. arXiv: 2109.13954.

Blatt, R. and C. F. Roos (Apr. 2012). "Quantum simulations with trapped ions". *Nature Physics* **8**.4, pp. 277–284. DOI: 10.1038/nphys2252.

Bloch, Immanuel, Jean Dalibard, and Sylvain Nascimbène (Apr. 2012). "Quantum simulations with ultracold quantum gases". *Nature Physics* **8**.4, pp. 267–276. DOI: 10.1038/nphys2259.

Boaron, Alberto et al. (Nov. 5, 2018). "Secure Quantum Key Distribution over 421 km of Optical Fiber". *Physical Review Letters* **121**.19, p. 190502. DOI: 10.1103/PhysRevLett.121.190502.

Bouillard, M., G. Boucher, J. Ferrer Ortas, B. Pointard, and R. Tualle-Brouri (May 29, 2019). "Quantum Storage of Single-Photon and Two-Photon Fock States with an All-Optical Quantum Memory". *Physical Review Letters* **122**.21, p. 210501. DOI: 10.1103/PhysRevLett.122.210501.

Bouwmeester, Dik, Jian-Wei Pan, Klaus Mattle, Manfred Eibl, Harald Weinfurter, and Anton Zeilinger (Dec. 1997). "Experimental quantum teleportation". *Nature* **390**.6660, pp. 575–579. DOI: 10.1038/37539.

Bozzio, Mathieu, Eleni Diamanti, and Frédéric Grosshans (Feb. 27, 2019). "Semi-device-independent quantum money with coherent states". *Physical Review A* **99**.2, p. 022336. DOI: 10.1103/PhysRevA.99.022336.

Bozzio, Mathieu, Adeline Orieux, Luis Trigo Vidarte, Isabelle Zaquine, Iordanis Kerenidis, and Eleni Diamanti (Jan. 30, 2018). "Experimental investigation of practical unforgeable quantum money". *npj Quantum Information* **4**.1, pp. 1–8. DOI: 10.1038/s41534-018-0058-2.

Braunstein, Samuel L. and Peter van Loock (June 29, 2005). "Quantum information with continuous variables". *Reviews of Modern Physics* **77**.2, pp. 513–577. DOI: 10.1103/RevModPhys.77.513.

Brekenfeld, Manuel, Dominik Niemietz, Joseph Dale Christesen, and Gerhard Rempe (June 2020). "A quantum network node with crossed optical fibre cavities". *Nature Physics* **16**.6, pp. 647–651. DOI: 10.1038/s41567-020-0855-3.

Briegel, H.-J., W. Dür, J. I. Cirac, and P. Zoller (Dec. 28, 1998). "Quantum Repeaters: The Role of Imperfect Local Operations in Quantum Communication". *Physical Review Letters* **81**.26, pp. 5932–5935. DOI: 10.1103/PhysRevLett.81.5932.

Briegel, H.-J. et al. (2000). "Quantum Networks and Multi-Particle Entanglement". *The Physics of Quantum Information: Quantum Cryptography, Quantum Teleportation, Quantum Computation*. Ed. by Dirk Bouwmeester, Artur Ekert, and Anton Zeilinger. Berlin, Heidelberg: Springer, pp. 191–220. DOI: 10.1007/978-3-662-04209-0_6.

Broadbent, Anne, Joseph Fitzsimons, and Elham Kashefi (Oct. 2009). "Universal Blind Quantum Computation". *2009 50th Annual IEEE Symposium on Foundations of Computer Science*. 2009 50th Annual IEEE Symposium on Foundations of Computer Science, pp. 517–526. DOI: 10.1109/FOCS.2009.36.

Burnham, David C. and Donald L. Weinberg (July 13, 1970). "Observation of Simultaneity in Parametric Production of Optical Photon Pairs". *Physical Review Letters* **25**.2, pp. 84–87. DOI: 10.1103/PhysRevLett.25.84.

Bussières, Félix, Nicolas Sangouard, Mikael Afzelius, Hugues de Riedmatten, Christoph Simon, and Wolfgang Tittel (Oct. 1, 2013). "Prospective applications of optical quantum memories". *Journal of Modern Optics* **60**.18, pp. 1519–1537. DOI: 10.1080/09500340.2013.856482.

Bustard, Philip J., Rune Lausten, Duncan G. England, and Benjamin J. Sussman (Aug. 19, 2013). "Toward Quantum Processing in Molecules: A THz-Bandwidth Coherent Memory for Light". *Physical Review Letters* **111**.8, p. 083901. DOI: 10.1103/PhysRevLett.111.083901.

C

Cao, Mingtao, Félix Hoffet, Shuwei Qiu, Alexandra S. Sheremet, and Julien Laurat (Oct. 20, 2020). "Efficient reversible entanglement transfer between light and quantum memories". *Optica* **7**.10, pp. 1440–1444. DOI: 10.1364/OPTICA.400695.

Carlson, N. W., Y. S. Bai, W. R. Babbitt, and T. W. Mossberg (Sept. 1, 1984). "Temporally programmed free-induction decay". *Physical Review A* **30**.3, pp. 1572–1574. DOI: 10.1103/PhysRevA.30.1572.

Cartlidge, Edwin (Nov. 2, 2018). "Europe's €1 billion quantum flagship announces grants". *Science* **362**.6414, pp. 512–512. DOI: 10.1126/science.362.6414.512.

Chanelière, T., D. N. Matsukevich, S. D. Jenkins, T. A. B. Kennedy, M. S. Chapman, and A. Kuzmich (Mar. 10, 2006). "Quantum Telecommunication Based on Atomic Cascade Transitions". *Physical Review Letters* **96**.9, p. 093604. DOI: 10.1103/PhysRevLett.96.093604.

Chanelière, T., D. N. Matsukevich, S. D. Jenkins, S.-Y. Lan, T. a. B. Kennedy, and A. Kuzmich (Dec. 2005). "Storage and retrieval of single photons transmitted between remote quantum memories". *Nature* **438**.7069, pp. 833–836. DOI: 10.1038/nature04315.

Chanelière, Thierry and Gabriel Hétet (Apr. 1, 2015). "Light-shift-modulated photon-echo". *Optics Letters* **40**.7, pp. 1294–1297. DOI: 10.1364/OL.40.001294.

Chen, Yi-Hsin, Meng-Jung Lee, I-Chung Wang, Shengwang Du, Yong-Fan Chen, Ying-Cheng Chen, and Ite A. Yu (Feb. 20, 2013). "Coherent Optical Memory with High Storage Efficiency and Large Fractional Delay". *Physical Review Letters* **110**.8, p. 083601. DOI: 10.1103/PhysRevLett.110.083601.

Chen, Lirong, Zhongxiao Xu, Weiqing Zeng, Yafei Wen, Shujing Li, and Hai Wang (Sept. 26, 2016). "Controllably releasing long-lived quantum memory for photonic polarization qubit into multiple spatially-separate photonic channels". *Scientific Reports* **6**.1, p. 33959. DOI: 10.1038/srep33959.

Chen, Moran, Nicolas C. Menicucci, and Olivier Pfister (Mar. 26, 2014). "Experimental Realization of Multipartite Entanglement of 60 Modes of a Quantum Optical Frequency Comb". *Physical Review Letters* **112**.12, p. 120505. DOI: 10.1103/PhysRevLett.112.120505.

Chi-Chih Yao, A. (Nov. 1993). "Quantum circuit complexity". *Proceedings of 1993 IEEE 34th Annual Foundations of Computer Science*. Proceedings of 1993 IEEE 34th Annual Foundations of Computer Science, pp. 352–361. DOI: 10.1109/SFCS.1993.366852.

Cho, Y.-W., G. T. Campbell, J. L. Everett, J. Bernu, D. B. Higginbottom, M. T. Cao, J. Geng, N. P. Robins, P. K. Lam, and B. C. Buchler (Jan. 20, 2016). "Highly efficient optical quantum memory with long coherence time in cold atoms". *Optica* **3**.1, pp. 100–107. DOI: 10.1364/OPTICA.3.000100.

Choi, K. S., H. Deng, J. Laurat, and H. J. Kimble (Mar. 2008). "Mapping photonic entanglement into and out of a quantum memory". *Nature* **452**.7183, pp. 67–71. DOI: 10.1038/nature06670.

Chou, C. W., H. de Riedmatten, D. Felinto, S. V. Polyakov, S. J. van Enk, and H. J. Kimble (Dec. 2005). "Measurement-induced entanglement for excitation stored in remote atomic ensembles". *Nature* **438**.7069, pp. 828–832. DOI: 10.1038/nature04353.

Chou, Chin-Wen, Julien Laurat, Hui Deng, Kyung Soo Choi, Hugues de Riedmatten, Daniel Felinto, and H. Jeff Kimble (June 1, 2007). "Functional Quantum Nodes for Entanglement Distribution over Scalable Quantum Networks". *Science*.

Cirac, J. I., P. Zoller, H. J. Kimble, and H. Mabuchi (Apr. 21, 1997). "Quantum State Transfer and Entanglement Distribution among Distant Nodes in a Quantum Network". *Physical Review Letters* **78**.16, pp. 3221–3224. DOI: 10.1103/PhysRevLett.78.3221.

Clausen, Christoph, Imam Usmani, Félix Bussières, Nicolas Sangouard, Mikael Afzelius, Hugues de Riedmatten, and Nicolas Gisin (Jan. 2011). "Quantum storage of photonic entanglement in a crystal". *Nature* **469**.7331, pp. 508–511. DOI: 10.1038/nature09662.

Cooper, C. J, G Hillenbrand, J Rink, C. G Townsend, K Zetie, and C. J Foot (Nov. 20, 1994). "The Temperature of Atoms in a Magneto-optical Trap". *Europhysics Letters (EPL)* **28**.6, pp. 397–402. DOI: 10.1209/0295-5075/28/6/004.

Coopmans, Tim et al. (July 16, 2021). "NetSquid, a NETwork Simulator for QUantum Information using Discrete events". *Communications Physics* **4**.1, pp. 1–15. DOI: 10.1038/s42005-021-00647-8.

Corzo, Neil V., Baptiste Gouraud, Aveek Chandra, Akihisa Goban, Alexandra S. Sheremet, Dmitriy V. Kupriyanov, and Julien Laurat (Sept. 23, 2016). "Large Bragg Reflection from One-Dimensional Chains of Trapped Atoms Near a Nanoscale Waveguide". *Physical Review Letters* **117**.13, p. 133603. DOI: 10.1103/PhysRevLett.117.133603.

Corzo, Neil V., Jérémy Raskop, Aveek Chandra, Alexandra S. Sheremet, Baptiste Gouraud, and Julien Laurat (Feb. 2019). "Waveguide-coupled single collective excitation of atomic arrays". *Nature* **566**.7744, pp. 359–362. DOI: 10.1038/s41586-019-0902-3.

D

Dahlberg, Axel et al. (Aug. 19, 2019). "A Link Layer Protocol for Quantum Networks". *Proceedings of the ACM Special Interest Group on Data Communication*, pp. 159–173. DOI: 10.1145/3341302.3342070. arXiv: 1903.09778.

Dai, Han-Ning et al. (May 21, 2012). "Holographic Storage of Biphoton Entanglement". *Physical Review Letters* **108**.21, p. 210501. DOI: 10.1103/PhysRevLett.108.210501.

Dalibard, J. and C. Cohen-Tannoudji (Nov. 1, 1989). "Laser cooling below the Doppler limit by polarization gradients: simple theoretical models". *JOSA B* **6**.11, pp. 2023–2045. DOI: 10.1364/JOSAB.6.002023.

De Greve, Kristiaan et al. (Nov. 2012). "Quantum-dot spin–photon entanglement via frequency downconversion to telecom wavelength". *Nature* **491**.7424, pp. 421–425. DOI: 10.1038/nature11577.

Deutsch, David and Richard Jozsa (Dec. 8, 1992). "Rapid solution of problems by quantum computation". *Proceedings of the Royal Society of London. Series A: Mathematical and Physical Sciences* **439**.1907, pp. 553–558. DOI: 10.1098/rspa.1992.0167.

Ding, Dong-Sheng, Wei Zhang, Zhi-Yuan Zhou, Shuai Shi, Bao-Sen Shi, and Guang-Can Guo (May 2015). "Raman quantum memory of photonic polarized entanglement". *Nature Photonics* **9**.5, pp. 332–338. DOI: 10.1038/nphoton.2015.43.

Ding, Dong-Sheng, Wei Zhang, Zhi-Yuan Zhou, Shuai Shi, Guo-Yong Xiang, Xi-Shi Wang, Yun-Kun Jiang, Bao-Sen Shi, and Guang-Can Guo (Feb. 4, 2015). "Quantum Storage of Orbital Angular Momentum Entanglement in an Atomic Ensemble". *Physical Review Letters* **114**.5, p. 050502. DOI: 10.1103/PhysRevLett.114.050502.

Drewsen, M., Ph. Laurent, A. Nadir, G. Santarelli, A. Clairon, Y. Castin, D. Grison, and C. Salomon (Sept. 1, 1994). "Investigation of sub-Doppler cooling effects in a cesium magneto-optical trap". *Applied Physics B* **59**.3, pp. 283–298. DOI: 10.1007/BF01081396.

Duan, L. -M., J. I. Cirac, and P. Zoller (Aug. 27, 2002). "Three-dimensional theory for interaction between atomic ensembles and free-space light". *Physical Review A* **66**.2, p. 023818. DOI: 10.1103/PhysRevA.66.023818.

Duan, L.-M., M. D. Lukin, J. I. Cirac, and P. Zoller (Nov. 2001). "Long-distance quantum communication with atomic ensembles and linear optics". *Nature* **414**.6862, pp. 413–418. DOI: 10.1038/35106500.

Dudin, Y. O., L. Li, and A. Kuzmich (Mar. 6, 2013). "Light storage on the time scale of a minute". *Physical Review A* **87**.3, p. 031801. DOI: 10.1103/PhysRevA.87.031801.

Dutt, M. V. Gurudev, L. Childress, L. Jiang, E. Togan, J. Maze, F. Jelezko, A. S. Zibrov, P. R. Hemmer, and M. D. Lukin (June 1, 2007). "Quantum Register Based on Individual Electronic and Nuclear Spin Qubits in Diamond". *Science* **316**.5829, pp. 1312–1316. DOI: 10.1126/science.1139831.

E

Eisaman, M. D., J. Fan, A. Migdall, and S. V. Polyakov (July 2011). "Invited Review Article: Single-photon sources and detectors". *Review of Scientific Instruments* **82**.7, p. 071101. DOI: 10.1063/1.3610677.

Eisert, Jens, Dominik Hangleiter, Nathan Walk, Ingo Roth, Damian Markham, Rhea Parekh, Ulysse Chabaud, and Elham Kashefi (July 2020). "Quantum certification and benchmarking". *Nature Reviews Physics* **2**.7, pp. 382–390. DOI: 10.1038/s42254-020-0186-4.

England, D. G., P. J. Bustard, J. Nunn, R. Lausten, and B. J. Sussman (Dec. 9, 2013). "From Photons to Phonons and Back: A THz Optical Memory in Diamond". *Physical Review Letters* **111**.24, p. 243601. DOI: 10.1103/PhysRevLett.111.243601.

Enk, S. J. van, J. I. Cirac, and P. Zoller (Jan. 9, 1998). "Photonic Channels for Quantum Communication". *Science* **279**.5348, pp. 205–208. DOI: 10.1126/science.279.5348.205.

F

Farrera, Pau, Georg Heinze, Boris Albrecht, Melvyn Ho, Matías Chávez, Colin Teo, Nicolas Sangouard, and Hugues de Riedmatten (Dec. 2016). "Generation of single photons with

highly tunable wave shape from a cold atomic ensemble". *Nature Communications* **7**.1, p. 13556. DOI: 10.1038/ncomms13556.

Felinto, D., C. W. Chou, H. de Riedmatten, S. V. Polyakov, and H. J. Kimble (Nov. 9, 2005). "Control of decoherence in the generation of photon pairs from atomic ensembles". *Physical Review A* **72**.5, p. 053809. DOI: 10.1103/PhysRevA.72.053809.

Fleischhauer, M. and M. D. Lukin (May 29, 2000). "Dark-State Polaritons in Electromagnetically Induced Transparency". *Physical Review Letters* **84**.22, pp. 5094–5097. DOI: 10.1103/PhysRevLett.84.5094.

— (Jan. 15, 2002). "Quantum memory for photons: Dark-state polaritons". *Physical Review A* **65**.2, p. 022314. DOI: 10.1103/PhysRevA.65.022314.

Franzen, Alexander, Boris Hage, James DiGuglielmo, Jaromír Fiurášek, and Roman Schnabel (Oct. 13, 2006). "Experimental Demonstration of Continuous Variable Purification of Squeezed States". *Physical Review Letters* **97**.15, p. 150505. DOI: 10.1103/PhysRevLett.97.150505.

Furusawa, A., J. L. Sørensen, S. L. Braunstein, C. A. Fuchs, H. J. Kimble, and E. S. Polzik (Oct. 23, 1998). "Unconditional Quantum Teleportation". *Science* **282**.5389, pp. 706–709. DOI: 10.1126/science.282.5389.706.

G

Gavinsky, Dmitry (Dec. 4, 2014). "Quantum money with classical verification". *AIP Conference Proceedings* **1633**.1, pp. 135–140. DOI: 10.1063/1.4903116.

Gazzano, O., S. Michaelis de Vasconcellos, C. Arnold, A. Nowak, E. Galopin, I. Sagnes, L. Lanco, A. Lemaître, and P. Senellart (Feb. 5, 2013). "Bright solid-state sources of indistinguishable single photons". *Nature Communications* **4**.1, p. 1425. DOI: 10.1038/ncomms2434.

Giner, L. et al. (Jan. 22, 2013). "Experimental investigation of the transition between Autler-Townes splitting and electromagnetically-induced-transparency models". *Physical Review A* **87**.1, p. 013823. DOI: 10.1103/PhysRevA.87.013823.

Gisin, Nicolas and Rob Thew (Mar. 2007). "Quantum communication". *Nature Photonics* **1**.3, pp. 165–171. DOI: 10.1038/nphoton.2007.22.

Giustina, Marissa et al. (Dec. 16, 2015). "Significant-Loophole-Free Test of Bell's Theorem with Entangled Photons". *Physical Review Letters* **115**.25, p. 250401. DOI: 10.1103/PhysRevLett.115.250401.

Goban, A., C.-L. Hung, J. D. Hood, S.-P. Yu, J. A. Muniz, O. Painter, and H. J. Kimble (Aug. 5, 2015). "Superradiance for Atoms Trapped along a Photonic Crystal Waveguide". *Physical Review Letters* **115**.6, p. 063601. DOI: 10.1103/PhysRevLett.115.063601.

Goban, A. et al. (May 8, 2014). "Atom–light interactions in photonic crystals". *Nature Communications* **5**.1, p. 3808. DOI: 10.1038/ncomms4808.

Gorshkov, Alexey V., Axel André, Michael Fleischhauer, Anders S. Sørensen, and Mikhail D. Lukin (Mar. 19, 2007). "Universal Approach to Optimal Photon Storage in Atomic Media". *Physical Review Letters* **98**.12, p. 123601. DOI: 10.1103/PhysRevLett.98.123601.

Gorshkov, Alexey V., Axel André, Mikhail D. Lukin, and Anders S. Sørensen (Sept. 7, 2007). "Photon storage in Lambda-type optically dense atomic media. II. Free-space model". *Physical Review A* **76**.3, p. 033805. DOI: 10.1103/PhysRevA.76.033805.

Gorshkov, Alexey V., Tommaso Calarco, Mikhail D. Lukin, and Anders S. Sørensen (Apr. 4, 2008). "Photon storage in Lambda-type optically dense atomic media. IV. Optimal control using gradient ascent". *Physical Review A* **77**.4, p. 043806. DOI: 10.1103/PhysRevA.77.043806.

Gottesman, Daniel, Thomas Jennewein, and Sarah Croke (Aug. 16, 2012). "Longer-Baseline Telescopes Using Quantum Repeaters". *Physical Review Letters* **109**.7, p. 070503. DOI: 10.1103/PhysRevLett.109.070503.

Gouzien, Élie and Nicolas Sangouard (Sept. 28, 2021). "Factoring 2048-bit RSA Integers in 177 Days with 13 436 Qubits and a Multimode Memory". *Physical Review Letters* **127**.14, p. 140503. DOI: 10.1103/PhysRevLett.127.140503.

Grodecka-Grad, Anna, Emil Zeuthen, and Anders S. Sørensen (Sept. 27, 2012). "High-Capacity Spatial Multimode Quantum Memories Based on Atomic Ensembles". *Physical Review Letters* **109**.13, p. 133601. DOI: 10.1103/PhysRevLett.109.133601.

Grover, Lov K. (July 1, 1996). "A fast quantum mechanical algorithm for database search". *Proceedings of the twenty-eighth annual ACM symposium on Theory of Computing*. STOC '96. New York, NY, USA: Association for Computing Machinery, pp. 212–219. DOI: 10.1145/237814.237866.

Guccione, Giovanni, Tom Darras, Hanna Le Jeannic, Varun B. Verma, Sae Woo Nam, Adrien Cavaillès, and Julien Laurat (2021). "Connecting heterogeneous quantum networks by hybrid entanglement swapping". *Science Advances* **6**.22 (), eaba4508. DOI: 10.1126/sciadv.aba4508.

Guo, Jinxian, Xiaotian Feng, Peiyu Yang, Zhifei Yu, L. Q. Chen, Chun-Hua Yuan, and Weiping Zhang (Jan. 11, 2019). "High-performance Raman quantum memory with optimal control in room temperature atoms". *Nature Communications* **10**.1, p. 148. DOI: 10.1038/s41467-018-08118-5.

H

Hammerer, Klemens, Anders S. Sørensen, and Eugene S. Polzik (Apr. 5, 2010). "Quantum interface between light and atomic ensembles". *Reviews of Modern Physics* **82**.2, pp. 1041–1093. DOI: 10.1103/RevModPhys.82.1041.

Hanson, Ronald and David D. Awschalom (June 2008). "Coherent manipulation of single spins in semiconductors". *Nature* **453**.7198, pp. 1043–1049. DOI: 10.1038/nature07129.

Harris, S. E., J. E. Field, and A. Imamoğlu (Mar. 5, 1990). "Nonlinear optical processes using electromagnetically induced transparency". *Physical Review Letters* **64**.10, pp. 1107–1110. DOI: 10.1103/PhysRevLett.64.1107.

Harris, Stephen E. (July 1, 1997). "Electromagnetically Induced Transparency". *Physics Today* **50**.7, pp. 36–42. DOI: 10.1063/1.881806.

Hau, Lene Vestergaard, S. E. Harris, Zachary Dutton, and Cyrus H. Behroozi (Feb. 1999). "Light speed reduction to 17 metres per second in an ultracold atomic gas". *Nature* **397**.6720, pp. 594–598. DOI: 10.1038/17561.

Heinze, Georg, Christian Hubrich, and Thomas Halfmann (July 15, 2013). "Stopped Light and Image Storage by Electromagnetically Induced Transparency up to the Regime of One Minute". *Physical Review Letters* **111**.3, p. 033601. DOI: 10.1103/PhysRevLett.111.033601.

Heller, Lukas, Pau Farrera, Georg Heinze, and Hugues de Riedmatten (May 28, 2020). "Cold-Atom Temporally Multiplexed Quantum Memory with Cavity-Enhanced Noise Suppression". *Physical Review Letters* **124**.21, p. 210504. DOI: 10.1103/PhysRevLett.124.210504.

Hensen, B. et al. (Oct. 2015). "Loophole-free Bell inequality violation using electron spins separated by 1.3 kilometres". *Nature* **526**.7575, pp. 682–686. DOI: 10.1038/nature15759.

Heshami, Khabat, Duncan G. England, Peter C. Humphreys, Philip J. Bustard, Victor M. Acosta, Joshua Nunn, and Benjamin J. Sussman (Nov. 12, 2016). "Quantum memories: emerging applications and recent advances". *Journal of Modern Optics* **63**.20, pp. 2005–2028. DOI: 10.1080/09500340.2016.1148212.

Higginbottom, D. B., J. Geng, G. T. Campbell, M. Hosseini, M. T. Cao, B. M. Sparkes, J. Bernu, N. P. Robins, P. K. Lam, and B. C. Buchler (Sept. 21, 2015). "Dual-rail optical gradient echo memory". *Optics Express* **23**.19, pp. 24937–24944. DOI: 10.1364/OE.23.024937.

Holzäpfel, Adrian, Jean Etesse, Krzysztof T. Kaczmarek, Alexey Tiranov, Nicolas Gisin, and Mikael Afzelius (June 2020). "Optical storage for 0.53 s in a solid-state atomic frequency comb memory using dynamical decoupling". *New Journal of Physics* **22**.6, p. 063009. DOI: 10.1088/1367-2630/ab8aac.

Hong, C. K., Z. Y. Ou, and L. Mandel (Nov. 2, 1987). "Measurement of subpicosecond time intervals between two photons by interference". *Physical Review Letters* **59**.18, pp. 2044–2046. DOI: 10.1103/PhysRevLett.59.2044.

Hsiao, Ya-Fen, Hung-Shiue Chen, Pin-Ju Tsai, and Ying-Cheng Chen (Nov. 5, 2014). "Cold atomic media with ultrahigh optical depths". *Physical Review A* **90**.5, p. 055401. DOI: 10.1103/PhysRevA.90.055401.

Hsiao, Ya-Fen, Pin-Ju Tsai, Hung-Shiue Chen, Sheng-Xiang Lin, Chih-Chiao Hung, Chih-Hsi Lee, Yi-Hsin Chen, Yong-Fan Chen, Ite A. Yu, and Ying-Cheng Chen (May 4, 2018). "Highly Efficient Coherent Optical Memory Based on Electromag-

netically Induced Transparency". *Physical Review Letters* **120**.18, p. 183602. DOI: 10.1103/PhysRevLett.120.183602.

Humphreys, Peter C., Norbert Kalb, Jaco P. J. Morits, Raymond N. Schouten, Raymond F. L. Vermeulen, Daniel J. Twitchen, Matthew Markham, and Ronald Hanson (June 2018). "Deterministic delivery of remote entanglement on a quantum network". *Nature* **558**.7709, pp. 268–273. DOI: 10.1038/s41586-018-0200-5. arXiv: 1712.07567.

J

J. León-Montiel, R. de and Juan P. Torres (Mar. 5, 2012). "Measurement of the temperature of atomic ensembles via which-way information". *Physical Review A* **85**.3, p. 033801. DOI: 10.1103/PhysRevA.85.033801.

Jeannic, H. Le, A. Cavaillès, J. Raskop, K. Huang, and J. Laurat (Aug. 20, 2018). "Remote preparation of continuous-variable qubits using loss-tolerant hybrid entanglement of light". *Optica* **5**.8, pp. 1012–1015. DOI: 10.1364/OPTICA.5.001012.

Jensen, K., W. Wasilewski, H. Krauter, T. Fernholz, B. M. Nielsen, M. Owari, M. B. Plenio, A. Serafini, M. M. Wolf, and E. S. Polzik (Jan. 2011). "Quantum memory for entangled continuous-variable states". *Nature Physics* **7**.1, pp. 13–16. DOI: 10.1038/nphys1819.

Jiang, N., Y.-F. Pu, W. Chang, C. Li, S. Zhang, and L.-M. Duan (Apr. 16, 2019). "Experimental realization of 105-qubit random access quantum memory". *npj Quantum Information* **5**.1, pp. 1–6. DOI: 10.1038/s41534-019-0144-0.

Jiang, Yan, Jun Rui, Xiao-Hui Bao, and Jian-Wei Pan (June 10, 2016). "Dynamical zeroing of spin-wave momentum to suppress motional dephasing in an atomic-ensemble quantum memory". *Physical Review A* **93**.6, p. 063819. DOI: 10.1103/PhysRevA.93.063819.

Jin, Jeongwan, Erhan Saglamyurek, Marcel. lí Grimau Puigibert, Varun Verma, Francesco Marsili, Sae Woo Nam, Daniel Oblak, and Wolfgang Tittel (Sept. 28, 2015). "Telecom-Wavelength Atomic Quantum Memory in Optical Fiber for Heralded Polarization Qubits". *Physical Review Letters* **115**.14, p. 140501. DOI: 10.1103/PhysRevLett.115.140501.

Jobez, P., I. Usmani, N. Timoney, C. Laplane, N. Gisin, and M. Afzelius (Aug. 2014). "Cavity-enhanced storage in an optical spin-wave memory". *New Journal of Physics* **16**.8, p. 083005. DOI: 10.1088/1367-2630/16/8/083005.

Jobez, Pierre, Cyril Laplane, Nuala Timoney, Nicolas Gisin, Alban Ferrier, Philippe Goldner, and Mikael Afzelius (June 12, 2015). "Coherent Spin Control at the Quantum Level in an Ensemble-Based Optical Memory". *Physical Review Letters* **114**.23, p. 230502. DOI: 10.1103/PhysRevLett.114.230502.

Jobez, Pierre, Nuala Timoney, Cyril Laplane, Jean Etesse, Alban Ferrier, Philippe Goldner, Nicolas Gisin, and Mikael Afzelius (Mar. 21, 2016). "Towards highly multimode optical quantum memory for quantum repeaters". *Physical Review A* **93**.3, p. 032327. DOI: 10.1103/PhysRevA.93.032327.

Julsgaard, Brian, Jacob Sherson, J. Ignacio Cirac, Jaromír Fiurášek, and Eugene S. Polzik (Nov. 2004). "Experimental demonstration of quantum memory for light". *Nature* **432**.7016, pp. 482–486. DOI: 10.1038/nature03064.

K

Kalb, N., A. A. Reiserer, P. C. Humphreys, J. J. W. Bakermans, S. J. Kamerling, N. H. Nickerson, S. C. Benjamin, D. J. Twitchen, M. Markham, and R. Hanson (June 2, 2017). "Entanglement distillation between solid-state quantum network nodes". *Science* **356**.6341, pp. 928–932. DOI: 10.1126/science.aan0070.

Kalb, Norbert, Andreas Reiserer, Stephan Ritter, and Gerhard Rempe (June 2, 2015). "Heralded Storage of a Photonic Quantum Bit in a Single Atom". *Physical Review Letters* **114**.22, p. 220501. DOI: 10.1103/PhysRevLett.114.220501.

Kane, B. E. (May 1998). "A silicon-based nuclear spin quantum computer". *Nature* **393**.6681, pp. 133–137. DOI: 10.1038/30156.

Ketterle, Wolfgang, Kendall B. Davis, Michael A. Joffe, Alex Martin, and David E. Pritchard (Apr. 12, 1993). "High densities of cold atoms in a dark spontaneous-force optical trap". *Physical Review Letters* **70**.15, pp. 2253–2256. DOI: 10.1103/PhysRevLett.70.2253.

Kimble, H. J. (June 2008). "The quantum internet". *Nature* **453**.7198, pp. 1023–1030. DOI: 10.1038/nature07127.

Kok, Pieter, W. J. Munro, Kae Nemoto, T. C. Ralph, Jonathan P. Dowling, and G. J. Milburn (Jan. 24, 2007). "Linear optical quantum computing with photonic qubits". *Reviews of Modern Physics* **79**.1, pp. 135–174. DOI: 10.1103/RevModPhys.79.135.

Kómár, P., E. M. Kessler, M. Bishof, L. Jiang, A. S. Sørensen, J. Ye, and M. D. Lukin (Aug. 2014). "A quantum network of clocks". *Nature Physics* **10**.8, pp. 582–587. DOI: 10.1038/nphys3000.

Kuhlmann, Andreas V., Julien Houel, Arne Ludwig, Lukas Greuter, Dirk Reuter, Andreas D. Wieck, Martino Poggio, and Richard J. Warburton (Sept. 2013). "Charge noise and spin noise in a semiconductor quantum device". *Nature Physics* **9**.9, pp. 570–575. DOI: 10.1038/nphys2688.

Kumar, Prem (Dec. 15, 1990). "Quantum frequency conversion". *Optics Letters* **15**.24, pp. 1476–1478. DOI: 10.1364/OL.15.001476.

L

Lago-Rivera, Dario, Samuele Grandi, Jelena V. Rakonjac, Alessandro Seri, and Hugues de Riedmatten (June 2021). "Telecom-heralded entanglement between multimode solid-state quantum memories". *Nature* **594**.7861, pp. 37–40. DOI: 10.1038/s41586-021-03481-8.

Lan, S.-Y., A. G. Radnaev, O. A. Collins, D. N. Matsukevich, T. a. B. Kennedy, and A. Kuzmich (Aug. 3, 2009). "A Multiplexed Quantum Memory". *Optics Express* **17**.16, pp. 13639–13645. DOI: 10.1364/OE.17.013639.

Lanyon, B. P., T. J. Weinhold, N. K. Langford, M. Barbieri, D. F. V. James, A. Gilchrist, and A. G. White (Dec. 19, 2007). "Experimental Demonstration of a Compiled Version of Shor's Algorithm with Quantum Entanglement". *Physical Review Letters* **99**.25, p. 250505. DOI: 10.1103/PhysRevLett.99.250505.

Laplane, Cyril, Pierre Jobez, Jean Etesse, Nicolas Gisin, and Mikael Afzelius (May 24, 2017). "Multimode and Long-Lived Quantum Correlations Between Photons and Spins in a Crystal". *Physical Review Letters* **118**.21, p. 210501. DOI: 10.1103/PhysRevLett.118.210501.

Larsen, Mikkel V., Xueshi Guo, Casper R. Breum, Jonas S. Neergaard-Nielsen, and Ulrik L. Andersen (Oct. 18, 2019). "Deterministic generation of a two-dimensional cluster state". *Science* **366**.6463, pp. 369–372. DOI: 10.1126/science.aay4354.

Laurat, Julien, Hugues de Riedmatten, Daniel Felinto, Chin-Wen Chou, Erik W. Schomburg, and H. Jeff Kimble (July 24, 2006). "Efficient retrieval of a single excitation stored in an atomic ensemble". *Optics Express* **14**.15, pp. 6912–6918. DOI: 10.1364/OE.14.006912.

Lauritzen, Björn, Jiří Minář, Hugues de Riedmatten, Mikael Afzelius, Nicolas Sangouard, Christoph Simon, and Nicolas Gisin (Feb. 24, 2010). "Telecommunication-Wavelength Solid-State Memory at the Single Photon Level". *Physical Review Letters* **104**.8, p. 080502. DOI: 10.1103/PhysRevLett.104.080502.

Lee, K. C. et al. (Dec. 2, 2011). "Entangling Macroscopic Diamonds at Room Temperature". *Science* **334**.6060, pp. 1253–1256. DOI: 10.1126/science.1211914.

Leibfried, D., R. Blatt, C. Monroe, and D. Wineland (Mar. 10, 2003). "Quantum dynamics of single trapped ions". *Reviews of Modern Physics* **75**.1, pp. 281–324. DOI: 10.1103/RevModPhys.75.281.

Lett, Paul D., Richard N. Watts, Christoph I. Westbrook, William D. Phillips, Phillip L. Gould, and Harold J. Metcalf (July 11, 1988). "Observation of Atoms Laser Cooled below the Doppler Limit". *Physical Review Letters* **61**.2, pp. 169–172. DOI: 10.1103/PhysRevLett.61.169.

Lettner, M., M. Mücke, S. Riedl, C. Vo, C. Hahn, S. Baur, J. Bochmann, S. Ritter, S. Dürr, and G. Rempe (May 26, 2011). "Remote Entanglement between a Single Atom and a Bose-Einstein Condensate". *Physical Review Letters* **106**.21, p. 210503. DOI: 10.1103/PhysRevLett.106.210503.

Li, Hang et al. (June 20, 2021). "Heralding quantum entanglement between two room-temperature atomic ensembles". *Optica* **8**.6, pp. 925–929. DOI: 10.1364/OPTICA.424599.

Li, Zheng-Da et al. (Sept. 2019). "Experimental quantum repeater without quantum memory". *Nature Photonics* **13**.9, pp. 644–648. DOI: 10.1038/s41566-019-0468-5.

Lin, Yen-Wei, Hung-Chih Chou, Prashant P. Dwivedi, Ying-Cheng Chen, and Ite A. Yu (Mar. 17, 2008). "Using a pair of rectangular coils in the MOT for the production

of cold atom clouds with large optical density". *Optics Express* **16**.6, p. 3753. DOI: 10.1364/OE.16.003753.

Lipka, Micha{\textbackslash}l, Mateusz Mazelanik, and Micha{\textbackslash}l Parniak (May 2021). "Entanglement distribution with wavevector-multiplexed quantum memory". **23**.5, p. 053012. DOI: 10.1088/1367-2630/abf79a.

Liu, Chien, Zachary Dutton, Cyrus H. Behroozi, and Lene Vestergaard Hau (Jan. 2001). "Observation of coherent optical information storage in an atomic medium using halted light pulses". *Nature* **409**.6819, pp. 490–493. DOI: 10.1038/35054017.

Lu, Chao-Yang, Daniel E. Browne, Tao Yang, and Jian-Wei Pan (Dec. 19, 2007). "Demonstration of a Compiled Version of Shor's Quantum Factoring Algorithm Using Photonic Qubits". *Physical Review Letters* **99**.25, p. 250504. DOI: 10.1103/PhysRevLett.99.250504.

Lucero, Erik et al. (Oct. 2012). "Computing prime factors with a Josephson phase qubit quantum processor". *Nature Physics* **8**.10, pp. 719–723. DOI: 10.1038/nphys2385.

M

Ma, Lijun, Oliver Slattery, and Xiao Tang (Apr. 1, 2017). "Optical quantum memory based on electromagnetically induced transparency". *Journal of Optics* **19**.4, p. 043001. DOI: 10.1088/2040-8986/19/4/043001.

Marcikic, I., H. de Riedmatten, W. Tittel, H. Zbinden, and N. Gisin (Jan. 2003). "Long-distance teleportation of qubits at telecommunication wavelengths". *Nature* **421**.6922, pp. 509–513. DOI: 10.1038/nature01376.

Maring, Nicolas, Pau Farrera, Kutlu Kutluer, Margherita Mazzera, Georg Heinze, and Hugues de Riedmatten (Nov. 2017). "Photonic quantum state transfer between a cold atomic gas and a crystal". *Nature* **551**.7681, pp. 485–488. DOI: 10.1038/nature24468.

Maring, Nicolas, Dario Lago-Rivera, Andreas Lenhard, Georg Heinze, and Hugues de Riedmatten (May 20, 2018). "Quantum frequency conversion of memory-compatible single photons from 606 nm to the telecom C-band". *Optica* **5**.5, pp. 507–513. DOI: 10.1364/OPTICA.5.000507.

Massar, S. and S. Popescu (Feb. 20, 1995). "Optimal Extraction of Information from Finite Quantum Ensembles". *Physical Review Letters* **74**.8, pp. 1259–1263. DOI: 10.1103/PhysRevLett.74.1259.

Meyer-Scott, Evan, Christine Silberhorn, and Alan Migdall (Apr. 1, 2020). "Single-photon sources: Approaching the ideal through multiplexing". *Review of Scientific Instruments* **91**.4, p. 041101. DOI: 10.1063/5.0003320.

Michelberger, P. S. et al. (Apr. 2015). "Interfacing GHz-bandwidth heralded single photons with a warm vapour Raman memory". **17**.4, p. 043006. DOI: 10.1088/1367-2630/17/4/043006.

Migdall, Alan L., John V. Prodan, William D. Phillips, Thomas H. Bergeman, and Harold J. Metcalf (June 17, 1985). "First Observation of Magnetically Trapped Neutral Atoms". *Physical Review Letters* **54**.24, pp. 2596–2599. DOI: 10.1103/PhysRevLett.54.2596.

Mishina, O. S., M. Scherman, P. Lombardi, J. Ortalo, D. Felinto, A. S. Sheremet, A. Bramati, D. V. Kupriyanov, J. Laurat, and E. Giacobino (May 9, 2011). "Electromagnetically induced transparency in an inhomogeneously broadened $\ensuremath{\Lambda}$ transition with multiple excited levels". *Physical Review A* **83**.5, p. 053809. DOI: 10.1103/PhysRevA.83.053809.

Mizuochi, N. et al. (May 2012). "Electrically driven single-photon source at room temperature in diamond". *Nature Photonics* **6**.5, pp. 299–303. DOI: 10.1038/nphoton.2012.75.

Moehring, D. L., P. Maunz, S. Olmschenk, K. C. Younge, D. N. Matsukevich, L.-M. Duan, and C. Monroe (Sept. 2007). "Entanglement of single-atom quantum bits at a distance". *Nature* **449**.7158, pp. 68–71. DOI: 10.1038/nature06118.

Moiseev, S. A. and W. Tittel (June 2011). "Optical quantum memory with generalized time-reversible atom–light interaction". **13**.6, p. 063035. DOI: 10.1088/1367-2630/13/6/063035.

Moore, Gordon E. (Sept. 2006). "Cramming more components onto integrated circuits, Reprinted from Electronics, volume 38, number 8, April 19, 1965, pp.114 ff." *IEEE Solid-State Circuits Society Newsletter* **11**.3, pp. 33–35. DOI: 10.1109/N-SSC.2006.4785860.

Morin, Olivier, Jean-Daniel Bancal, Melvyn Ho, Pavel Sekatski, Virginia D'Auria, Nicolas Gisin, Julien Laurat, and Nicolas Sangouard (Mar. 25, 2013). "Witnessing Trustworthy Single-Photon Entanglement with Local Homodyne Measurements". *Physical Review Letters* **110**.13, p. 130401. DOI: 10.1103/PhysRevLett.110.130401.

Morin, Olivier, Virginia D'Auria, Claude Fabre, and Julien Laurat (Sept. 1, 2012). "High-fidelity single-photon source based on a Type II optical parametric oscillator". *Optics Letters* **37**.17, pp. 3738–3740. DOI: 10.1364/OL.37.003738.

Morin, Olivier, Kun Huang, Jianli Liu, Hanna Le Jeannic, Claude Fabre, and Julien Laurat (July 2014). "Remote creation of hybrid entanglement between particle-like and wave-like optical qubits". *Nature Photonics* **8**.7, pp. 570–574. DOI: 10.1038/nphoton.2014.137.

N

Nakao, Hideaki and Naoki Yamamoto (Feb. 2017). "Optimal control for perfect state transfer in linear quantum memory". **50**.6, p. 065501. DOI: 10.1088/1361-6455/aa5257.

Nguyen, T. L. et al. (Feb. 26, 2018). "Towards Quantum Simulation with Circular Rydberg Atoms". *Physical Review X* **8**.1, p. 011032. DOI: 10.1103/PhysRevX.8.011032.

Nicolas, A., L. Veissier, L. Giner, E. Giacobino, D. Maxein, and J. Laurat (Mar. 2014). "A quantum memory for orbital angular momentum photonic qubits". *Nature Photonics* **8**.3, pp. 234–238. DOI: 10.1038/nphoton.2013.355.

Northup, T. E. and R. Blatt (May 2014). "Quantum information transfer using photons". *Nature Photonics* **8**.5, pp. 356–363. DOI: 10.1038/nphoton.2014.53.

O

Osorio, C. I., N. Sangouard, and R. T. Thew (Feb. 2013). "On the purity and indistinguishability of down-converted photons". *Journal of Physics B: Atomic, Molecular and Optical Physics* **46**.5, p. 055501. DOI: 10.1088/0953-4075/46/5/055501.

P

Pan, Jian-Wei, Dik Bouwmeester, Harald Weinfurter, and Anton Zeilinger (May 4, 1998). "Experimental Entanglement Swapping: Entangling Photons That Never Interacted". *Physical Review Letters* **80**.18, pp. 3891–3894. DOI: 10.1103/PhysRevLett.80.3891.

Pan, Jian-Wei, Christoph Simon, Časlav Brukner, and Anton Zeilinger (Apr. 2001). "Entanglement purification for quantum communication". *Nature* **410**.6832, pp. 1067–1070. DOI: 10.1038/35074041.

Parigi, Valentina, Vincenzo D'Ambrosio, Christophe Arnold, Lorenzo Marrucci, Fabio Sciarrino, and Julien Laurat (July 13, 2015). "Storage and retrieval of vector beams of light in a multiple-degree-of-freedom quantum memory". *Nature Communications* **6**.1, p. 7706. DOI: 10.1038/ncomms8706.

Parkins, A. S., P. Marte, P. Zoller, and H. J. Kimble (Nov. 8, 1993). "Synthesis of arbitrary quantum states via adiabatic transfer of Zeeman coherence". *Physical Review Letters* **71**.19, pp. 3095–3098. DOI: 10.1103/PhysRevLett.71.3095.

Parniak, Michał, Michał Dąbrowski, Mateusz Mazelanik, Adam Leszczyński, Michał Lipka, and Wojciech Wasilewski (Dec. 15, 2017). "Wavevector multiplexed atomic quantum memory via spatially-resolved single-photon detection". *Nature Communications* **8**.1, p. 2140. DOI: 10.1038/s41467-017-02366-7.

Pearman, C. P., C. S. Adams, S. G. Cox, P. F. Griffin, D. A. Smith, and I. G. Hughes (Dec. 2002). "Polarization spectroscopy of a closed atomic transition: applications to laser frequency locking". *Journal of Physics B: Atomic, Molecular and Optical Physics* **35**.24, pp. 5141–5151. DOI: 10.1088/0953-4075/35/24/315.

Pompili, M. et al. (Apr. 16, 2021). "Realization of a multinode quantum network of remote solid-state qubits". *Science* **372**.6539, pp. 259–264. DOI: 10.1126/science.abg1919.

Prasad, Adarsh S., Jakob Hinney, Sahand Mahmoodian, Klemens Hammerer, Samuel Rind, Philipp Schneeweiss, Anders S. Sørensen, Jürgen Volz, and Arno Rauschenbeutel (Dec. 2020). "Correlating photons using the collective nonlinear response of atoms weakly coupled to an optical mode". *Nature Photonics* **14**.12, pp. 719–722. DOI: 10.1038/s41566-020-0692-z.

Pu, Y.-F., N. Jiang, W. Chang, H.-X. Yang, C. Li, and L.-M. Duan (May 8, 2017). "Experimental realization of a multiplexed quantum memory with 225 individually accessible memory cells". *Nature Communications* **8**.1, p. 15359. DOI: 10.1038/ncomms15359.

Pu, Yunfei, Sheng Zhang, Yukai Wu, Nan Jiang, Wei Chang, Chang Li, and Luming Duan (Feb. 25, 2021). "Experimental demonstration of memory-enhanced scaling for entanglement connection of quantum repeater segments". *Nature Photonics*. DOI: 10.1038/s41566-021-00764-4. arXiv: 2101.08541.

R

Raab, E. L., M. Prentiss, Alex Cable, Steven Chu, and D. E. Pritchard (Dec. 7, 1987). "Trapping of Neutral Sodium Atoms with Radiation Pressure". *Physical Review Letters* **59**.23, pp. 2631–2634. DOI: 10.1103/PhysRevLett.59.2631.

Radnaev, A. G., Y. O. Dudin, R. Zhao, H. H. Jen, S. D. Jenkins, A. Kuzmich, and T. a. B. Kennedy (Nov. 2010). "A quantum memory with telecom-wavelength conversion". *Nature Physics* **6**.11, pp. 894–899. DOI: 10.1038/nphys1773.

Raimond, J M, M Brune, S Haroche, and Laboratoire Kastler Brossel (2001). "Colloquium: Manipulating quantum entanglement with atoms and photons in a cavity". *Rev. Mod. Phys.* **73**.3, p. 18.

Rakonjac, Jelena V., Dario Lago-Rivera, Alessandro Seri, Margherita Mazzera, Samuele Grandi, and Hugues de Riedmatten (Nov. 19, 2021). "Entanglement between a Telecom Photon and an On-Demand Multimode Solid-State Quantum Memory". *Physical Review Letters* **127**.21, p. 210502. DOI: 10.1103/PhysRevLett.127.210502.

Rastogi, Anindya, Erhan Saglamyurek, Taras Hrushevskyi, Scott Hubele, and Lindsay J. LeBlanc (July 11, 2019). "Discerning quantum memories based on electromagnetically-induced-transparency and Autler-Townes-splitting protocols". *Physical Review A* **100**.1, p. 012314. DOI: 10.1103/PhysRevA.100.012314.

Reiserer, Andreas and Gerhard Rempe (Dec. 1, 2015). "Cavity-based quantum networks with single atoms and optical photons". *Reviews of Modern Physics* **87**.4, pp. 1379–1418. DOI: 10.1103/RevModPhys.87.1379.

Riedl, Stefan, Matthias Lettner, Christoph Vo, Simon Baur, Gerhard Rempe, and Stephan Dürr (Feb. 13, 2012). "Bose-Einstein condensate as a quantum memory for a photonic polarization qubit". *Physical Review A* **85**.2, p. 022318. DOI: 10.1103/PhysRevA.85.022318.

Ringot, J., P. Szriftgiser, and J. C. Garreau (Dec. 11, 2001). "Subrecoil Raman spectroscopy of cold cesium atoms". *Physical Review A* **65**.1, p. 013403. DOI: 10.1103/PhysRevA.65.013403.

Rowe, M. A., D. Kielpinski, V. Meyer, C. A. Sackett, W. M. Itano, C. Monroe, and D. J. Wineland (Feb. 2001). "Experimental violation of a Bell's inequality with efficient detection". *Nature* **409**.6822, pp. 791–794. DOI: 10.1038/35057215.

S

Sabooni, M., F. Beaudoin, A. Walther, N. Lin, A. Amari, M. Huang, and S. Kröll (Aug. 2, 2010). "Storage and Recall of Weak Coherent Optical Pulses with an Efficiency of 25%". *Physical Review Letters* **105**.6, p. 060501. DOI: 10.1103/PhysRevLett.105.060501.

Sabooni, Mahmood, Qian Li, Stefan Kröll, and Lars Rippe (Mar. 26, 2013). "Efficient Quantum Memory Using a Weakly Absorbing Sample". *Physical Review Letters* **110**.13, p. 133604. DOI: 10.1103/PhysRevLett.110.133604.

Saglamyurek, Erhan, Taras Hrushevskyi, Logan Cooke, Anindya Rastogi, and Lindsay J. LeBlanc (Sept. 11, 2019). "Single-photon-level light storage in cold atoms using the Autler-Townes splitting protocol". *Physical Review Research* **1**.2, p. 022004. DOI: 10.1103/PhysRevResearch.1.022004.

Saglamyurek, Erhan, Taras Hrushevskyi, Anindya Rastogi, Logan W. Cooke, Benjamin D. Smith, and Lindsay J. LeBlanc (Apr. 2021). "Storing short single-photon-level optical pulses in Bose–Einstein condensates for high-performance quantum memory". **23**.4, p. 043028. DOI: 10.1088/1367-2630/abf1d9.

Saglamyurek, Erhan, Taras Hrushevskyi, Anindya Rastogi, Khabat Heshami, and Lindsay J. LeBlanc (Dec. 2018). "Coherent storage and manipulation of broadband photons via dynamically controlled Autler–Townes splitting". *Nature Photonics* **12**.12, pp. 774–782. DOI: 10.1038/s41566-018-0279-0.

Saglamyurek, Erhan, Neil Sinclair, Jeongwan Jin, Joshua A. Slater, Daniel Oblak, Félix Bussières, Mathew George, Raimund Ricken, Wolfgang Sohler, and Wolfgang Tittel (Jan. 2011). "Broadband waveguide quantum memory for entangled photons". *Nature* **469**.7331, pp. 512–515. DOI: 10.1038/nature09719.

Salomon, C., J. Dalibard, A. Aspect, H. Metcalf, and C. Cohen-Tannoudji (Oct. 12, 1987). "Channeling atoms in a laser standing wave". *Physical Review Letters* **59**.15, pp. 1659–1662. DOI: 10.1103/PhysRevLett.59.1659.

Sangouard, Nicolas, Christoph Simon, Hugues de Riedmatten, and Nicolas Gisin (Mar. 21, 2011). "Quantum repeaters based on atomic ensembles and linear optics". *Reviews of Modern Physics* **83**.1, pp. 33–80. DOI: 10.1103/RevModPhys.83.33.

Saunders, D. J., J. H. D. Munns, T. F. M. Champion, C. Qiu, K. T. Kaczmarek, E. Poem, P. M. Ledingham, I. A. Walmsley, and J. Nunn (Mar. 3, 2016). "Cavity-Enhanced Room-Temperature Broadband Raman Memory". *Physical Review Letters* **116**.9, p. 090501. DOI: 10.1103/PhysRevLett.116.090501.

Scholl, Pascal et al. (July 2021). "Quantum simulation of 2D antiferromagnets with hundreds of Rydberg atoms". *Nature* **595**.7866, pp. 233–238. DOI: 10.1038/s41586-021-03585-1.

Schraft, Daniel, Marcel Hain, Nikolaus Lorenz, and Thomas Halfmann (Feb. 17, 2016). "Stopped Light at High Storage Efficiency in a Pr3+Y2SiO5 Crystal". *Physical Review Letters* **116**.7, p. 073602. DOI: 10.1103/PhysRevLett.116.073602.

Schweickert, Lucas et al. (Feb. 26, 2018). "On-demand generation of background-free single photons from a solid-state source". *Applied Physics Letters* **112**.9, p. 093106. DOI: 10.1063/1.5020038.

Schymik, Kai-Niklas, Vincent Lienhard, Daniel Barredo, Pascal Scholl, Hannah Williams, Antoine Browaeys, and Thierry Lahaye (Dec. 10, 2020). "Enhanced atom-by-atom assembly of arbitrary tweezer arrays". *Physical Review A* **102**.6, p. 063107. DOI: 10.1103/PhysRevA.102.063107.

Senellart, Pascale, Glenn Solomon, and Andrew White (Nov. 2017). "High-performance semiconductor quantum-dot single-photon sources". *Nature Nanotechnology* **12**.11, pp. 1026–1039. DOI: 10.1038/nnano.2017.218.

Seri, Alessandro, Dario Lago-Rivera, Andreas Lenhard, Giacomo Corrielli, Roberto Osellame, Margherita Mazzera, and Hugues de Riedmatten (Aug. 22, 2019). "Quantum Storage of Frequency-Multiplexed Heralded Single Photons". *Physical Review Letters* **123**.8, p. 080502. DOI: 10.1103/PhysRevLett.123.080502.

Shalm, Lynden K. et al. (Dec. 16, 2015). "Strong Loophole-Free Test of Local Realism". *Physical Review Letters* **115**.25, p. 250402. DOI: 10.1103/PhysRevLett.115.250402.

Shannon, C. E. (July 1948). "A mathematical theory of communication". *The Bell System Technical Journal* **27**.3, pp. 379–423. DOI: 10.1002/j.1538-7305.1948.tb01338.x.

Sheremet, A. S., L. V. Gerasimov, I. M. Sokolov, D. V. Kupriyanov, O. S. Mishina, E. Giacobino, and J. Laurat (Sept. 30, 2010). "Quantum memory for light via a stimulated off-resonant Raman process: Beyond the three-level Lambda-scheme approximation". *Physical Review A* **82**.3, p. 033838. DOI: 10.1103/PhysRevA.82.033838.

Shinbrough, Kai, Benjamin D. Hunt, and Virginia O. Lorenz (June 24, 2021). "Optimization of broadband $\mathrm{\ensuremath{\Lambda}}$-type quantum memory using Gaussian pulses". *Physical Review A* **103**.6, p. 062418. DOI: 10.1103/PhysRevA.103.062418.

Shor, P.W. (Nov. 1994). "Algorithms for quantum computation: discrete logarithms and factoring". *Proceedings 35th Annual Symposium on Foundations of Computer Science*. Proceedings 35th Annual Symposium on Foundations of Computer Science, pp. 124–134. DOI: 10.1109/SFCS.1994.365700.

Shor, Peter W (1997). "Polynomial-Time Algorithms for Prime Factorization and Discrete Logarithms on a Quantum Computer", p. 26.

Simon, Daniel R. (Oct. 1, 1997). "On the Power of Quantum Computation". *SIAM Journal on Computing* **26**.5, pp. 1474–1483. DOI: 10.1137/S0097539796298637.

Simon, Jonathan, Haruka Tanji, James K. Thompson, and Vladan Vuletić (May 3, 2007). "Interfacing Collective Atomic Excitations and Single Photons". *Physical Review Letters* **98**.18, p. 183601. DOI: 10.1103/PhysRevLett.98.183601.

Sinclair, Neil et al. (July 29, 2014). "Spectral Multiplexing for Scalable Quantum Photonics using an Atomic Frequency Comb Quantum Memory and Feed-Forward Control". *Physical Review Letters* **113**.5, p. 053603. DOI: 10.1103/PhysRevLett.113.053603.

Sprague, M. R., P. S. Michelberger, T. F. M. Champion, D. G. England, J. Nunn, X.-M. Jin, W. S. Kolthammer, A. Abdolvand, P. St J. Russell, and I. A. Walmsley (Apr. 2014). "Broadband single-photon-level memory in a hollow-core photonic crystal fibre". *Nature Photonics* **8**.4, pp. 287–291. DOI: 10.1038/nphoton.2014.45.

Steck, Daniel (Feb. 7, 1998). "Cesium D Line Data".

Stute, A., B. Casabone, B. Brandstätter, K. Friebe, T. E. Northup, and R. Blatt (Mar. 2013). "Quantum-state transfer from an ion to a photon". *Nature Photonics* **7**.3, pp. 219–222. DOI: 10.1038/nphoton.2012.358.

Stute, A., B. Casabone, P. Schindler, T. Monz, P. O. Schmidt, B. Brandstätter, T. E. Northup, and R. Blatt (May 2012). "Tunable ion–photon entanglement in an optical cavity". *Nature* **485**.7399, pp. 482–485. DOI: 10.1038/nature11120.

Surmacz, K., J. Nunn, K. Reim, K. C. Lee, V. O. Lorenz, B. Sussman, I. A. Walmsley, and D. Jaksch (Sept. 8, 2008). "Efficient spatially resolved multimode quantum memory". *Physical Review A* **78**.3, p. 033806. DOI: 10.1103/PhysRevA.78.033806.

T

Thomas, S. E., J. H. D. Munns, K. T. Kaczmarek, C. Qiu, B. Brecht, A. Feizpour, P. M. Ledingham, I. A. Walmsley, J. Nunn, and D. J. Saunders (June 2017). "High efficiency Raman memory by suppressing radiation trapping". **19**.6, p. 063034. DOI: 10.1088/1367-2630/aa7534.

Tian, Long, Zhongxiao Xu, Lirong Chen, Wei Ge, Haoxiang Yuan, Yafei Wen, Shengzhi Wang, Shujing Li, and Hai Wang (Sept. 29, 2017). "Spatial Multiplexing of Atom-Photon Entanglement Sources using Feedforward Control and Switching Networks". *Physical Review Letters* **119**.13, p. 130505. DOI: 10.1103/PhysRevLett.119.130505.

Tiranov, Alexey et al. (Dec. 9, 2016). "Temporal Multimode Storage of Entangled Photon Pairs". *Physical Review Letters* **117**.24, p. 240506. DOI: 10.1103/PhysRevLett.117.240506.

Tittel, W., M. Afzelius, T. Chaneliére, R.l. Cone, S. Kröll, S.a. Moiseev, and M. Sellars (2010). "Photon-echo quantum memory in solid state systems". *Laser & Photonics Reviews* **4**.2, pp. 244–267. DOI: 10.1002/lpor.200810056.

Townsend, C. G., N. H. Edwards, K. P. Zetie, C. J. Cooper, J. Rink, and C. J. Foot (Mar. 1, 1996). "High-density trapping of cesium atoms in a dark magneto-optical trap". *Physical Review A* **53**.3, pp. 1702–1714. DOI: 10.1103/PhysRevA.53.1702.

Tsai, Pin-Ju, Ya-Fen Hsiao, and Ying-Cheng Chen (July 28, 2020). "Quantum storage and manipulation of heralded single photons in atomic memories based on electromagnetically induced transparency". *Physical Review Research* **2**.3, p. 033155. DOI: 10.1103/PhysRevResearch.2.033155.

Tseng, Yu-Chih, Yan-Cheng Wei, and Ying-Cheng Chen (Nov. 30, 2020). "Efficient quantum memory for heralded single photons generated by cavity-enhanced spontaneous parametric downconversion". *arXiv:2011.14948 [physics, physics:quant-ph]*. arXiv: 2011.14948.

U

Ungar, P. J., D. S. Weiss, E. Riis, and Steven Chu (Nov. 1, 1989). "Optical molasses and multilevel atoms: theory". *Journal of the Optical Society of America B* **6**.11, p. 2058. DOI: 10.1364/JOSAB.6.002058.

Usmani, Imam, Christoph Clausen, Félix Bussières, Nicolas Sangouard, Mikael Afzelius, and Nicolas Gisin (Apr. 2012). "Heralded quantum entanglement between two crystals". *Nature Photonics* **6**.4, pp. 234–237. DOI: 10.1038/nphoton.2012.34.

V

Van Meter, Rodney and Simon J. Devitt (Sept. 2016). "The Path to Scalable Distributed Quantum Computing". *Computer* **49**.9, pp. 31–42. DOI: 10.1109/MC.2016.291.

Vandersypen, Lieven M. K., Matthias Steffen, Gregory Breyta, Costantino S. Yannoni, Mark H. Sherwood, and Isaac L. Chuang (Dec. 2001). "Experimental realization of Shor's quantum factoring algorithm using nuclear magnetic resonance". *Nature* **414**.6866, pp. 883–887. DOI: 10.1038/414883a.

Vernaz Gris, Pierre, Kun Huang, Mingtao Cao, Alexandra S. Sheremet, and Julien Laurat (Dec. 2018). "Highly-efficient quantum memory for polarization qubits in a spatially-multiplexed cold atomic ensemble". *Nature Communications* **9**.1, p. 363. DOI: 10.1038/s41467-017-02775-8.

Vernaz Gris, Pierre, Aaron D. Tranter, Jesse L. Everett, Anthony C. Leung, Karun V. Paul, Geoff T. Campbell, Ping Koy Lam, and Ben C. Buchler (May 14, 2018). "High-performance Raman memory with spatio-temporal reversal". *Optics Express* **26**.10, pp. 12424–12431. DOI: 10.1364/OE.26.012424.

Viola, Lorenza and Seth Lloyd (Oct. 1, 1998). "Dynamical suppression of decoherence in two-state quantum systems". *Physical Review A* **58**.4, pp. 2733–2744. DOI: 10.1103/PhysRevA.58.2733.

Vivoli, Valentina Caprara, Nicolas Sangouard, Mikael Afzelius, and Nicolas Gisin (Sept. 2013). "High-bandwidth quantum memory protocol for storing single photons in rare-earth doped crystals". *New Journal of Physics* **15**.9, p. 095012. DOI: 10.1088/1367-2630/15/9/095012.

W

Wang, Xu-Jie, Sheng-Jun Yang, Peng-Fei Sun, Bo Jing, Jun Li, Ming-Ti Zhou, Xiao-Hui Bao, and Jian-Wei Pan (Mar. 2, 2021). "Cavity-Enhanced Atom-Photon Entanglement with Subsecond Lifetime". *Physical Review Letters* **126**.9, p. 090501. DOI: 10.1103/PhysRevLett.126.090501.

Wang, Yunfei, Jianfeng Li, Shanchao Zhang, Keyu Su, Yiru Zhou, Kaiyu Liao, Shengwang Du, Hui Yan, and Shi-Liang Zhu (May 2019). "Efficient quantum memory for single-photon polarization qubits". *Nature Photonics* **13**.5, pp. 346–351. DOI: 10.1038/s41566-019-0368-8.

Wehner, Stephanie, David Elkouss, and Ronald Hanson (Oct. 19, 2018). "Quantum internet: A vision for the road ahead". *Science* **362**.6412, eaam9288. DOI: 10.1126/science.aam9288.

Wei, Yan-Cheng, Bo-Han Wu, Ya-Fen Hsiao, Pin-Ju Tsai, and Ying-Cheng Chen (Dec. 24, 2020). "Broadband coherent optical memory based on electromagnetically induced transparency". *Physical Review A* **102**.6, p. 063720. DOI: 10.1103/PhysRevA.102.063720.

Wen, Yafei, Pai Zhou, Zhongxiao Xu, Liang Yuan, Haoyi Zhang, Shengzhi Wang, Long Tian, Shujing Li, and Hai Wang (July 25, 2019). "Multiplexed spin-wave–photon entanglement source using temporal multimode memories and feedforward-controlled readout". *Physical Review A* **100**.1, p. 012342. DOI: 10.1103/PhysRevA.100.012342.

Wootters, W. K. and W. H. Zurek (Oct. 1982). "A single quantum cannot be cloned". *Nature* **299**.5886, pp. 802–803. DOI: 10.1038/299802a0.

X

Xu, Zhongxiao, Yuelong Wu, Long Tian, Lirong Chen, Zhiying Zhang, Zhihui Yan, Shujing Li, Hai Wang, Changde Xie, and Kunchi Peng (Dec. 10, 2013). "Long Lifetime and High-Fidelity Quantum Memory of Photonic Polarization Qubit by Lifting Zeeman Degeneracy". *Physical Review Letters* **111**.24, p. 240503. DOI: 10.1103/PhysRevLett.111.240503.

Y

Yang, Sheng-Jun, Xu-Jie Wang, Xiao-Hui Bao, and Jian-Wei Pan (June 2016). "An efficient quantum light–matter interface with sub-second lifetime". *Nature Photonics* **10**.6, pp. 381–384. DOI: 10.1038/nphoton.2016.51.

Yang, Tian-Shu et al. (Aug. 24, 2018). "Multiplexed storage and real-time manipulation based on a multiple degree-of-freedom quantum memory". *Nature Communications* **9**.1, p. 3407. DOI: 10.1038/s41467-018-05669-5.

Yin, Juan et al. (June 2020). "Entanglement-based secure quantum cryptography over 1,120 kilometres". *Nature* **582**.7813, pp. 501–505. DOI: 10.1038/s41586-020-2401-y.

Yu, Yong et al. (Feb. 13, 2020). "Entanglement of two quantum memories via fibers over dozens of kilometres". *Nature* **578**.7794, pp. 240–245. DOI: 10.1038/s41586-020-1976-7. arXiv: 1903.11284.

Z

Zhang, Shanchao, J. F. Chen, Chang Liu, Shuyu Zhou, M. M. T. Loy, G. K. L. Wong, and Shengwang Du (July 1, 2012). "A dark-line two-dimensional magneto-optical trap of 85Rb atoms with high optical depth". *Review of Scientific Instruments* **83**.7, p. 073102. DOI: 10.1063/1.4732818.

Zhou, Zong-Quan, Yi-Lin Hua, Xiao Liu, Geng Chen, Jin-Shi Xu, Yong-Jian Han, Chuan-Feng Li, and Guang-Can Guo (Aug. 13, 2015). "Quantum Storage of Three-Dimensional Orbital-Angular-Momentum Entanglement in a Crystal". *Physical Review Letters* **115**.7, p. 070502. DOI: 10.1103/PhysRevLett.115.070502.

Félix HOFFET **28 3 2022**

Sujet : Transfert efficace d'intrication entre photons et mémoires quantiques

Résumé : Cette thèse porte sur le développement de mémoires quantiques efficaces basées sur des ensembles d'atomes froids. Ces mémoires, qui ont la capacité de stocker un état quantique photonique pour le récupérer sur demande après un temps défini, constituent un élément central pour la construction de réseaux quantiques à grande échelle. Nous commençons par expliquer pourquoi une mémoire quantique est importante dans ce contexte, et nous expliquons de quelle façon l'efficacité d'une mémoire est un paramètre crucial, qui se doit d'être proche de l'unité pour mener à bien des applications réalistes. Nous nous concentrons ensuite sur l'optimisation de ce paramètre en expliquant notamment comment l'absorptivité des atomes et la transition choisie influe sur l'efficacité. Dans le but de préparer notre ensemble d'atomes à agir comme une mémoire quantique efficace, plusieurs techniques expérimentales sont aussi présentées. Nous démontrons finalement deux expériences de stockage quantique sur la ligne D_1 du césium. La première est le stockage de photons uniques avec une efficacité record de $\eta = (87 \pm 5)\%$. Ensuite, nous étendons ce résultat à un stockage d'intrication photonique et nous démontrons un transfert d'intrication avec une efficacité de transfert de $\lambda = (80 \pm 20)\%$. Ces résultats constituent une avancée essentielle vers la construction d'un réseau quantique de grande échelle.

Mots clés : Atomes froids, EIT, Excitation collective, Photons uniques, DLCZ, Intrication, Mémoire quantique

Subject : Highly-efficient entanglement transfer into and out of cold-atom quantum memories

Abstract: This PhD thesis focuses on the development of highly-efficient quantum memories based on large ensemble of cold cesium atoms with the ability to store photonic quantum states and retrieve it on demand, a key ingredient for large scale quantum networks. We first illustrate how memory parameters influence the performance of such a network. Specifically, we identify that a highly efficient memory is a stringent requirement. We then focus on how to optimize the efficiency of such memories by explaining the physics at play. We describe several experimental techniques to increase the absorption in our atomic ensemble, limit the temperature to a low value and optimize the magnetic environment. In this setup, by using the cesium D_1-line, we first demonstrate the storage of single photons with an efficiency of $\eta = (87 \pm 5)\%$. This is the maximal achievable value at this optical depth, and also the highest efficiency ever achieved for single-photon storage in a quantum memory regardless of the platform considered. Finally, we demonstrate an efficient mapping of single-photon entanglement into and out of two quantum memories, with an overall entanglement transfer of $\lambda = (80 \pm 20)\%$ without background correction, a three-fold increase as compared to prior work. This work constitute an essential requirement to build large-scale networks.

Keywords : Cold atoms, EIT, Collective spin excitations, Single photons, DLCZ, Entanglement, Quantum memory